Improving Voltage Stability Margin Estimation through the use of HEM and PMU Data

Final Project Report

S-77G

Power Systems Engineering Research Center
Empowering Minds to Engineer
the Future Electric Energy System

Improving Voltage Stability Margin Estimation through the use of HEM and PMU Data

Final Project Report

Project Team
Daniel Tylavsky, Project Leader
Arizona State University

Graduate Students
Qirui Li
Songyan Li
Shruti Rao
Arizona State University

PSERC Publication 19-01

August 2019

For information about this project, contact:

Daniel Tylavsky
Arizona State University
School of Electrical Computer and Energy Engineering
Engineering Research Center
P.O. Box 875706
Tempe AZ 85287
Phone: 480-965-3460
Email: tylavsky@asu.edu

Power Systems Engineering Research Center

The Power Systems Engineering Research Center (PSERC) is a multi-university Center conducting research on challenges facing the electric power industry and educating the next generation of power engineers. More information about PSERC can be found at the Center's website: http://www.pserc.org.

For additional information, contact:

Power Systems Engineering Research Center
Arizona State University
527 Engineering Research Center
Tempe, Arizona 85287-5706
Phone: 480-965-1643
Fax: 480-727-2052

Notice Concerning Copyright Material

Acknowledgements

We wish to thank all of our GEIRI North America advisors: Dr. Di Shi, Xiaohu Zhang, Xi Chen, Zhe Yu, Wendong Zhu, Xinan Wang, Janet Zhang. Special thanks to Zhiwei Wang who approved the proposal and invited the principal investigator to give multiple presentations on the progress. Also, we are indebted to Dr. Di Shi, who not only suggested the project, but saw to the funding arrangements and held numerous progress meetings with us to weigh in on the value of the various strategies taken in the research and suggest approaches when difficulties arose. This project would have never gotten off the ground without Dr. Shi and the wonderful team at GEIRI North America.

Executive Summary

Recently, a novel non-iterative power flow (PF) method known as the Holomorphic Embedding Method (HEM) was applied to the power-flow problem. The method has been shown to produce reduced-order network models (from analytical model data) that accurately captured the nonlinear behavior of the network models and were able to predict the nearness of the operating point to the saddle-nose bifurcation point (SNBP), a measure of voltage stability margin. The goal of this work was to explore whether HEM could be used with PMU measurements to similarly calculate this metric.

The work progressed in five stages. The first stage was to produce reduced-order nonlinear Thévenin-like network models using HEM and analytical model data. These reduced-order models served as accurate reference cases for the models built using PMU measurement. This first stage was completed successfully, showing the wide range of conditions over which such models were both valid and could be developed.

The second stage involved showing that the traditional maximum power transfer theorem (MPTT) used for linear models was not applicable to nonlinear models and a new nonlinear MPTT successfully derived.

The third state involed identifying ways in which the nonlinear reduced order Thévenin-like models could be used to predict the SNBP. Of the methods identified, two methods were singled out for further testing: (1) The MPTT method (using the nonlinear MPTT); (2) The Roots method (using the roots of Padé approximant of the voltage function for the bus at which the PMU measurements were taken).

In the forth stage of work, numerical methods for approximating the needed functions from measured data were proposed. Recognizing that appxoimations of the functions from measured data were senstive to precision, multiple numerical methods for both the MPTT and Roots methods were tested using psuedo-measurment from the network models identified in the first stage of this work. Advantages and limitations of both methods were identified and both methods were shown to be viable provided sufficient accuracy in the measurments and calculations was assumed.

In the fifth stage, noise was added to the pseudo-measurements and the various numerical methods proposed were reevaluated. With this test, the performance was less accurate than hoped and future work was identified to improve the performance.

Project Publications:

[1] S. Rao, D. J. Tylavsky, “Two-Bus Holomorphic Embedding Method-Based Equivalents and Weak-Bus Determination,” *arxiv.org/ftp/arxiv/papers/1706/1706.01298.pdf*, Aug. 2017, pp. 1-4.

[2] S. Rao, D. J. Tylavsky, V. Vittal, W. Yi, D. Shi, Z. Wang, “Fast Weak-Bus and Bifurcation Point Determination using Holomorphic Embedding Method,” *IEEE PES General Meeting*, July. 2018, pp. 1-5.

[3] S. Rao, S. Li, D. J. Tylavsky and Di Shi, “The Holomorphic Embedding Method Applied to a Newton Raphson Power Flow Formulation,” *2018 North American Power Symposium*, pp. 1-6, Sep. 2018.

[4] S. Li, Q. Li, D. J. Tylavsky and Di Shi, “Robust Padé Approximation Applied to the Holomorphic Embedded Power Flow Algorithm,” *2018 North American Power Symposium*, pp. 1-6, Sep. 2018.

[5] S. Li, D. J. Tylavsky, “Analytic Continuation as the Origin of Complex Distances in Impedance Approximations,” International Journal of Electrical Power and Energy Systems, Volume 105, Feb. 2019, pp. 699-708.

[6] S. Rao, D. J. Tylavsky, D. Shi, Z. Wang, “A measurement-based approach to estimate the saddle-node bifurcation point using Padé approximants,” *IEEE Trans on Power Systems*, (in preparation).

[7] S. Li, D. J. Tylavsky, D. Shi, Z. Wang, “Stahl’s Theorem Part 1: Implications to Theoretical Convergence,” *IEEE Trans on Power Systems*, (in preparation).

[8] A. Dronamraju, S. Li, Q. Li, Y. Li, D. J. Tylavsky, D. Shi, Z. Wang, “Stahl’s Theorem Part 2: Implications to Numerical Convergence,” *IEEE Trans on Power Systems*, (in preparation).

[9] S. Li, D. J. Tylavsky, D. Shi, Z. Wang, “The Padé Matrix Pencil Method,” *Society of Industrial and Applied Mathematics*, (In Preparation), 2019.

[10] S. Li, Q. Li, D. J. Tylavsky, D. Shi, Z. Wang, “Estimation of the Saddle Node Bifurcation Point using HEM and PMU Data,” *IEEE Trans on Power Systems*, (in preparation).

Student Theses:

[1] Shruti Rao, “Exploration of a Scalable Holomorphic Embedding Method Formulation for Power System Analysis Applications,” PhD Dissertation, Completed Summer, 2017.

[2] Qirui Li, “Numerical Performance of the Holomorphic Embedding Method,” MS Thesis, Completed Summer, 2018.

[3] Songyan Li, “Application of HEM to SNBP Prediction and the OPF Problem,” PhD Dissertation, in progress.

Table of Contents

List of Figures

List of Tables

1. Introduction

1.1 Overview

The holomorphic embedding power flow method (HEM) was first proposed in [1]. As a new power flow method, it has many merits including:

1) When the power flow problem has a high voltage solution, the claim [1] is that the method is guaranteed to find it.
2) When the power flow solution does not exist, the method unequivocally indicates such by its behavior.

As presented in [1], HEM uses Padé approximants to represent the bus voltage as rational functions of a load scaling factor. The poles and zeros of the rational function are closely related to the voltage collapse point. This suggests that, if the rational function approximation can be built for the bus voltages from local measurement, the location of the voltage collapse point (the saddle node bifurcation point, SNBP) may be extracted from the rational function approximation. This idea is studied, and the theory and results are presented in this report.

Chapter 2 includes a literature review of different methods of evaluating the saddle -node bifurcation point of a power system.

Chapter 3 contains a discussion on the traditional way of using local measurements to build Thévenin equivalent networks at the bus-of-interest and explores its different aspects. Nonlinear Thévenin-like networks are then built using model data and it is shown that the series impedance in the Thévenin-like network can be assumed to be of any reasonable desired value and the nonlinear voltage source model parameters calculated using the procedures introduced here are such as to preserve the load voltage and load current behavior. Multi-bus nonlinear networks are developed in which network topology and parameters can be made arbitrary and the nonlinear current injections can be suitably modified such that the load voltage and load current behavior is preserved. The arbitrariness of the nonlinear reduced-order networks can be used to simplify the process of obtaining such networks using local measurements.

Chapter 4 concentrates on the SNBP estimation from HE-based Thévenin-like networks using local-measurements. The Maximum Power Transfer Theorem (MPTT) is validated with extremely high precision. The comparison of four different numerical methods based on the MPTT are tested on the modified IEEE 118-bus system using pseudo-measurements. The roots method is also discussed and compared with the MPTT method. The effect of noisy measurements on the accuracy of SNBP estimation is explored.

Finally, the conclusion and the scope for the future work are included in Chapter 5.

2. Literature Review

In recent years, power systems are operated under increasingly stressed conditions, which has elevated the concern about system voltage stability. The saddle-node bifurcation point (SNBP) can be used as a useful voltage-stability-margin metric and hence the prediction of SNBP has received significant attention [3].

When the loads of a power system increase up to a critical limit, the static model of the power system will experience voltage collapse and this critical point is identified as a saddle-node bifurcation point (SNBP). In mathematics, the SNBP represents the intersection points where different equilibria of a dynamical system meet [4]. When the dynamic model is constructed using classical machine models, the equilibria are represented by a set of nonlinear algebraic equations and the SNBP is a saddle-nose type of branch point in this set of algebraic equations. In this section, several methods of estimating the SNBP will be discussed.

2.1 Continuation Power Flow

The continuation power flow (CPF) [5] is a NR-based method which can be used to trace the P-V curve from a base case up to the maximum loading point by solving successive power flows while scaling up the load and generation level of the power system [5]. In the CPF method, the power flow (PF) equations are reformulated to include a loading parameter to eliminate the singularity of Jacobian matrix when close to SNBP. The basic strategy behind the CPF is to use of a predictor-corrector scheme, which contains two steps: One is to predict the next solution by taking a specified step size in the direction of a tangent vector corresponding to a different value of the load parameter. Then the other one is to correct the solution using a local parameterization technique.

The computational complexity of the CPF is much higher than the Newton-Raphson method since it requires calculating many operating points on the P-V curve. In addition, the control of the step size and the continuation parameter play a key role in computational efficiency of CPF. For example, a small step size gives too many solution points and requires much computation time, whereas a large step size may give a poor starting point in predictor and thus cause divergence in corrector.

Various modified versions of CPF methods have been proposed to improve the accuracy and speed of the CPF. In [6]-[8], the geometric parameterization technique is used. In [9]-[11], modified predictor-corrector approaches are introduced. Techniques for controlling the step size are also proposed in [9]-[11]. In [12], multiple power injection variations in the power system are modeled.

References [6]-[8] present an efficient geometric parameterization technique for the CPF from the observation of the geometrical behavior of PF solutions. The Jacobian matrix singularity is avoided by the addition of a line equation, which passes through a point in the plane determined by the total real power losses and loading factor.

In [9], a singularity avoidance procedure is implemented around the SNBP. This method avoids the computational complexities of the existing CPFs and overcomes the difficulty of how to smoothly cross through the SNBP and continue tracing the lower part of the P-V curve. In [10], the CPF with an adaptive step size control using a convergence monitor is proposed. It is shown that this approach needs much less time and does not need the critical buses preselected. A modified fast-decoupled power flow based CPF is reported in [11]. The use of a first-order polynomial secant predictor, where the step size controlled using the Euclidean norm of the tangent vector, reduces the number of iterations of the corrector step.

In [12], an improved CPF is proposed that allows the power injections at each bus to vary according to multiple load variations and actual real generation dispatch.

2.2 HEM-based methods

Since holomorphic embedding method (HEM) can eliminate the non-convergence issues of those traditional iterative methods, this advantage can be exploited to develop methods that can reliably estimate the SNBP of a system. In [2] , four different HEM-based methods to estimate the SNBP are proposed and compared in terms of accuracy as well as computational efficiency:

2.2.1 Power-Flow Search Method (PFSM)

In this approach, the PF equations are embedded in a non-extrapolating way such that the formulation is only valid at α =1 and has no meaningful interpretation at any other value of α. A binary search, which is similar to CPF, is performed until the SNBP is reached. This involves solving multiple PF problems and is of the order of the complexity of the CPF. This approach is computationally the most expensive method of the four proposed HEM-based methods [2].

2.2.2 Padé Approximant Search (PAS)

By using an extrapolation embedding formulation, the solution obtained at different values of α can represent the solution when the loads and real power generation of the system are uniformly scaled by a factor of α. Therefore, the PF problem only needs to be solved once to get the Padé approximants (PA's) and then, by using a binary search approach and evaluating the Padé approximants for various α values, the SNBP is obtained [2].

2.2.3 Extrapolating Sigma Method (ESM)

The idea behind this method is to develop a two-bus equivalent network consisting of only slack bus and one retained bus and use the so-called σ index to estimate the SNBP of the system. The condition to ensure the system is short of or at its static voltage collapse point, called the 'σ condition', is given by:

$$\frac{1}{4} + \sigma_R - \sigma_I^2 \geq 0 \tag{2.1}$$

With the proposed extrapolation formulation, σ is obtained as a function of α. Then the SNBP of the system can be estimated by evaluating the Padé approximates for all the $\sigma_i(\alpha)$ at escalating values of α until the σ condition is violated [2].

2.2.4 Roots method

In this approach, the extrapolation formulation is used to estimate the SNBP using the poles and zeros of the Padé approximates of an arbitrary bus. The smallest real zero/pole is taken as the load-scaling factor at the SNBP. Unlike the method proposed in sections 2.2.1, 2.2.2 and 2.2.3, the roots method does not involve any binary search process, which could be computationally expensive. This method is shown to be the most efficient of all the HEM methods, provided a reference state for the scalable-form power flow exists [2].

2.3 Measurement-based methods

The main idea of the local-measurement-based approach [13]-[18] comes from the impedance matching concept of the single-port Thévenin equivalent circuit: The local voltage and local current measurements are used to build a Thévenin equivalent representing the system as viewed from the bus of interest. When the system is at the voltage collapse point, the Thévenin impedance has the same magnitude as load impedance. The parameters of the Thévenin equivalent are estimated using the least-squares method [13], [14], or Kalman filter method [18], or other alternative methods [15], [16]. A comparative study of four Thévenin equivalent identification methods was examined in [17]. Once the Thévenin equivalent parameters are obtained, a voltage stability index is computed to track the voltage stability margin. Some other indices such as power margin have been used in [14], [18] to provide information of how much load should be shed.

The wide deployment of phasor measurement units (PMU) has opened new perspectives for developing wide-area measurement-based methods to estimate voltage stability margin [19]-[26]. Effort has been focused on building a more accurate models from measurements on all monitored buses [21], [22]-[24]. Reference [22] provides a modified coupled single-port model for long-term voltage-stability assessment (VSA). In [23], a quasi-steady-state model for the external injections is constructed. A multiport Thévenin equivalent network has been built in [24] to better account for the different limits on individual tie-lines connecting to the load area. A comparison of different methods using local measurements or wide-area measurements to estimate the voltage stability margin was completed in [26].

3. Local-Measurement-Based Methods of Steady-State Voltage Stability Analysis

3.1 Local-measurement-based methods of estimating the steady-state voltage stability margin

Local-measurement-based methods of estimating the steady-state voltage stability margin [13] - [17], [19], [26], [36], [37], [38] and [39] use the load voltage and load current measurements at the bus-of-interest to build a Thévenin equivalent network (assuming that the parameters of the Thévenin equivalent remain constant during the sampling period) as shown in Figure 3.1. Impedance matching is then used to estimate the steady-state voltage stability margin [13] - [17], [19], [26], [36], [37], [38] and [39].

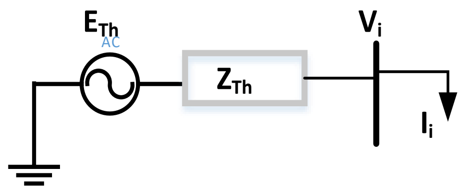

Figure 3.1 Thévenin equivalent at the bus of interest

A minimum of two distinct phasor measurements each, of the load voltage and the load current are needed to estimate the Thévenin network parameters. The equations used to estimate the Thévenin equivalent parameters are given by (3.1),

$$E_{Th} - I_i Z_{Th} = V_i \tag{3.1}$$

where E_{Th} is the Thévenin voltage, Z_{Th} is the Thévenin impedance, V_i is the load voltage and I_i is the load current. If perfect measurements are used, two distinct phasor measurements are sufficient and the expression for the Thévenin equivalent parameters are given by (3.2) and (3.3) [36], [15].

$$Z_{Th} = (V_1 - V_2)/(I_2 - I_1) \tag{3.2}$$

$$E_{Th} = (V_1 I_2 - V_2 I_1)/(I_2 - I_1) \tag{3.3}$$

However, in the absence of perfect measurements, and with the changes in Thévenin parameters due to changing system conditions, a larger number of measurements are required to obtain a reasonable estimate of the Thévenin equivalent parameters, i.e. $E_{Th} = E_{Re}+jE_{Im}$ and $Z_{Th} = R_{Th}+jX_{Th}$ [13]. If one has K (K>2) number of phasor measurements of the voltage at bus i ($V_i = V_{Re}+jV_{Im}$) and the load current at bus i, ($Ii = I_{Re}+jI_{Im}$), the estimation of E_{Th} and Z_{Th} may be performed by solving the overdetermined set of equations given by (3.4), which is a least-squares minimization of the error.

$$\begin{bmatrix} 1 & 0 & -I_{1\_\mathrm{Re}} & I_{1\_\mathrm{Im}} \\ 0 & 1 & -I_{1\_\mathrm{Im}} & -I_{1\_\mathrm{Re}} \\ \vdots & \vdots & \vdots & \vdots \\ 1 & 0 & -I_{K\_\mathrm{Re}} & I_{K\_\mathrm{Im}} \\ 0 & 1 & -I_{K\_\mathrm{Im}} & -I_{K\_\mathrm{Re}} \end{bmatrix} \times \begin{bmatrix} E_{\mathrm{Re}} \\ E_{\mathrm{Im}} \\ R_{Th} \\ X_{Th} \end{bmatrix} = \begin{bmatrix} V_{1\_\mathrm{Re}} \\ V_{1\_\mathrm{Im}} \\ \vdots \\ V_{K\_\mathrm{Re}} \\ V_{K\_\mathrm{Im}} \end{bmatrix} \tag{3.4}$$

It is well known that, if the voltage source is constant and the load power factor is allowed to vary, maximum real power is delivered to the load when $Z_L = Z_{Th}^*$. For a load with a fixed power factor, the maximum power is transferred to the load when $|Z_{Th}|=|Z_L|$ (where |.| refers to the magnitude operator), which can be derived as follows: (This well known proof is included as a variation of it will be used to prove a similar result when HEM is used.)

Consider the load to be represented by an equivalent impedance Z_L as shown in Figure 3.2.

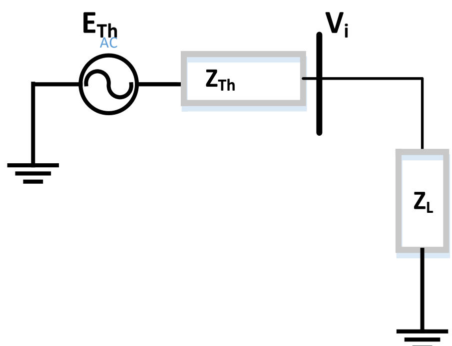

Figure 3.2 Thévenin impedance and load impedance

The real power delivered to the load is given by:

$$P_L = |I_L|^2 R_L \tag{3.5}$$

The load current in the Thévenin equivalent network is given by:

$$I_L = \frac{E_{Th}}{(Z_{Th} + Z_L)} \tag{3.6}$$

Using (3.5) and (3.6), we get:

$$P_L = \left|\frac{E_{Th}}{(Z_{Th} + Z_L)}\right|^2 R_L = \frac{|E_{Th}|^2}{(R_{Th} + R_L)^2 + (X_{Th} + X_L)^2} R_L \tag{3.7}$$

Assuming the power factor angle of the load, φ, is kept fixed, the load impedance can be written as:

$$Z_L = R_L + jX_L = R_L + jR_L \tan(\phi) \tag{3.8}$$

Equation (3.7) can thus be written as:

$$P_L = \frac{|E_{Th}|^2 R_L}{(R_{Th} + R_L)^2 + (X_{Th} + R_L \tan\phi)^2} \tag{3.9}$$

The derivative of P_L with respect to R_L is given by (keeping in mind that E_{Th} and Z_{Th} are assumed to be constant):

$$\begin{aligned} &\frac{dP_L}{dR_L} = \\ &|E_{Th}|^2 \frac{\left((R_{Th} + R_L)^2 + (X_{Th} + R_L \tan\phi)^2\right)}{\left((R_{Th} + R_L)^2 + (X_{Th} + R_L \tan\phi)^2\right)^2} \\ &-|E_{Th}|^2 \frac{R_L\left(2(R_{Th} + R_L) + 2(X_{Th} + R_L \tan\phi)\tan\phi\right)}{\left((R_{Th} + R_L)^2 + (X_{Th} + R_L \tan\phi)^2\right)^2} \end{aligned} \tag{3.10}$$

When the power delivered to the load is maximum, the derivative of P_L with respect to R_L is zero. Equating the right-hand side expression (RHS) of (3.10) to zero, we get:

$$\begin{aligned} &(R_{Th} + R_L)^2 + (X_{Th} + R_L \tan\phi)^2 \\ &= R_L\left(2(R_{Th} + R_L) + 2(X_{Th} + R_L \tan\phi)\tan\phi\right) \end{aligned} \tag{3.11}$$

Equation (3.11) can be expanded as follows:

$$\begin{aligned} &R_{Th}^2 + R_L^2 + 2R_{Th}R_L + X_{Th}^2 + R_L^2 \tan^2\phi + 2X_{Th}R_L \tan\phi \\ &= 2R_L R_{Th} + 2R_L^2 + 2R_L X_{Th} \tan\phi + 2R_L^2 \tan^2\phi \end{aligned} \tag{3.12}$$

Equation (3.12) can be further simplified to get the final impedance magnitude matching condition for a constant source connected to a fixed power factor load.

$$\begin{aligned} &R_{Th}^2 + X_{Th}^2 = R_L^2 + R_L^2 \tan^2\phi \\ &\therefore |Z_{Th}|^2 = |Z_L|^2 \\ &\therefore |Z_{Th}| = |Z_L| \end{aligned} \tag{3.13}$$

Hence once the Thévenin equivalent parameters are obtained, assuming the power-factor of the load remains constant, the steady-state voltage collapse occurs when $|Z_{Th}|=|Z_L|$ [13], [37]. A common voltage stability index used is $1-|Z_{Th}|/|Z_L|$. When this index is closer to 1.0, the system is in a stable operating region; whereas an index closer to 0 indicates that the system is close to steady-state voltage collapse. Some researchers use the fact that at the SNBP, the voltage drop across the Thévenin impedance is the same as the load voltage, i.e. $E_{Th} - V = V$ and thus define the voltage stability index as $|(E_{Th} - V)/V|$ [41] or $|V|/|E_{Th} - V|$ [25], which when closer to 1.0. is indicative of the system's proximity to voltage collapse. Some other indices (using the same underlying principle of maximum power transfer) such as power margin have been used in [36], [14]. Wide-area measurements have been proposed to be used wherein system-wide installed PMUs send their data to a central computer and Thévenin equivalents are built at all the monitored buses to estimate the voltage stability margin [50]. Multi-bus equivalent networks have been built using the measurements in a load area to estimate the voltage stability margin in order to better account for the different limits of individual tie-lines connecting the load area to the rest of the network [24], [38], [43] - [45]. Effort has been focused on accurately estimating the Thévenin equivalent parameters from measurements in [16], [46], [47]. A comparison of different methods using local measurements or wide-area measurements to estimate the voltage stability margin has been performed, in terms of their computational costs and the PMU coverage required to be able to reliably estimate the SNBP using such measurement-based methods (including methods that involve building multi-bus equivalent networks), in [26], [17].

It can be shown that the Thévenin impedance obtained from (3.2) is actually the incremental source impedance (also known as differential impedance). The incremental source impedance Z_{diff} is given by (3.14) where v is the voltage across the impedance and i is the current flowing through the impedance.

$$Z_{diff} = \frac{dv}{di} = \frac{v_2 - v_1}{i_2 - i_1} \tag{3.14}$$

The voltage across the impedance and the current flowing through it can be substituted into (3.14) to get:

$$Z_{diff} = \frac{(E_{Th} - V_2) - (E_{Th} - V_1)}{(I_2 - I_1)} = \frac{(V_1 - V_2)}{(I_2 - I_1)} \tag{3.15}$$

It is seen from (3.2) and (3.15) that the measurement-based method calculates the incremental source impedance. However, since the Thévenin source is assumed to be linear, its impedance is the same as its incremental impedance. Additionally, the E_{Th} calculated using (3.3) is not actually the open-circuit voltage at the bus-of-interest as obtained from the full network. It is obtained using only local measurements, without any information about the rest of the network and it will be shown that the behavior of E_{Th} calculated using (3.3) as the load increases can be counter-intuitive in some cases wherein the $|E_{Th}|$ increases as the system load increases. Also the Z_{Th} obtained using measurements is not the same as V_{OC}/I_{SC}, where V_{OC} is the open-circuit voltage at the bus and I_{SC} is the short-circuit current at the bus. In fact it is quite likely that in the presence of nonlinear injections, a power-flow problem will not have a solution if the bus-of-interest is short-circuited and hence it is not possible to calculate the I_{SC}. Additionally, since only local load measurements are used in this method, the power supplied by the Thévenin source is only sufficient to meet the local load and the losses due to Z_{Th}, and hence the slack-bus power is not preserved in the Thévenin equivalent.

It is observed that the behavior of the E_{Th} and Z_{Th} as the load increases depends on the bus-of-interest. For example, if the IEEE 14-bus system is modified, such that all non-slack buses are PQ buses with positive loads, the behavior of Z_{Th} and E_{Th} as the load increases, is different at different buses in the system. The two distinct pseudo-measurements necessary to calculate Z_{Th} at each load-scaling factor λ, are obtained by solving two power-flow problems when (a) all injections are scaled by λ and (b) all injections (used for the first measurement) are perturbed by 1% of their respective base-case injections. The Newton-Raphson method (MATPOWER [34]) is used to solve both power-flow problems using a convergence tolerance of 10^{-6} MVA. At bus number 4, both $|Z_{Th}|$ and $|E_{Th}|$ increase as the load increases (not considering VAr limits) as shown in Figure 3.3. Contrary to the behavior expected from the "open-circuit voltage", as the load in the network increases the magnitude of the E_{Th} increases, as mentioned earlier. The increase in E_{Th} and Z_{Th} compensate each other such that the voltage at the retained bus (bus number 4 in this case) decreases as the load increases which is expected. However at bus number 13, both $|Z_{Th}|$ and $|E_{Th}|$ decrease as the load increases (not considering VAr limits) as shown in Figure 3.4.

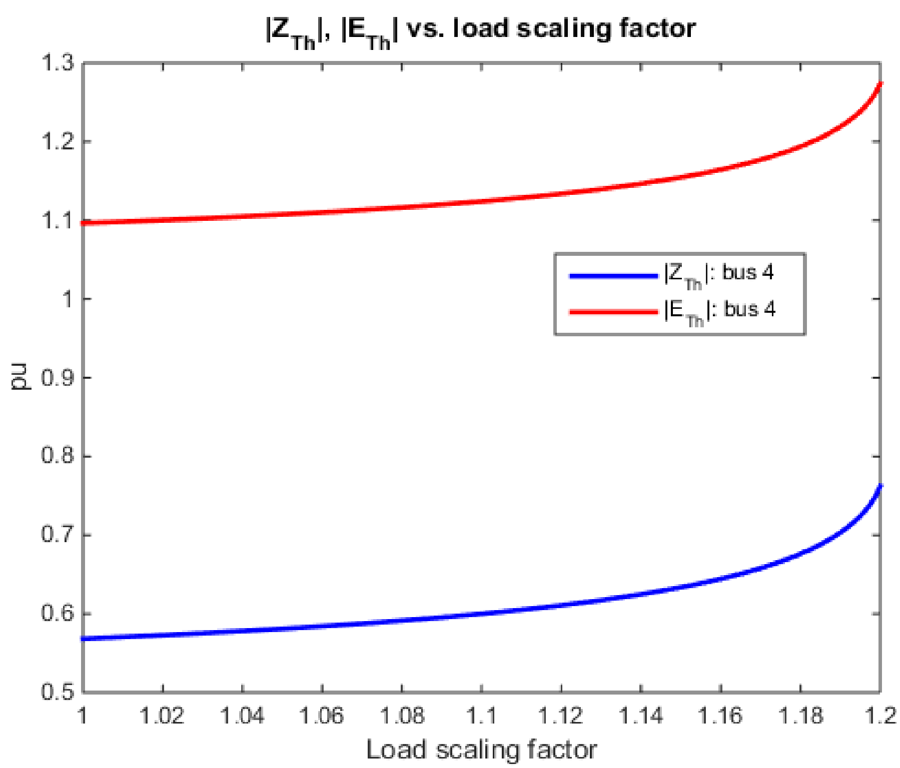

Figure 3.3 $|Z_{Th}|$ and $|E_{Th}|$ at bus number 4 vs. the load-scaling factor when generator VAr limits are ignored

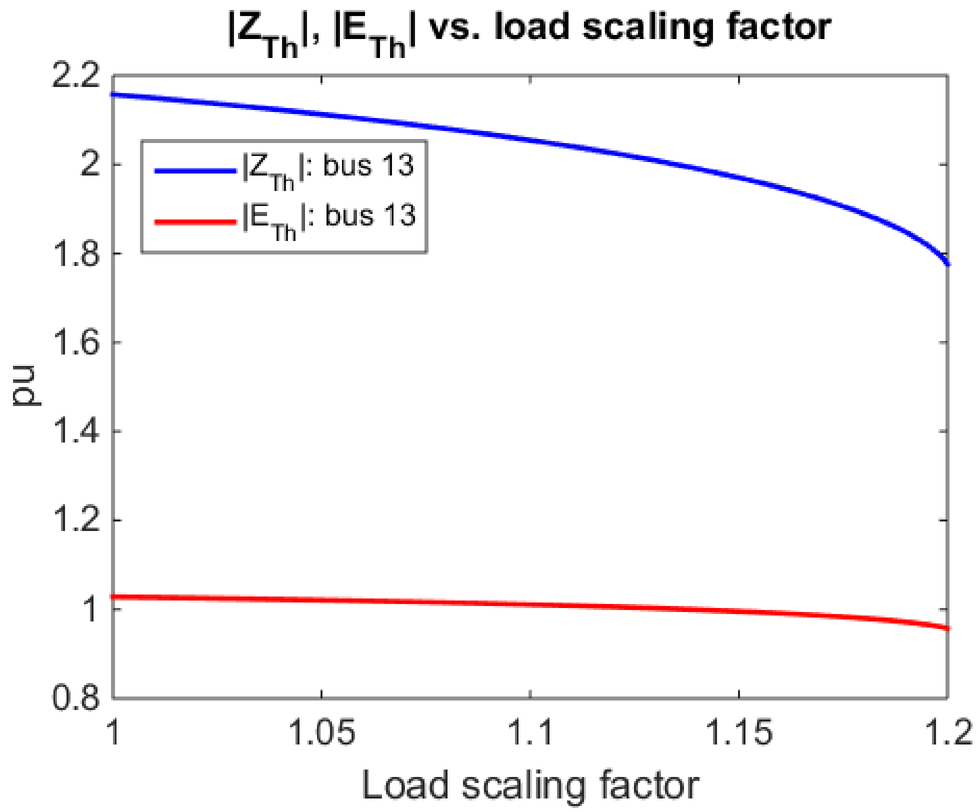

Figure 3.4 $|Z_{Th}|$ and $|E_{Th}|$ at bus number 13 vs. the load-scaling factor when generator VAr limits are ignored

The angle of Z_{Th} does not necessarily increase/decrease uniformly with load as shown in Figure 3.5 where the angle of Z_{Th} at bus number 13 is plotted against the load-scaling factor. This causes the real part of the Z_{Th} to initially decrease as the load increases and then start increasing after a certain point as shown in Figure 3.6.

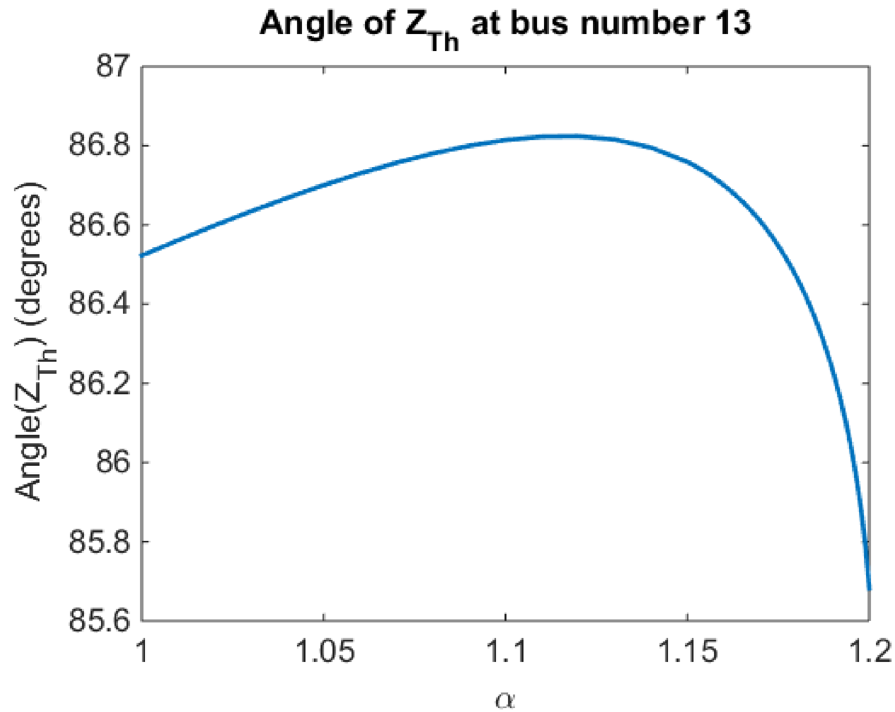

Figure 3.5 Angle of Z_{Th} at bus number 13 vs. the load-scaling factor when generator VAr limits are ignored

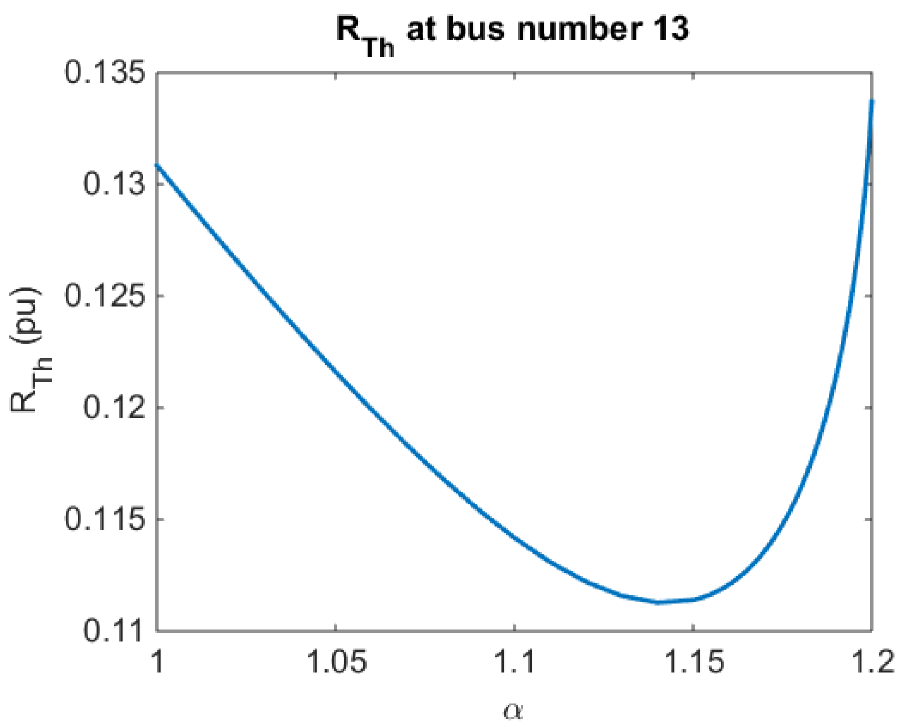

Figure 3.6 R_{Th} at bus number 13 vs. the load-scaling factor when generator VAr limits are ignored

Thus, no general conclusions can be drawn about the behavior of Z_{Th} and E_{Th} as the system load increases, except that the behavior of Z_{Th} and E_{Th} are similar at a given bus.

In order to estimate the steady-state voltage stability margin, the $|Z_L|$ and $|Z_{Th}|$ are plotted on the same graph as shown in Figure 3.7. It is seen that as the load-scaling factor increases, the $|Z_L|$ and $|Z_{Th}|$ approach each other and are very close to each other at the SNBP which occurs at λ= 1.2009 obtained using CPF. In order to ensure that the simulation was able to approach the SNBP as closely as possible, the step-size of the load-scaling factor λ was reduced from 0.01 to 0.001 after λ = 1.15. The $|Z_L|$ and $|Z_{Th}|$ at all buses are very close to each other at the SNBP and Figure 3.7 is a representative plot.

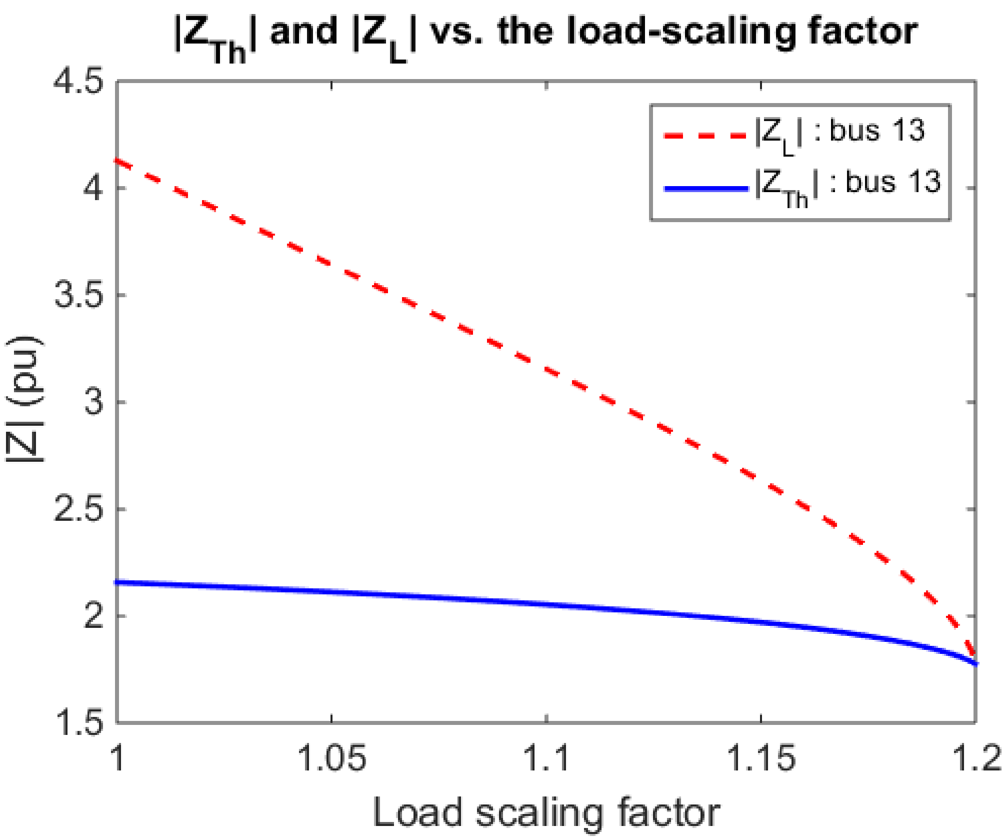

Figure 3.7 Magnitude of Z_L and Z_{Th} at bus number 13 vs. the load-scaling factor when generator VAr limits are ignored

In the following section, the effect of discrete changes on the purely local-measurement-based methods of estimating the SNBP will be demonstrated.

3.2 Effect of discrete changes on local measurement-based methods of estimating the steady-state voltage stability margin

In order to demonstrate the effect of discrete changes on local measurement-based methods of estimating the steady-state voltage stability margin, the IEEE 14-bus system as shown in Figure 3.8 is used.

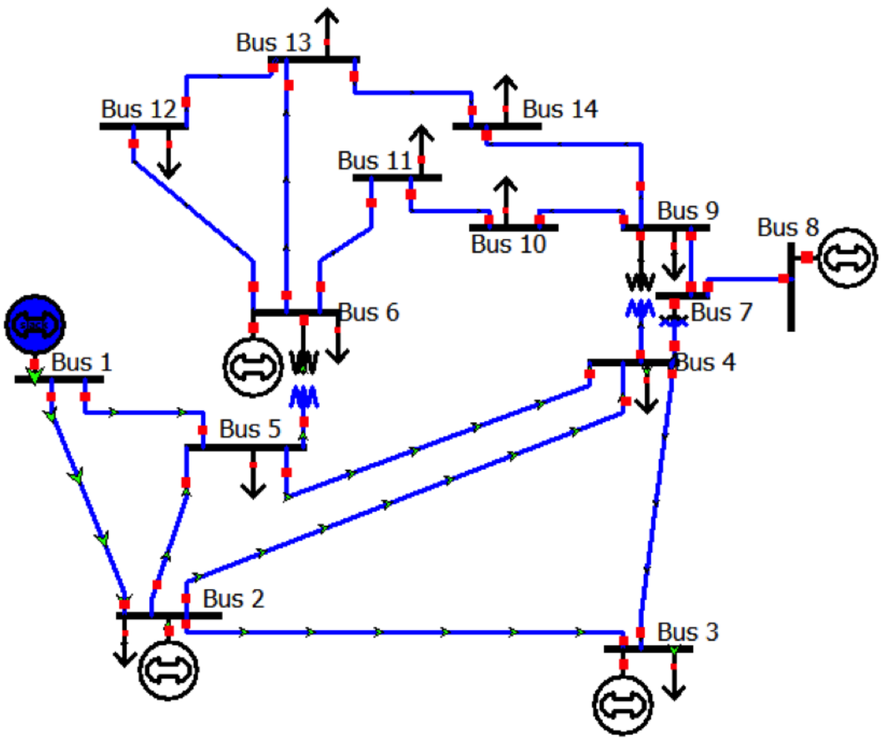

Figure 3.8 IEEE 14-bus system [40]

3.2.1 Effect of generator VAr limits

The impact on the estimated Z_{Th} for the 14-bus system from generators being forced to be on their VAr limits, is shown in Figure 3.9, in which the magnitude of Z_{Th} seen at bus number 4, is plotted against the load-scaling factor which scales all the loads and real-power-generation in the system. The two distinct pseudo-measurements necessary to calculate Z_{Th} at each load-scaling factor λ, were obtained by solving two power-flow problems when (a) all injections were scaled by λ and (b) injections of the PQ buses (used for the first measurement) were perturbed by 0.01% of their respective base-case injections. The Newton-Raphson method (MATPOWER [34]) was used to solve both power-flow problems using a convergence tolerance of 10^{-6} MVA. It is seen from Figure 3.9 that the measurement-based Thévenin impedance increased in magnitude each time a generator was forced to be on its VAr limit, with the discrete increase becoming larger as the number of generators with available VAr capabilities reduced. For this system, up to a 11.65% increase was seen in $|Z_{Th}|$ when any one of the generators reached its respective VAr limit. The SNBP obtained using CPF (MATPOWER [34]) for this system occurs at a load-scaling factor of 1.7780. In order to ensure the simulated results were able to approach the SNBP as closely as possible, the step-size of the load-scaling factor λ was reduced from 0.01 to 0.0001 beyond λ = 1.7 and the perturbation added to get the second measurement was also reduced from -10^{-4} to -10^{-6}. The last point at which two measurements were successfully obtained was at λ = 1.7779.

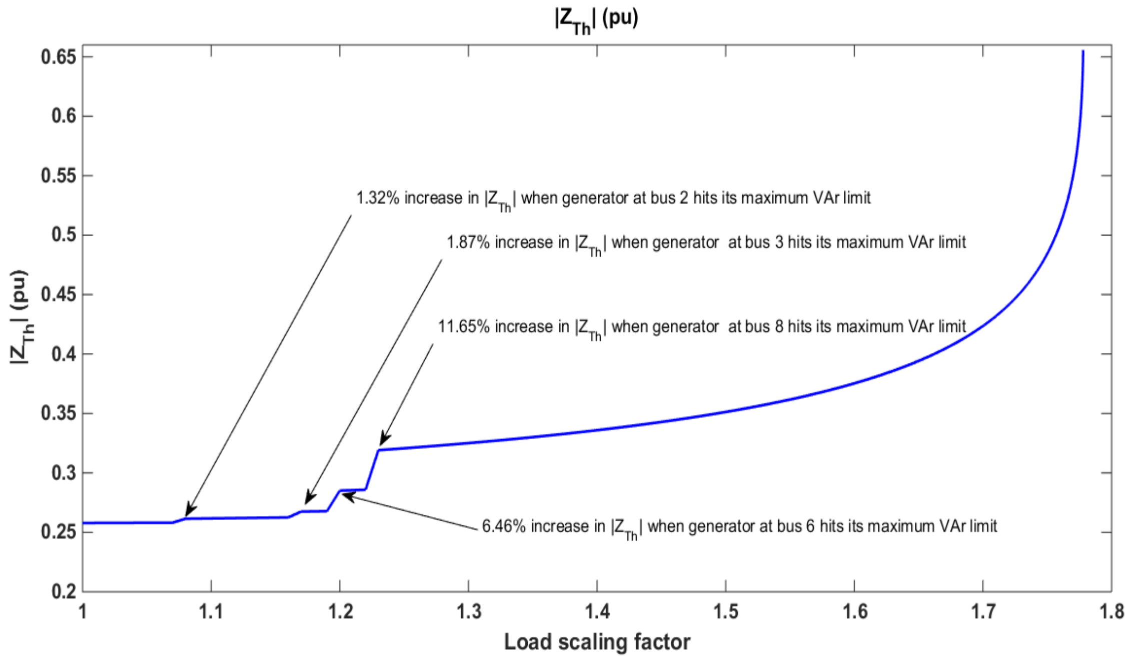

Figure 3.9 Magnitude of Z_{Th} vs. the load-scaling factor when generator VAr limits are respected

It was observed that as the load-scaling factor increased, the E_{Th} at bus number 4 had a similar behavior as that of Z_{Th}. This is shown in Figure 3.10 where the magnitude of E_{Th} is plotted along with the magnitude of Z_{Th} (with the magnitude of Z_{Th} being shifted such that $|E_{Th}|=|Z_{Th\text{-}shifted}|$ at $\lambda = 1.0$).

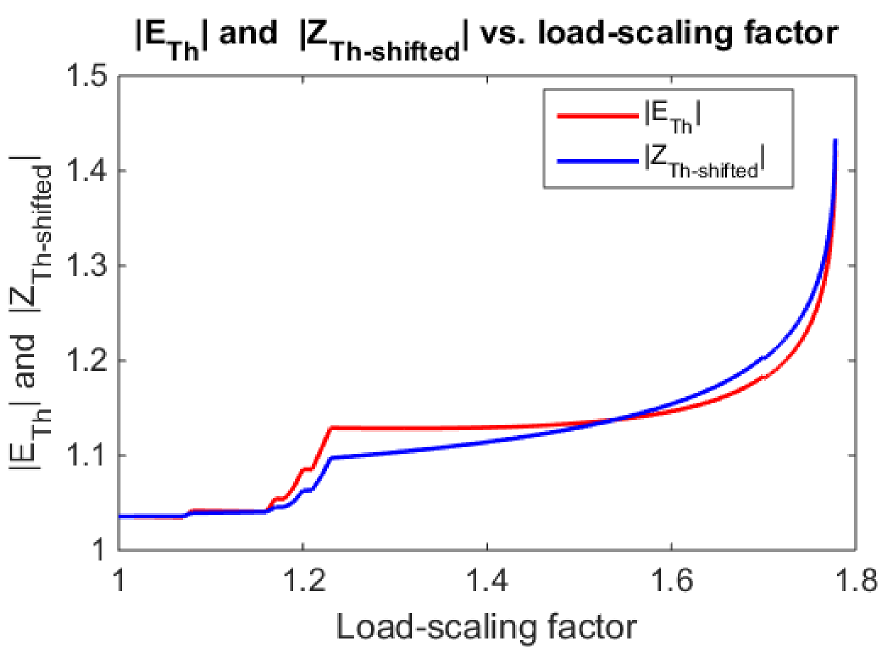

Figure 3.10 Magnitude of E_{Th} and the “shifted” Z_{Th} vs. the load-scaling factor

The proximity of the generator that reaches its VAr limit to the bus-of-interest is expected to play an important role in determining the extent of its impact on the $|Z_{Th}|$ obtained using local measurements at the bus. This can be seen from the percent increase in $|Z_{Th}|$ observed at buses 11, 12 and 13 when different generators reach their maximum VAr limits, tabulated in Table 3.1. For instance, the order of buses that are electrically closest to farthest from bus number 8 are buses 11, 13 and 12. Correspondingly, the order of buses that see the largest to smallest impact on the $|Z_{Th}|$ when the generator at bus 8 reaches its maximum VAr limit is also 11, 13, 12. Similarly, the order of buses that are electrically closest to farthest from bus 6 are buses 13, 11 and 12 and this matches the order of the buses with the largest to smallest increase in $|Z_{Th}|$ when the generator at bus 6 reaches its maximum VAr limit. However one cannot expect a perfect one-to-one correspondence between the order of buses that are electrically closer to a generator and the order of buses that see the largest impact of that generator's VAr limit being reached, in *all* meshed systems. However, buses that are electrically close to a generator reaching its VAr limit are generally expected to undergo a larger change in $|Z_{Th}|$ than those that are significantly farther. It is also observed that the following trend holds true at all buses: as more generators reach their VAr limits, the percent increase in $|Z_{Th}|$ caused by imposing these var limits increases.

Table 3.1 Percent increase in |ZTh| due to VAr limits observed at different buses

Bus number of generator going on VAr limit	Bus-of-interest: 11	Bus-of-interest: 12	Bus-of-interest: 13
Bus 2	0.7%	0.86%	0.81%
Bus 3	0.77%	1.13%	1%
Bus 6	5.21%	4.65%	5.31%
Bus 8	5.9%	5.65%	5.68%

The impedance magnitude matching theorem is seen to hold true (as it should) even in the presence of VAr limits, as shown in Figure 3.11 where the $|Z_L|$ and $|Z_{Th}|$ are plotted on the same plot, with the bus-of-interest being bus number 4. It is seen that as the load-scaling factor increases, the $|Z_L|$ and $|Z_{Th}|$ approach each other and are very close to each other at the SNBP. The small gap between the two at the last point can be attributed to the inability to obtain a converged power-flow solution at two loading conditions that are very close to the SNBP, and also to the approximation involved in assuming that the Thévenin source remains constant over the window of measurements.

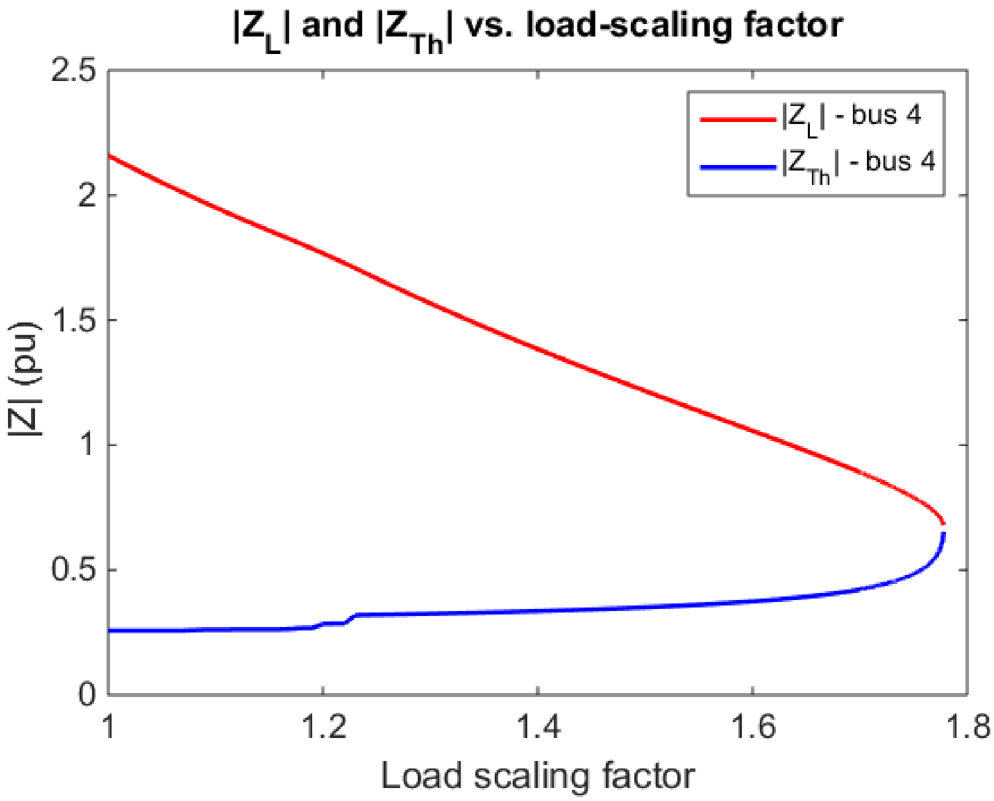

Figure 3.11 Magnitude of Z_L and Z_{Th} at bus number 4 vs. the load-scaling factor when generator VAr limits are respected

It is well-known that if the generator reactive power capabilities are not taken into consideration, the estimated SNBP can be very non-conservative. The $|Z_{Th}|$, with and without VAr limits being considered, is plotted against the load-scaling factor (varying from the base-case through to the respective SNBPs) in Figure 3.12. It is seen that the net increase in the magnitude of the Thévenin impedance due to VAr limits is 154% and that there is a growth factor of 2.2556 between the estimated SNBP without VAr limits over that with VAr limits. Thus, if purely local-measurement-based methods are used to estimate the steady-state voltage stability margin when none of the generators are on VAr limits (for example at λ = 1.0), the estimated margin will be very non-conservative as one cannot predict, based purely on only local measurements, if and when different generators will be forced to be on their respective VAr limits.

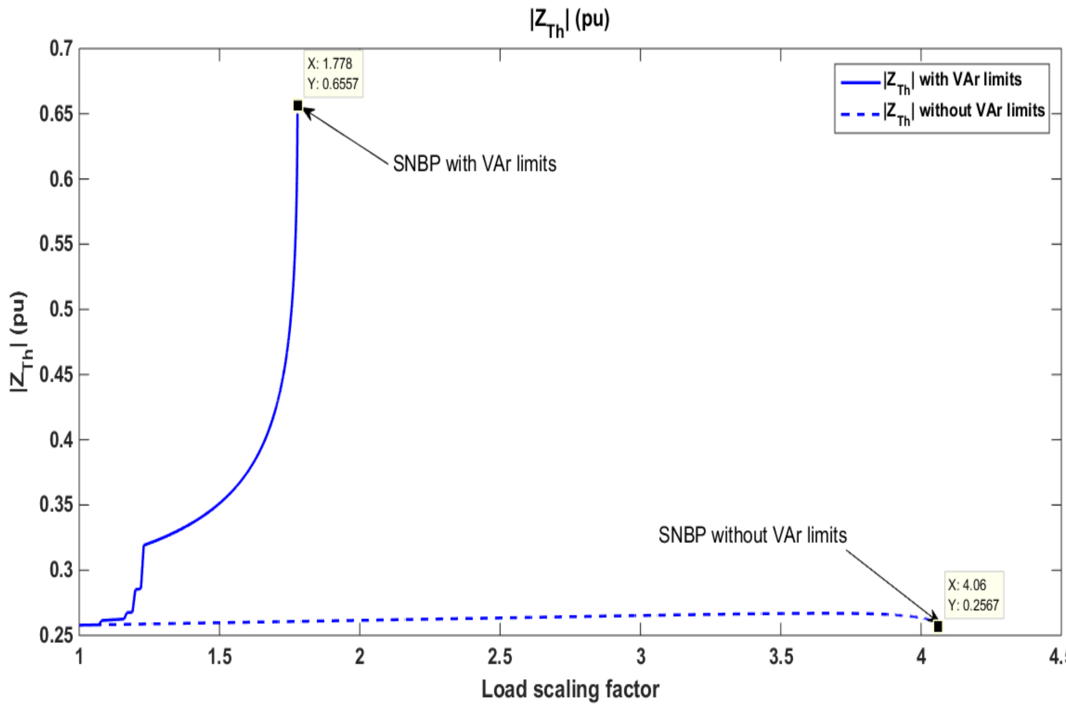

Figure 3.12 Magnitude of Z_{Th} vs. the load-scaling factor with and without VAr limits

Thus, using purely local measurements, one cannot predict all the changes in the magnitude of Z_{Th}, which makes continuous monitoring and updating of local-measurement-based models necessary. More than just local measurements are necessary in order to foresee such discrete changes in the system. This thought is echoed in [42] where information about generator field currents in the system is used to anticipate the activation of over-excitation limiters for generators.

3.2.2 Effect of other discrete changes

In order to judge the impact of other discrete changes in the system such as tap changes, the $|Z_{Th}|$, $|Z_L|$ and $|E_{Th}|$ before and after the following discrete changes are noted:

1. Increasing tap of the transformer between buses 4 and 7 from 0.978 to 1.0.
2. Increasing phase-shift of the transformer between buses 4 and 7 from 0° to 5°.
3. Increasing phase-shift of the transformer between buses 4 and 7 from 0° to 30°. (While such a dramatic discrete change is not expected to occur in a short span of time under typical operating conditions, this change was simulated to observe the extent of the effect that phase-shifting transformers can have on $|Z_{Th}|$.)
4. Switching off a 19 MVAr capacitor bank on bus 9.

The percent change in $|Z_L|$ and $|Z_{Th}|$ caused by each of the above discrete changes is shown in Figure 3.13 and Figure 3.14 respectively. It is seen that in the case where the $|Z_L|$ increases due to a discrete change, $|Z_{Th}|$ also increases, with the increase in $|Z_{Th}|$ being slightly more than the increase in $|Z_L|$. This causes the SNBP to be slightly reduced. Likewise, in the cases where $|Z_L|$ decreases, $|Z_{Th}|$ either increases slightly or also decreases but the decrease in the $|Z_L|$ is more pronounced than that in $|Z_{Th}|$, which again leads to a reduction in the estimated SNBP. It is seen from Figure 3.15 that an increase/decrease in the $|Z_{Th}|$ is also accompanied by an increase/decrease, respectively, in $|E_{Th}|$ (except at buses 4 and 7 when the phase-shift of the transformer is increased to 5°, in which case the percent change in $|Z_{Th}|$ is very small). The effect of the discrete changes on the estimated SNBP is shown in Figure 3.16, where it is clearly seen that the 30° phase shift of the transformer causes the highest reduction in SNBP, however this is a dramatic change which is not expected to occur in a single step in the field.

The goal of this analysis was to determine which types of discrete changes had the greatest effect on the SNBP. It is seen that the effect of discrete changes such as tap changing and phase changing on the estimated SNBP is not as pronounced as the effect of bus-type switching, for the system tested.

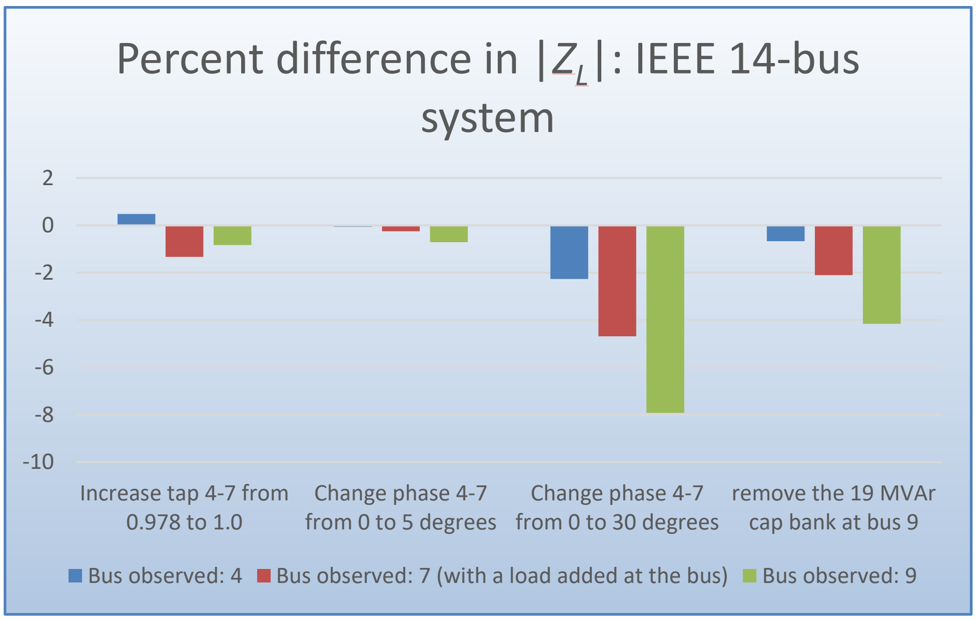

Figure 3.13 Effect of other discrete changes on Z_L

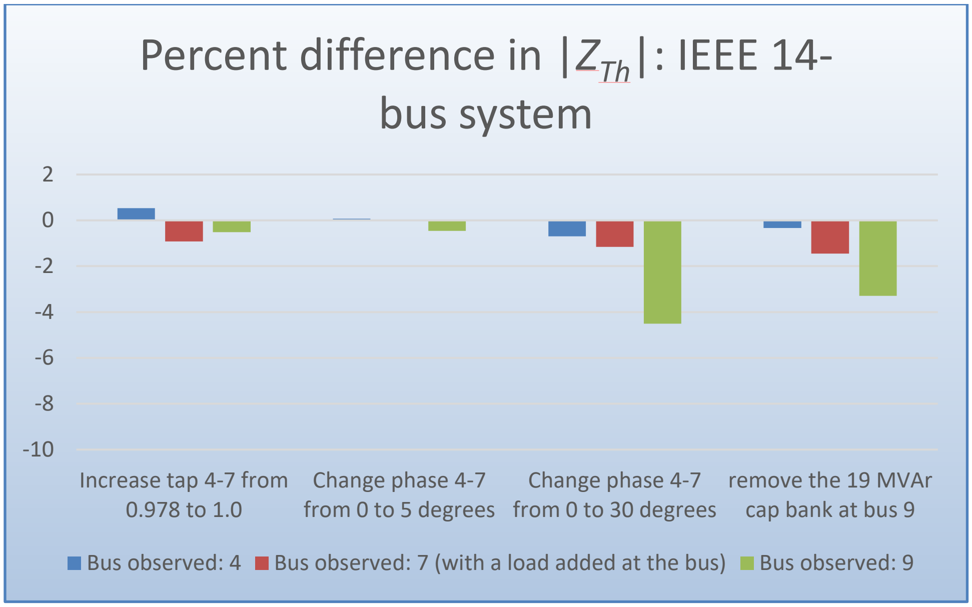

Figure 3.14 Effect of other discrete changes on Z_{Th}

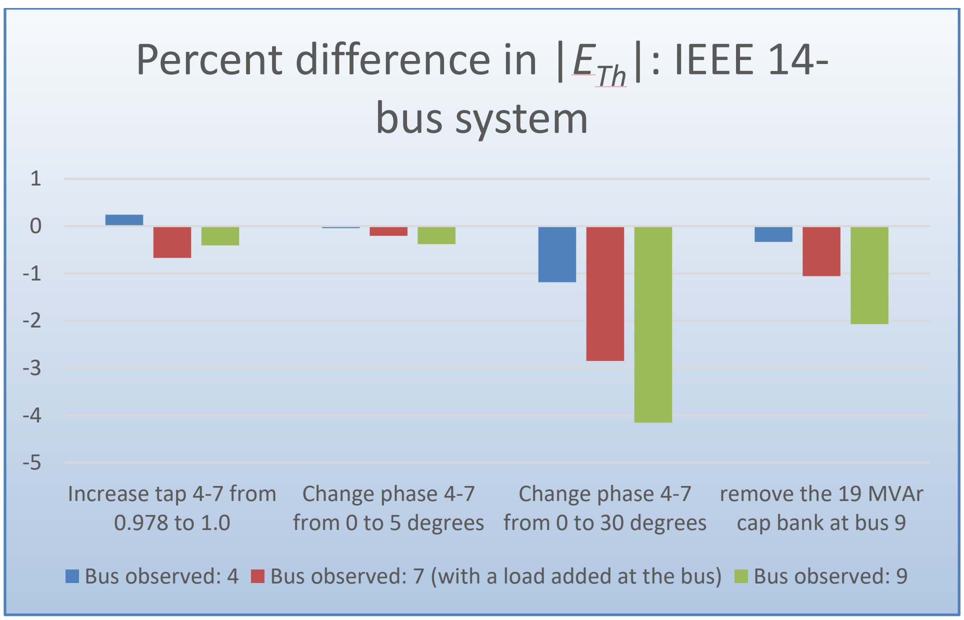

Figure 3.15 Effect of other discrete changes on E_{Th}

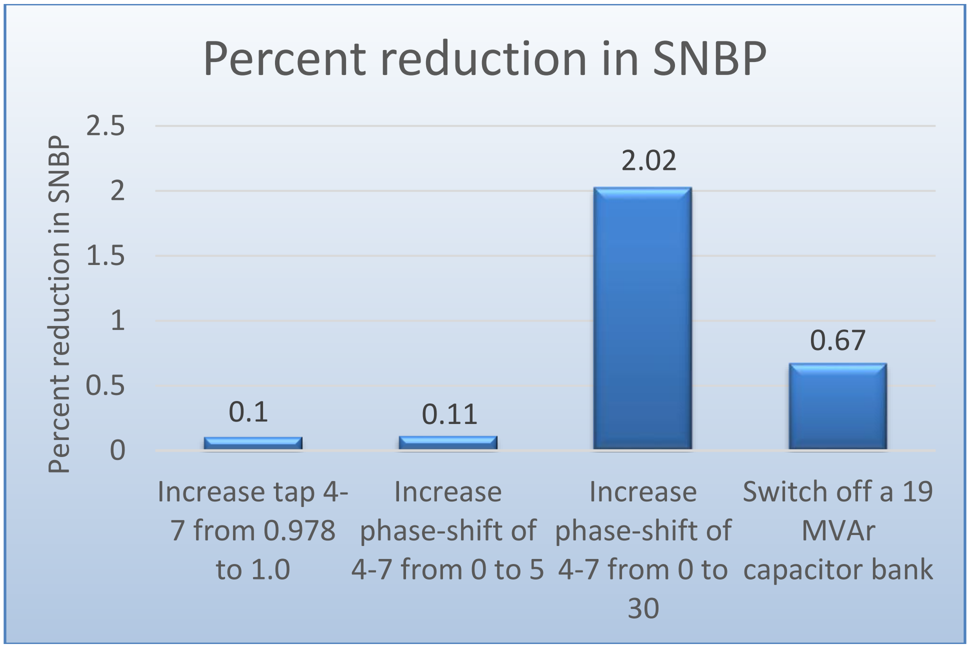

Figure 3.16 Effect of other discrete changes on estimated SNBP

3.2.3 Limit-induced bifurcation points

Another phenomenon that cannot be foreseen based on local measurements alone, is the occurrence of a limit-induced bifurcation point. A limit-induced bifurcation point occurs when a physical limit such as generator VAr limit is reached, and the system loses its steady-state stability despite the Jacobian being non-singular at the point [48]. In fact, the system changes such that one of the eigenvalues of the Jacobian has a positive real part when the limit is encountered, indicating that the operating point is unstable [48]. In other words, the equilibrium point obtained for the operating condition when a generator reaches its VAr limit, coincides with the unstable equilibrium point (low-voltage solution) for the system if the generator had been modeled as a PQ bus to begin with [3], [48], [49]. Due to the operating point being unstable at least momentarily, the likelihood of the system experiencing voltage collapse due to the inevitable small disturbances is at least as high as the possibility of the system converging to a nearby stable equilibrium point [48]. If only local measurements are used, one cannot foresee the occurrence of limit-induced bifurcation points. It is important to note here, that in the numerical experiments reported in [32], with test systems of sizes varying from 14 buses to 2158 buses, the limit induced bifurcation points occurred very close to the SNBP and thus the differences between the loadability limits with or without limit-induced bifurcation points were negligible for all systems tested. Since power systems are not allowed to operate at such high load levels (such that the system is very close to its SNBP), limit-induced bifurcations are possibly not a concern for system operators and this may be more of a theoretical concern than a practical one. However, the results from [32] do not preclude the possibility of such a phenomenon occurring at lower loading levels i.e., theoretically there is no guarantee that a limit-induced bifurcation will *always* occur only at higher loading levels [48]. If they occur at moderate loading levels, not accounting for them could lead to a larger difference in the loadability margin.

In short, *in the presence of discrete changes in the system (which indeed occur in all power systems), voltage stability margin predictions should use both system-based models and local-measurement-based models: the local-measurement-based models should be used to inform and correct the system-based models*.

3.3 Validation of pseudo-measurements obtained using HEPF

It has already been shown that the holomorphic-embedded power flow (HEPF) algorithm can be used to solve power-flow problems and that the solution obtained using HEPF for a given power-flow problem matches that obtained using NR, with the extent of the difference between the two solutions depending on the convergence tolerance used for NR and the number of terms used for HEPF. Since the measurement-based methods calculate the Thévenin voltage and impedance using the voltage and current measurements at the load bus, it naturally follows that the Thévenin voltage and impedance obtained using pseudo-measurements calculated using HEPF (by solving two power-flow problems as explained in section 3.1) will match those obtained when NR is used to obtain the pseudo-measurements. This is shown in Figure 3.17 where the $|Z_L|$ and $|Z_{Th}|$ obtained using NR and HEPF are plotted against the load-scaling factor for the 14-bus system, with the bus-of-interest being bus number 4. It is seen that the $|Z_L|$ and $|Z_{Th}|$ obtained using HEPF match those obtained using NR. A total of 61 terms were used for the HEPF method and a convergence tolerance of 10^{-6} MW was used for the NR method. Generator VAr limits were not considered for this test; however, as long as the same set of buses are on maximum and minimum VAr limits respectively, the Z_L and Z_{Th} obtained using pseudo-measurements using HEPF are expected to match those obtained using NR.

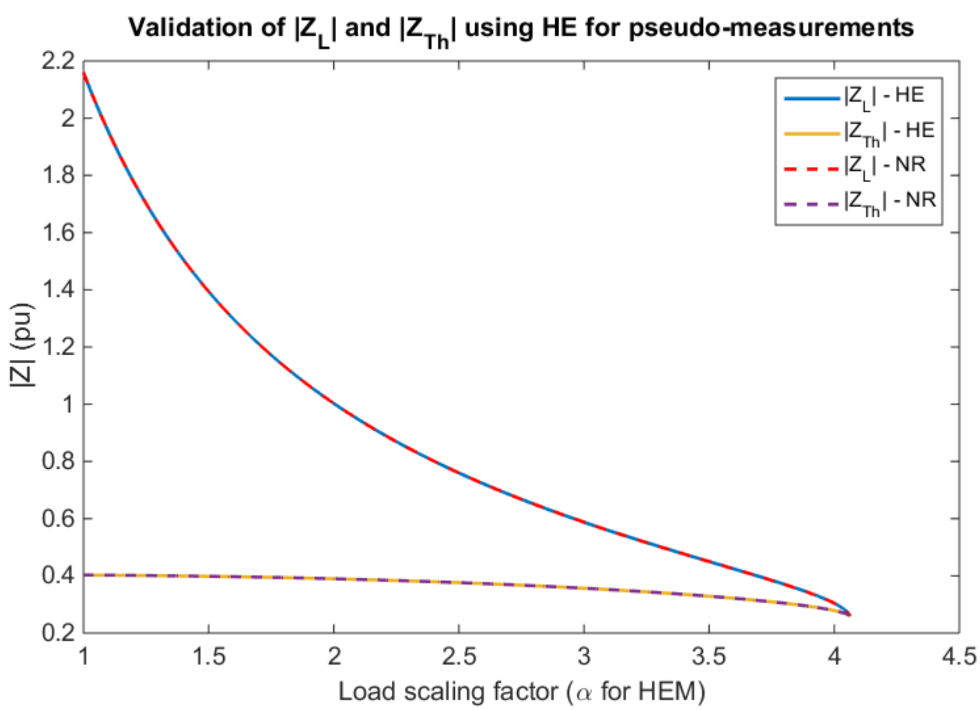

Figure 3.17 Validation of HEPF pseudo-measurements

3.4 Developing a Thévenin-like network using HE reduction

Two-bus equivalent networks for distribution systems that preserve the bus voltage at the retained bus theoretically exactly as long as the load changes along a pre-defined direction have been demonstrated [27]. Multi-bus reduced-order networks for larger meshed systems have been developed in [27], which preserve the voltages at all the retained buses and preserve the system SNBP as long as the load changes along a pre-defined direction. Similar to the HE reduction for distribution systems, the HE reduction for meshed systems also involves solving the full-network power-flow problem using HEPF before proceeding with the network reduction. HE reduction is essentially a nonlinear variation of Ward reduction wherein the injections at the boundary buses are nonlinear functions of α instead of being obtained using linearization at the base case. The topology of the reduced network and the network parameters of the reduced network are the same as those obtained from Ward reduction. HE reduction for meshed systems has been demonstrated on the 14-bus and 118-bus IEEE test systems and a 6057-bus ERCOT system, with approximately a 50% reduction in the network size [27]. Using HE reduction, reduced-order networks can also be built that are structurally similar to the Thévenin networks described in section 3.1, but are nonlinear, i.e., a nonlinear voltage source connected to the load through a constant series impedance, i.e., a series impedance that is not a function of loading level. How would one build such nonlinear Thévenin-like networks and use them to estimate the SNBP will be investigated in the rest of this section 3.4. The advantage of building such a nonlinear network would be that if measurements are eventually used to build the Thévenin-like network, it may better capture the nonlinear behavior of the original system. Fitting a polynomial function to the voltage function at the bus-of-interest using measurements, can also give more information about the expected voltage at that bus under different operating conditions.

3.4.1 Steps involved in obtaining the Thévenin-like network

Consider a simple four-bus system as shown in Figure 3.18 with the bus-of-interest being bus number 3 (i.e. the farthest bus from the slack bus). The parameters for this system are provided in Table 3.2.

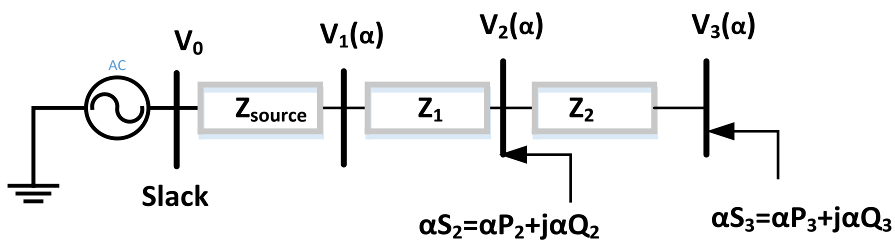

Figure 3.18 Four-bus system

Table 3.2 System parameters for four-bus system

Parameter name	Value	Parameter name	Value
S_2	50.0 + 10.0j (MVA)	Z_{Source}	0.01j (Ω-pu)
S_3	10.0 + 5.0j (MVA)	V_0	1.0 pu
Z_1	0.01 + 0.1j (Ω-pu)	MVA_{Base}	100 MVA
Z_2	0.02 + 0.2j (Ω-pu)		

The first step to obtain the Thévenin-like network is to reduce the original system to a three-bus network as shown in Figure 3.19, obtained by eliminating bus number 2 using HE reduction. The current injection at bus number 2, $I_2(\alpha)$ is given by:

$$I_2(\alpha) = \frac{\alpha S_2^*}{V_2^*(\alpha^*)} \tag{3.16}$$

The functions $I_{1\_2}(\alpha)$ and $I_{3\_2}(\alpha)$ represent the parts of the external (nonlinear) current injections (i.e., $I_2(\alpha)$), that are moved to the boundary buses, i.e., bus 1 and bus 3, respectively, for this system. The reason bus 1 is retained in the reduced network (and this is important) is to avoid a part of the external current injection being moved to the slack bus, since the system effects of such a current source (in parallel with a voltage source at the slack bus) are lost and the model, therefore, becomes incorrect. Note that at this stage, the slack bus power in the reduced network is the same as that in the original full network.

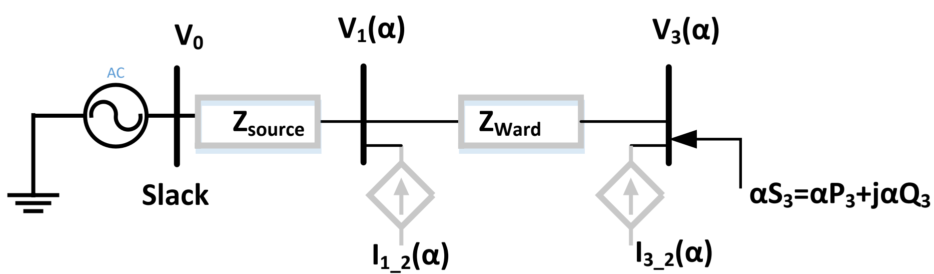

Figure 3.19 HE-reduced network

Once a network with a structure as shown in Figure 3.19 is obtained (and this topology is what we will obtain even for more complex network reductions), we need to transform it into a Thévenin-like network. The first step in doing this is to convert the voltage source at the slack bus to a Norton source as shown in Figure 3.20.

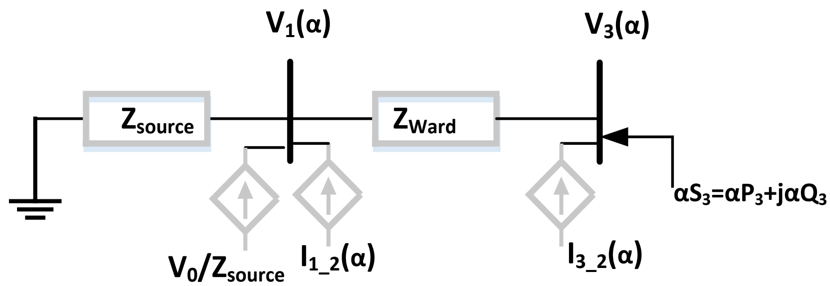

Figure 3.20 Step1 of getting a Thévenin-like network from the HE-reduced network

Though Thévenin-Norton conversions have been shown to be strictly valid for only linear systems, one can show that the conversion shown in Figure 3.20, preserves the load voltage and current profiles. The net current flowing into bus 1 in the reduced network shown in Figure 3.19 should be zero and is given by I_{in_1}:

$$I_{in\_1} = \frac{V_0 - V_1(\alpha)}{Z_{Source}} + I_{1\_2}(\alpha) + \frac{V_3(\alpha) - V_1(\alpha)}{Z_{Ward}} \tag{3.17}$$

The current flowing into bus 1 in the network shown in Figure 3.20 is:

$$I_{in\_1\_step1} = -\frac{V_1(\alpha)}{Z_{Source}} + \frac{V_0}{Z_{Source}} + I_{1\_2}(\alpha) + \frac{V_3(\alpha) - V_1(\alpha)}{Z_{Ward}} \tag{3.18}$$

Note that the current injection into bus 1 is the same in both networks as seen from (3.17) and (3.18). Clearly the net injection into bus 3 is also the same in both networks. Hence the load voltage and load current are preserved in this Thévenin-Norton conversion. Given that the roots of the voltage Padé approximants provide a tight upper bound on the SNBP, and that the voltage series in the two networks is the same, it follows that the SNBP of the network is preserved after such a Thévenin-Norton conversion. The net current injection at bus 1 in Figure 3.20 can then be converted to a voltage source using a Norton-to-Thévenin conversion, as shown in Figure 3.21.

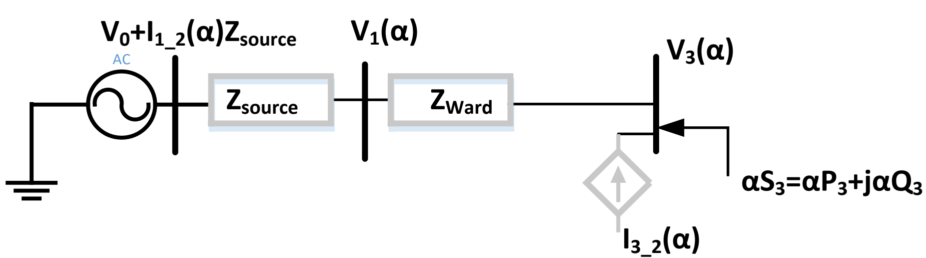

Figure 3.21 Step-2 of getting a Thévenin-like network from the HE-reduced network

It can be shown that this Norton-Thévenin conversion preserves the load voltage and current despite the nonlinear nature of the source. The current flowing into bus 1 in Figure 3.21 is given by:

$$I_{in\_1\_step2} = \frac{V_0 + I_{1\_2}(\alpha) Z_{Source} - V_1(\alpha)}{Z_{Source}} + \frac{V_3(\alpha) - V_1(\alpha)}{Z_{Ward}} \tag{3.19}$$

Note that the current injection into bus 1 is the same in the networks shown in Figure 3.20 and Figure 3.21 as seen from (3.18) and (3.19). Hence the load voltage, load current as well as the system SNBP are preserved through the Norton-Thévenin conversion. The voltage source can then be converted again to a current source (again while preserving the load characteristics and the system SNBP as shown earlier) as shown in Figure 3.22.

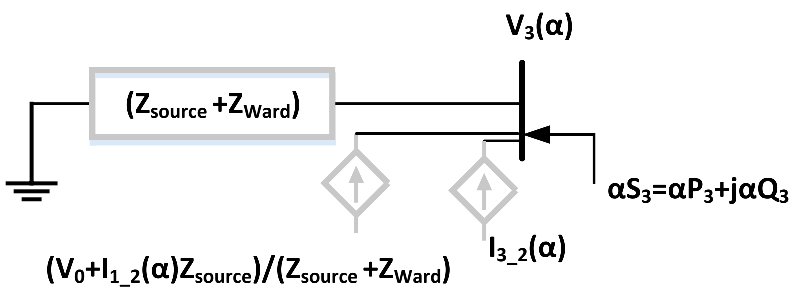

Figure 3.22 Step-3 of getting a Thévenin-like network from the HE-reduced network

The net current injection at bus 3 can then be converted back to a voltage source, as shown in Figure 3.23, which is the Thévenin-like network consisting of a variable voltage source $V_{source}(\alpha)$, connected to the bus-of-interest through a constant impedance.

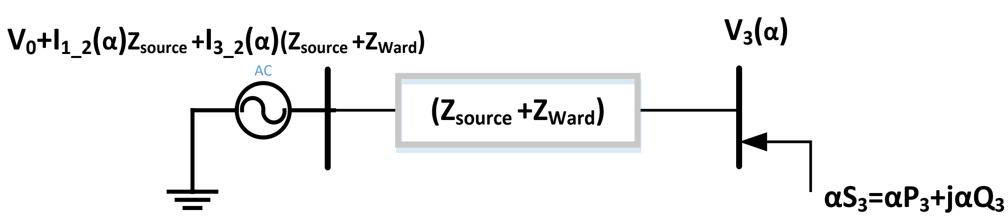

Figure 3.23 Final step of getting a Thévenin-like network from the HE-reduced network

Note that when such Thévenin-Norton conversions are performed, the slack bus power is no longer preserved, i.e., it does not match the slack bus power from the full network. Additionally, similar to the measurement-based Thévenin equivalent, the source voltage, $V_{source}(\alpha)$, is not the open-circuit voltage at the bus-of-interest (if the uniform scaling HEPF formulation is used). If evaluated at α=0, it represents the voltage the bus-of-interest when *all* the buses in the network are open-circuited. One can use the direction-of-change scaling formulation to scale the load only at the bus-of-interest, in which case $V_{source}(\alpha)$ evaluated at α=0, represents the open-circuit voltage at the bus-of-interest. The formulation that one uses to solve the power-flow problem for the whole network depends on the study one wants to perform with the reduced model. Hence depending on the assumptions one makes about the full-model load behavior, one should choose an appropriate scaling formulation. The series impedance of the nonlinear Thévenin-like network is not the same as

V_{OC}/I_{SC} either, it is simply the series combination of Z_{source} and the impedance obtained from Ward reduction i.e. Z_{Ward}. Since the loads are modeled as nonlinear current injections, it is not surprising that the series impedance is a constant that is independent of the system loading condition. Instead, it is V_{source} that is a function of α since it is dependent on the external current injections.

While a simple radial 4-bus system was used to explain the approach for arriving at the Thévenin-like network, no inherent assumptions are made that would restrict this approach to radial systems. Results will be demonstrated on the meshed 14-bus system in the following sections.

Numerically validating the foregoing approach is an important component of the research approach. In order to validate the foregoing Thévenin-like network with a nonlinear voltage source, obtained using HE reduction, the power-flow problem is solved for this reduced network to obtain the voltage at the retained bus. The voltage solution obtained from the reduced network is compared with the full network solution for the four-bus system at different load-scaling factors up to the SNBP (estimated at load-scaling factor = 5.0243, using CPF). It was seen that the voltage solution from the Thévenin-like network matched that obtained from the full network at all loading levels as shown in Figure 3.24 and Figure 3.25 in which the voltage magnitudes and voltage angles for the full and reduced networks are plotted against the load-scaling factor. The magnitude of the difference between the voltage at the retained bus obtained from the full network and that obtained from the Thévenin-like network is plotted against the load-scaling factor in Figure 3.26. It is seen that the difference is on the order of 10^{-15} pu at load levels that are not too close to the SNBP.

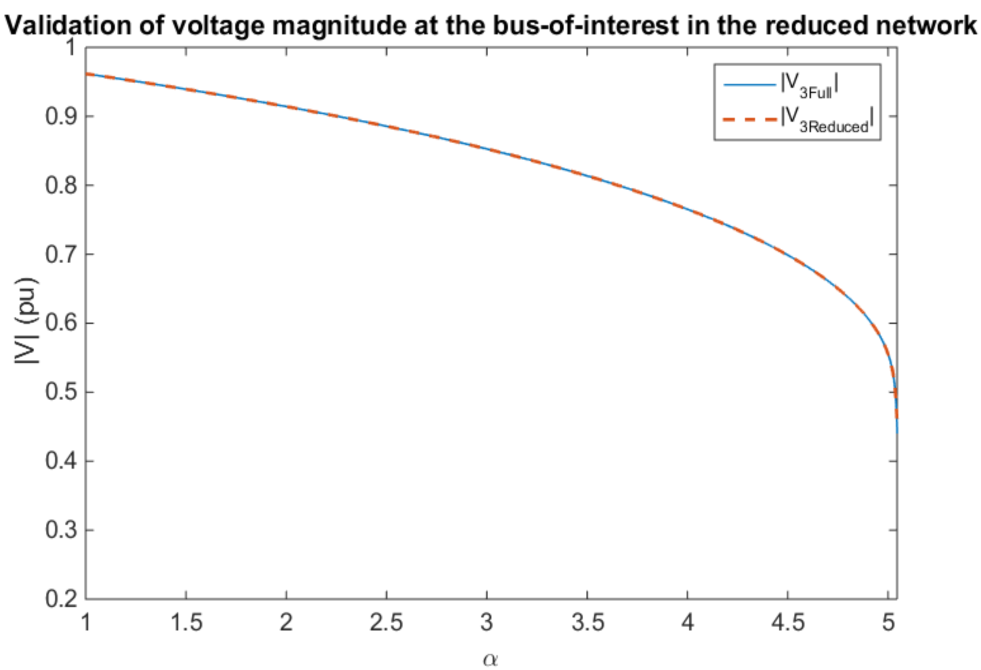

Figure 3.24 Voltage magnitude from Thévenin-like network and full network, 4-bus system

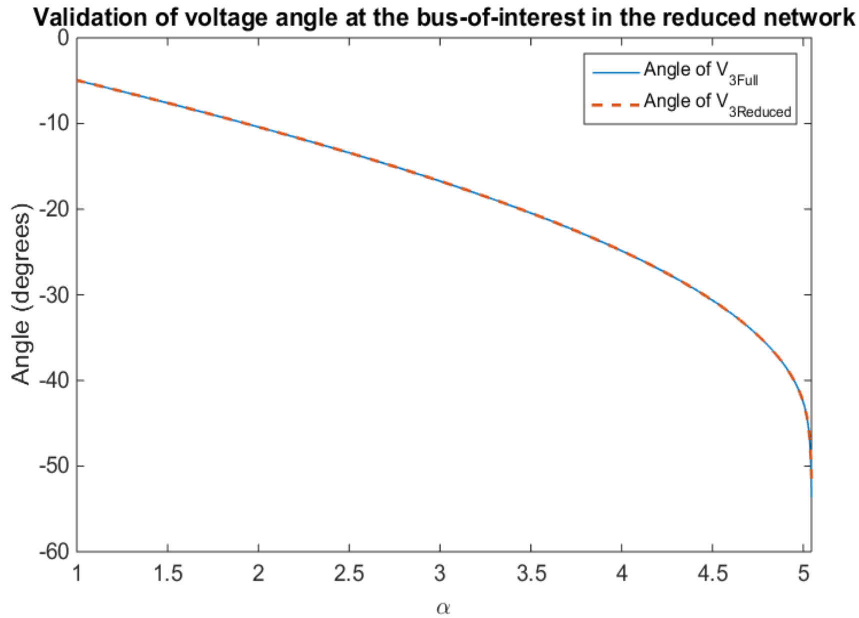

Figure 3.25 Voltage angle from Thévenin-like network and full network, 4-bus system

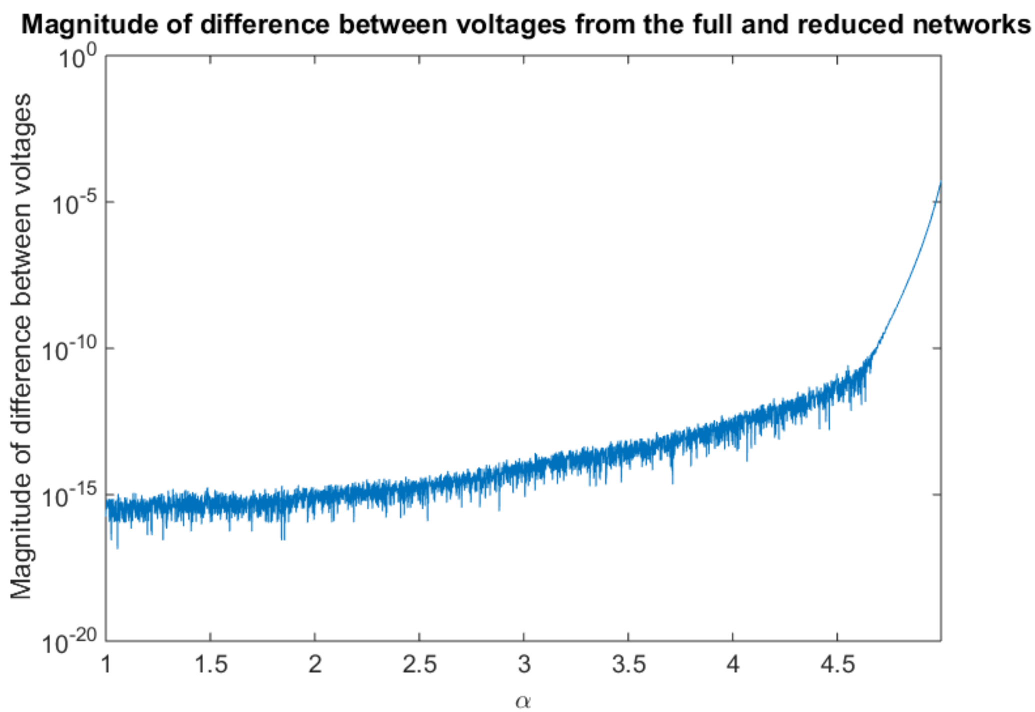

Figure 3.26 Difference between the voltage magnitudes obtained from the Thévenin-like network and the full network, 4-bus system

For a second test case, the IEEE 14 bus system was used. Similarly, the voltage solution from the Thévenin-like network matched that obtained from the full network for the 14-bus system at all loading levels through to the SNBP (estimated to be at load-scaling factor = 4.012, using CPF) as shown in Figure 3.27 and Figure 3.28 in which the voltage magnitudes and voltage angles are plotted respectively for the full and reduced networks against the load-scaling factor, with the bus-of-interest being bus number 4. Note that an additional bus, ‘bus 0’ was added to the system and made the slack bus in the new system, connected to the original slack bus (bus number 1) in the IEEE 14-bus system via the series impedance Z_{source} (assumed to be 0.01j), thus making the total number of buses 15. This system will be referred to as the modified 14-bus system in the rest of the document. The magnitude of difference between the voltage at the retained bus (bus number 4) obtained from the full network and that obtained from the Thévenin-like network for the modified 14-bus system is plotted against the load-scaling factor in Figure 3.29 and it is seen that the differences are very low. The gaps in the plot represent loading levels where the error was exactly zero, when using Matlab’s double precision arithmetic.

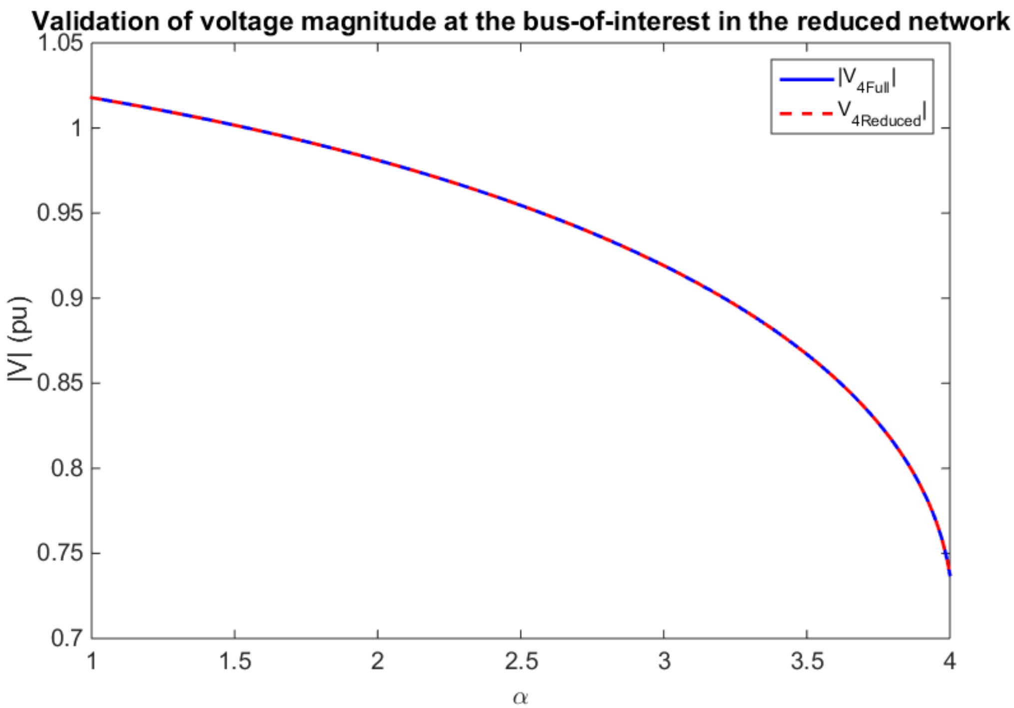

Figure 3.27 Voltage magnitude from Thévenin-like network and full network, modified 14-bus system

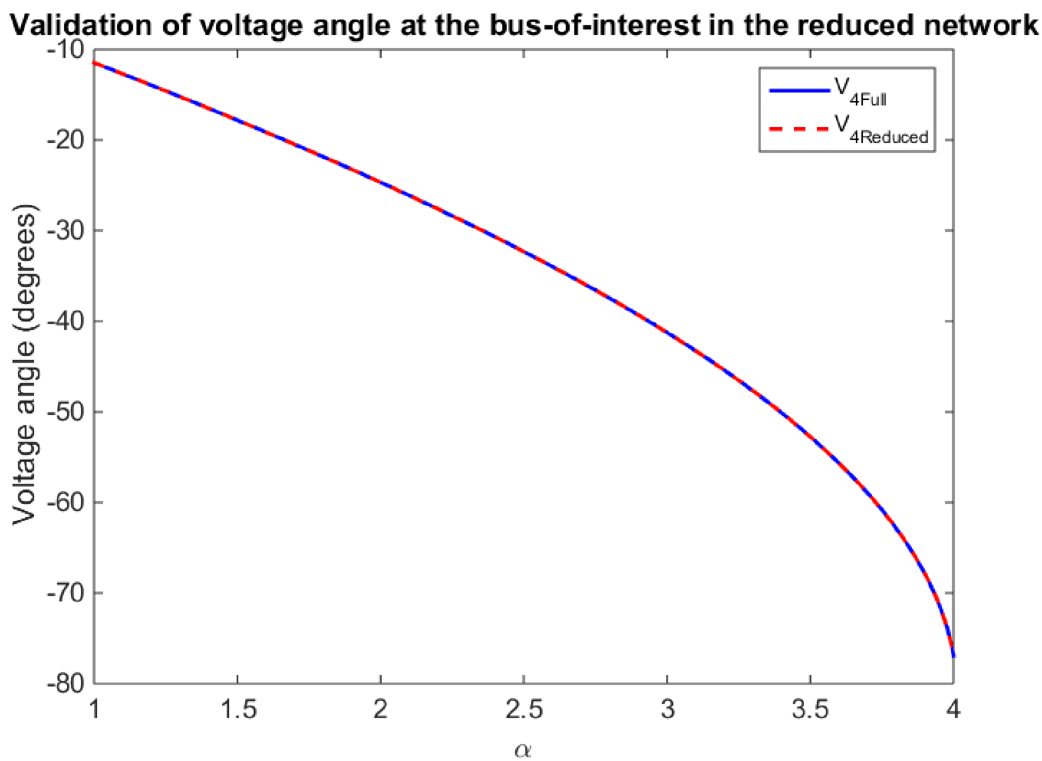

Figure 3.28 Voltage angle from Thévenin-like network and full network, modified 14-bus system

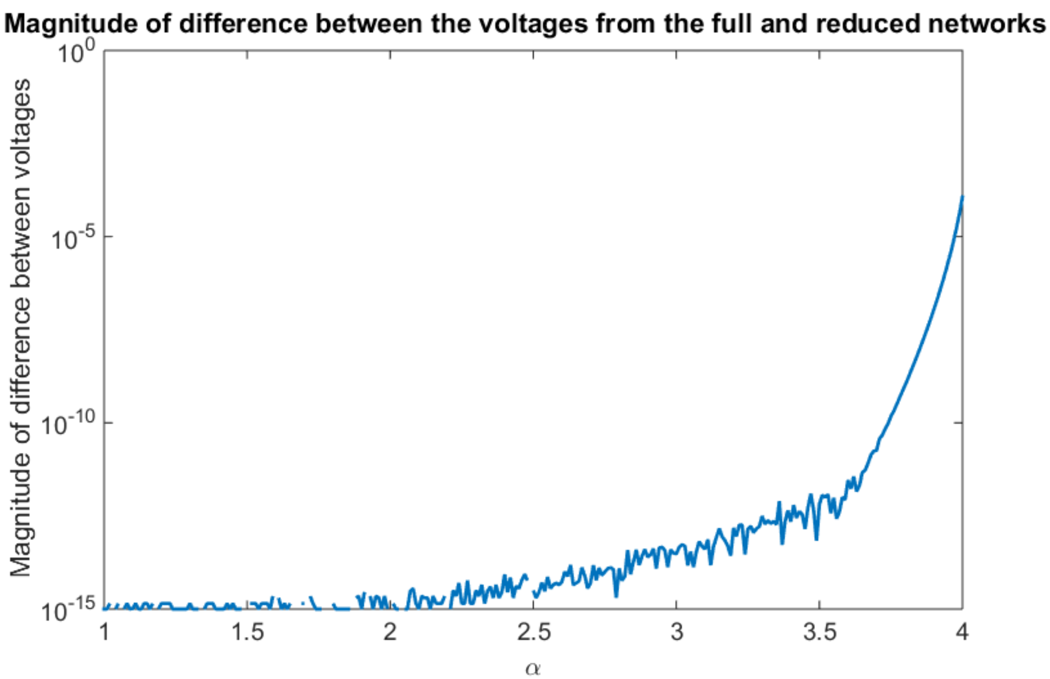

Figure 3.29 Difference between the voltage magnitudes obtained from the Thévenin-like network and the full network, modified 14-bus system

Since the voltage at the retained bus from the Thévenin-like network matches that obtained from the full network, it follows that the local-measurement-based Thévenin network parameters obtained using (3.2) from the reduced network would match that obtained from the full network. This is shown for the modified 14-bus network in Figure 3.30 where the $|Z_L|$ and $|Z_{Th}|$ obtained from the full system and the Thévenin-like network for bus number 4, are plotted against the load-scaling factor. It is seen that the $|Z_L|$ and $|Z_{Th}|$ obtained from the full network match those obtained from the Thévenin-like network.

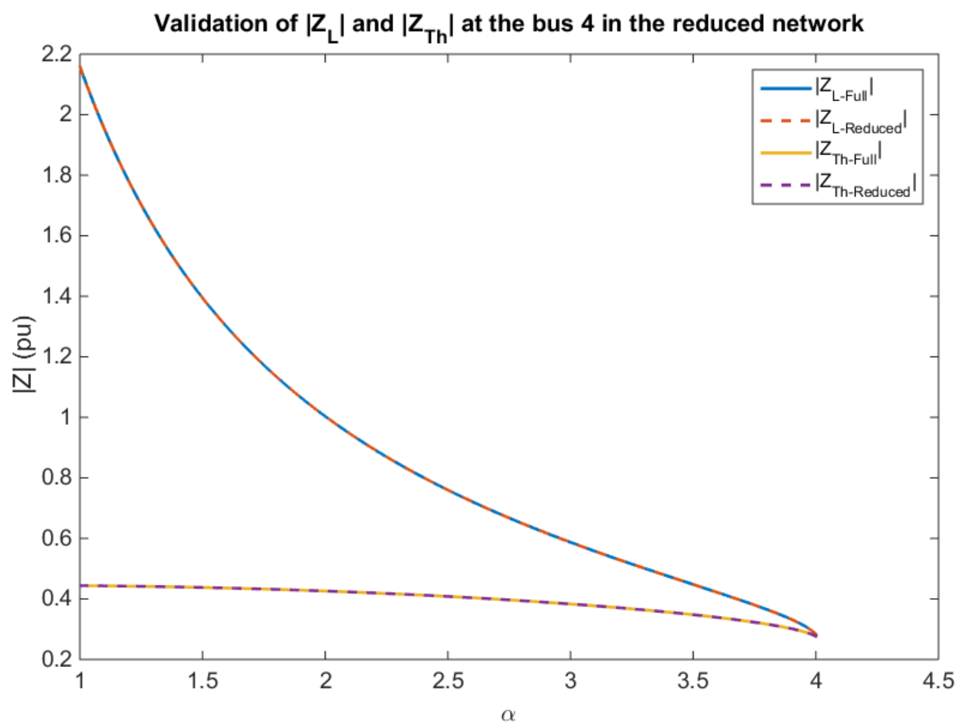

Figure 3.30 Validation of pseudo-measurements from the Thévenin-like network

One aspect of the Thévenin-like network obtained using HE reduction is the behavior of the voltage source as the system load increases. It was shown in section 3.1 that if the IEEE 14-bus system is modified, such that all non-slack buses are PQ buses with positive loads, at some of the buses the E_{Th} increases as the load increases, which is counter-intuitive. For the modified 14-bus system with an additional slack-bus '0', if all possible (14) two-bus nonlinear Thévenin equivalents are generated, it is shown in Figure 3.31, that the magnitudes of the voltage sources in the nonlinear Thévenin-like networks decrease as the load increases. Similar decreasing behavior was also observed for the IEEE 14-bus system with PV buses.

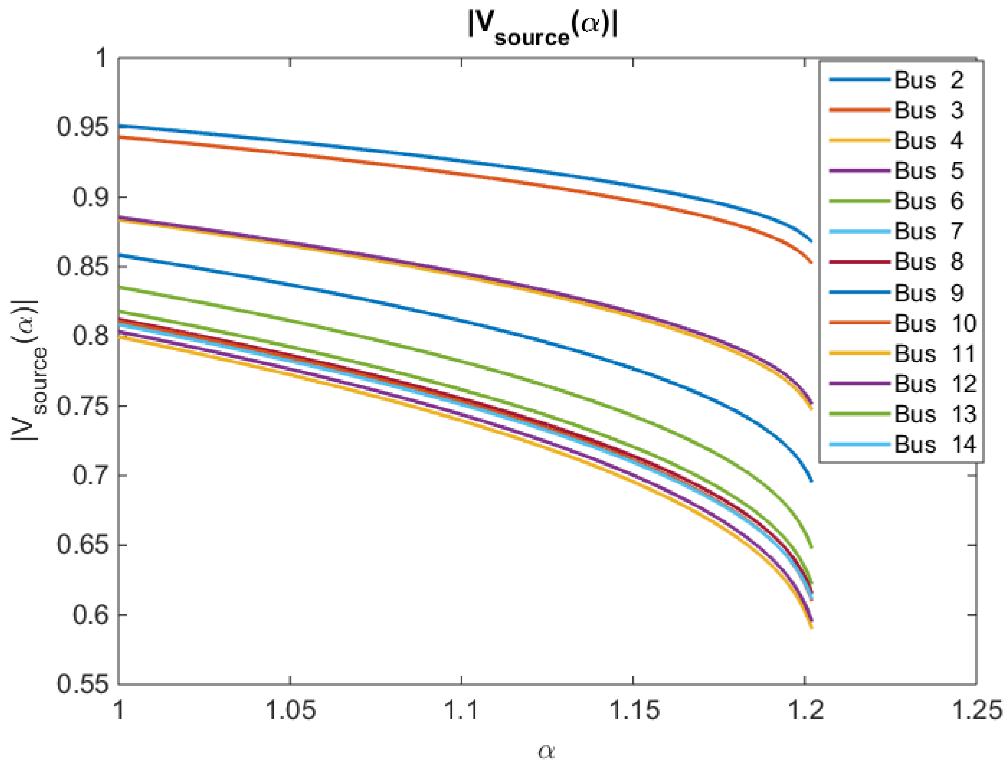

Figure 3.31 Magnitude of $V_{source}(\alpha)$ vs. α

3.4.2 Impact of modeling loads as nonlinear currents or nonlinear impedances

In the numerical results demonstrated in section 3.4.1, the loads were modeled as nonlinear current injections. However, it is possible to model the loads as nonlinear impedances as well. This can be shown by replacing $I_{3\_2}(\alpha)$ (the external current injection at bus 3) in Figure 3.21 by an equivalent nonlinear impedance given by (3.20) as shown in Figure 3.32.

$$Z_{3\_2}(\alpha) = -\frac{V_3(\alpha)}{I_{3\_2}(\alpha)} \tag{3.20}$$

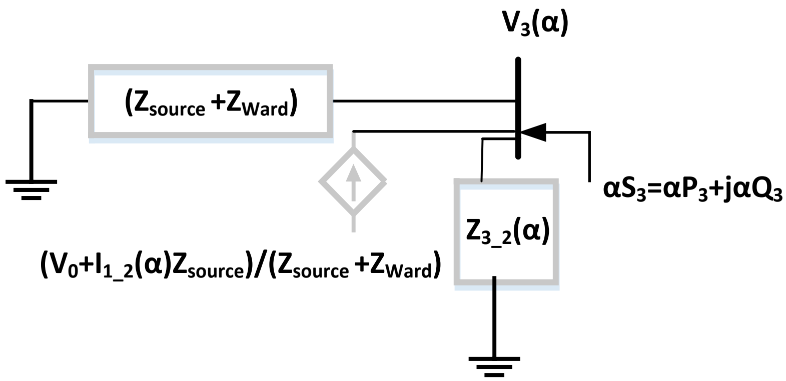

Figure 3.32 Load modeled as nonlinear impedance in step-3 of getting a Thévenin-like network

The effective series impedance in the resultant Thévenin-like network is then a parallel combination of $Z_{3\_2}(\alpha)$ with $(Z_{source}+Z_{Ward})$. The Thévenin-like network will appear as shown below.

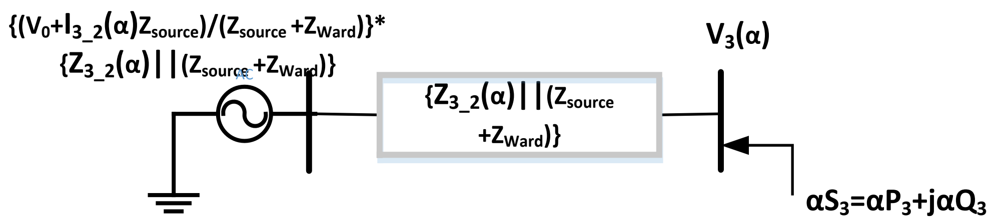

Figure 3.33 Load modeled as nonlinear impedance in step-3 of getting a Thévenin-like network

Note that in the above network, the voltage source as well as the series impedance as nonlinear functions of α. The current flowing into bus 3 in the above network is given by:

$$I_{in\_3\_nonlinearZ} = \frac{\dfrac{\left(V_0 + I_{1\_2}(\alpha) Z_{Source}\right)}{\left(Z_{Source} + Z_{Ward}\right)} * \left\{\dfrac{\left(Z_{Source} + Z_{Ward}\right) \cdot Z_{3\_2}(\alpha)}{\left(Z_{Source} + Z_{Ward} + Z_{3\_2}(\alpha)\right)}\right\} - V_3(\alpha)}{\left\{\dfrac{\left(Z_{Source} + Z_{Ward}\right) \cdot Z_{3\_2}(\alpha)}{\left(Z_{Source} + Z_{Ward} + Z_{3\_2}(\alpha)\right)}\right\}} + \frac{\alpha S_3^*}{V_3^*\left(\alpha^*\right)} \tag{3.21}$$

By substituting the expression for $Z_{3\_2}(\alpha)$ from (3.20) into (3.21), one gets

$$
\begin{aligned}
&I_{in\_3\_nonlinearZ} \\
&= \frac{\left(V_0 + I_{1\_2}(\alpha) Z_{Source}\right)}{\left(Z_{Source} + Z_{Ward}\right)} - \frac{V_3(\alpha)}{\left\{ \dfrac{\left(Z_{Source} + Z_{Ward}\right) \cdot \dfrac{\left(-V_3(\alpha)\right)}{I_{3\_2}(\alpha)}}{\left(Z_{Source} + Z_{Ward} + \dfrac{\left(-V_3(\alpha)\right)}{I_{3\_2}(\alpha)}\right)} \right\}} + \frac{\alpha S_3^*}{V_3^*\left(\alpha^*\right)}
\end{aligned}
\tag{3.22}
$$

By further simplification of (3.22) as given below, one can show that the net current flowing into bus 3 in the network given by Figure 3.33 is the same as that in the network given by Figure 3.23.

$$
\begin{aligned}
&I_{in\_3\_nonlinearZ} \\
&= \frac{\left(V_0 + I_{1\_2}(\alpha) Z_{Source}\right)}{\left(Z_{Source} + Z_{Ward}\right)} - \frac{V_3(\alpha)}{\left\{ \dfrac{\left(Z_{Source} + Z_{Ward}\right) \cdot \left(-V_3(\alpha)\right)}{\left(\left(Z_{Source} + Z_{Ward}\right) I_{3\_2}(\alpha) - V_3(\alpha)\right)} \right\}} + \frac{\alpha S_3^*}{V_3^*\left(\alpha^*\right)} \\
&= \frac{\left(V_0 + I_{1\_2}(\alpha) Z_{Source}\right)}{\left(Z_{Source} + Z_{Ward}\right)} + \frac{\left(\left(Z_{Source} + Z_{Ward}\right) I_{3\_2}(\alpha) - V_3(\alpha)\right)}{\left(Z_{Source} + Z_{Ward}\right)} + \frac{\alpha S_3^*}{V_3^*\left(\alpha^*\right)} \\
&= \frac{\left(V_0 + I_{1\_2}(\alpha) Z_{Source} - V_3(\alpha)\right)}{\left(Z_{Source} + Z_{Ward}\right)} + I_{3\_2}(\alpha) + \frac{\alpha S_3^*}{V_3^*\left(\alpha^*\right)}
\end{aligned}
\tag{3.23}
$$

This was tested numerically on the modified 14-bus system by solving the power-flow problem for the network given by Figure 3.32 with a nonlinear impedance at the retained bus and it was observed that the voltage series at the bus-of-interest matched the voltage series of that bus from the full-network solution, with an accuracy of the order of 10^{-14} and the system SNBP was preserved as well. This shows that it is not necessary to model the loads as nonlinear current injections that are functions of α but the loads can also be modeled as nonlinear shunt impedances. Given that both the models can be used, there is no obvious motivation to model the loads as impedances because that would make the admittance matrix a function of α, thus making the network reduction very complicated and computationally expensive. Additionally, since the source voltage as well as impedance are nonlinear in this case, if the Maclaurin series are to be estimated using local voltage and current measurements, one would need to fit *two* 40^{th} degree polynomials (the degree of the polynomials would depend on the number of terms needed to accurately estimate the SNBP and 40 is an empirically obtained approximate number) instead of one polynomial. This would make the process more complicated and prone to inaccuracies, particularly in the presence of noisy measurements. Hence, while there is no compulsion to do so, it is recommended that the loads be modeled as nonlinear current injections for ease of computation.

3.4.3 Arbitrary Thévenin-like networks

As demonstrated in section 3.4.1, depending on how the loads are modeled (nonlinear current injections or nonlinear shunt impedances), one can get different Thévenin-like networks, while still preserving the voltage at the load bus and the system SNBP. In fact, one can even model some of the loads as nonlinear shunt impedances and the rest as nonlinear currents. This flexibility can be extended to fixed shunt impedances as well. The traditional way of modeling fixed shunts is to keep them as constants in the admittance matrix while performing the reduction, which would result in fixed shunt impedances appearing in the reduced network. The other way of modeling fixed shunt impedances is to model them as nonlinear current injections given by $-Y_{shunt}V(\alpha)$ before performing the reduction (keeping in mind that all the voltage series from the full network are available before performing the reduction). This would result in a reduced-order network that doesn't have any shunt impedances. Thus there are an infinite number of ways in which some/all the shunt impedances (or even parts of the series impedances if one so desires) can be modeled as nonlinear current injections by suitably multiplying them by the voltage series before performing the HE-reduction. This implies that there are an infinite number of different Thévenin-like networks that can be obtained for any given system. The implication that this has on using measurements to build the Thévenin-like networks is that, one can arbitrarily choose a value for the series impedance and fit the series for the source voltage such that the load behavior at the bus-of-interest is preserved. In order to prove that this can be done, consider a three-bus network obtained using HE-reduction as shown in Figure 3.19, where only the series impedances were retained in the admittance matrix and the shunt impedances were modeled as nonlinear current sources to yield the model of Figure 3.19. The Thévenin-like network would consequently not have any shunt impedances and would appear as shown in Figure 3.23. One can add a shunt impedance at bus 1 to the network shown in Figure 3.23 along with a compensatory current injection as shown in Figure 3.34.

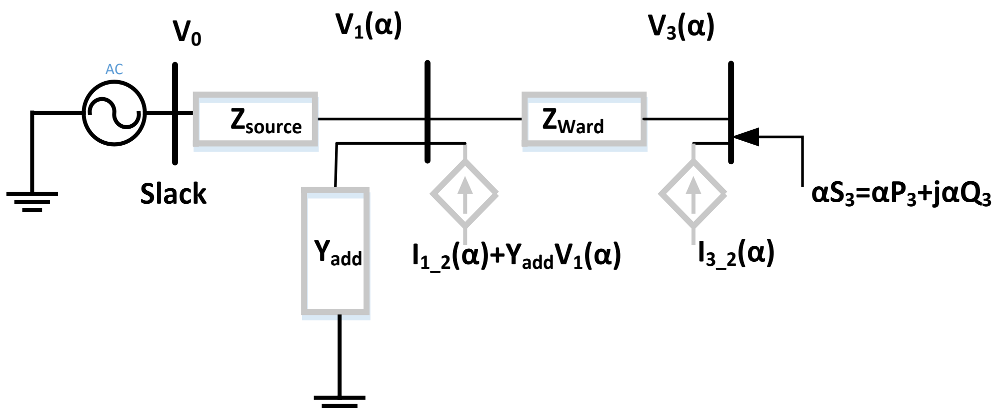

Figure 3.34 Shunt impedance and compensatory shunt current added at bus 1.

Note that since the additional shunt impedance is negated by an equivalent injected current, the bus voltages and current flows in the network are still preserved. The effective input impedance of the above network is then given by:

$$
\begin{aligned}
\hat{Z}_{series} &= Z_{source} \parallel (1/Y_{add}) + Z_{Ward} \\
&= \frac{1}{\dfrac{1}{Z_{source}} + Y_{add}} + Z_{Ward} \\
&= \frac{Z_{source}}{1 + Y_{add} Z_{source}} + Z_{Ward}
\end{aligned}
\qquad (3.24)
$$

Since the additional shunt impedance can be arbitrarily chosen, this implies that the effective source impedance $\hat{Z}_{series}$ can also be arbitrary and the nonlinear source voltage will then ensure that the load voltage and current characteristics are preserved. One can reverse engineer the above process to calculate the additional shunt impedance one needs to add on to bus 1, $Z_{add} = Y_{add}^{-1}$ given by (3.25), in order to get the desired value of effective source impedance, $Z_{desired}$.

$$
Z_{add} = \frac{Z_{source}(Z_{desired} - Z_{Ward})}{(Z_{source} + Z_{Ward} - Z_{desired})} \qquad (3.25)
$$

This was verified numerically on the four-bus and 14-bus systems where the source impedance was arbitrarily forced to be 0.01+0.1j and the necessary shunt impedance calculated from (3.27) and compensatory current was added at bus 1. The voltage series of the bus-of-interest obtained by solving the power-flow problem for this reduced-order network was the same as that from the full-network with an accuracy on the order of 10^{-14}. Thus, one can arbitrarily choose a value for the series impedance and fit the series for the source voltage using measurements such that the voltage at the bus-of-interest is preserved and such a model will preserve the system SNBP. Expectedly, if one chooses the series impedance value to be the measurement-based Z_{Th} from section 3.1, that value of $V_S(\alpha)$, evaluated at that particular loading-level, matches the measurement-based E_{Th} with an accuracy of 10^{-15}. This shows that the measurement-based Thévenin equivalent network, is obtained by linearizing one of the infinitely-many nonlinear Thévenin-like networks about the base-case operating point.

3.4.4 Maximum power-transfer condition in the presence of a variable voltage source

It is known that if the voltage source and impedance are constant, the maximum power transfer to the load occurs when the magnitude of the load impedance is equal to the magnitude of the source impedance, i.e., $|Z_{Source}|=|Z_L|$. However, the Thévenin-like network developed in section 3.4 has a voltage source that is a function of the load-scaling factor α. Hence the assumption of a constant source is no longer valid, consequently the condition $|Z_{Source}|=|Z_L|$ is no longer true at the maximum power transfer point. This is shown in Figure 3.35, in which the magnitude of the load impedance and the magnitude of the source impedance is plotted against the load-scaling factor, α. It is seen that there is a significant difference between the magnitude of the source impedance and the load impedance even at the SNBP which occurs at α = 4.012 obtained using CPF. Note that the source impedance remains constant as the system load increases, which is expected.

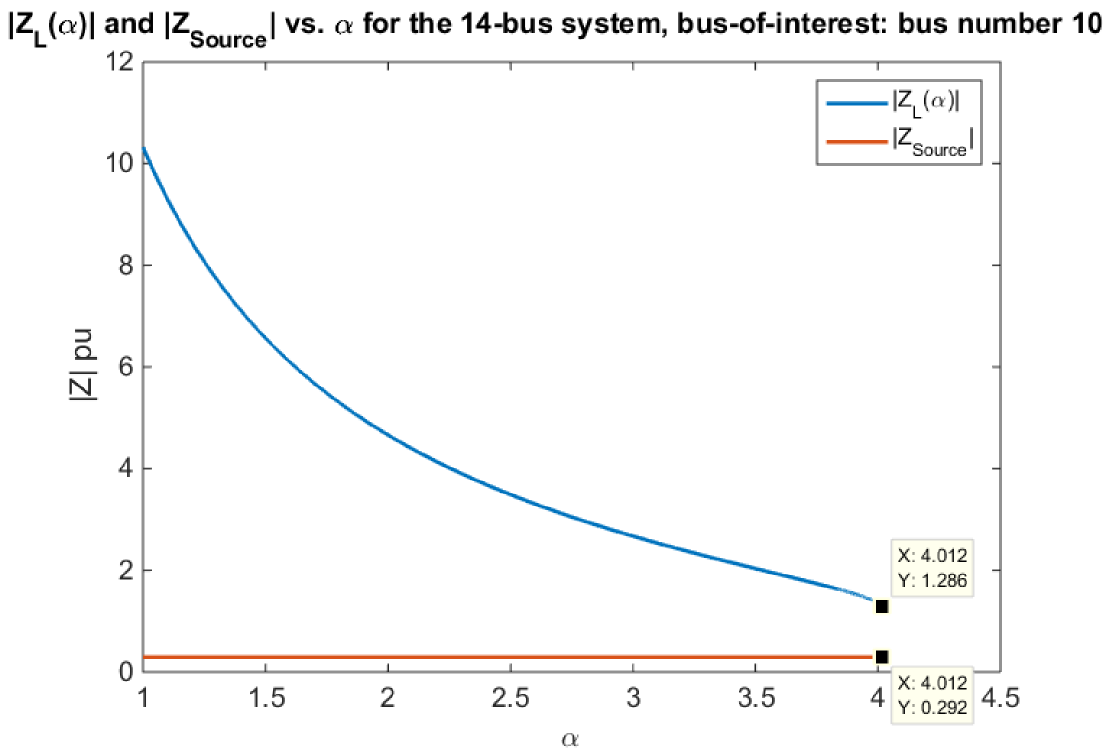

Figure 3.35 $|Z_L(\alpha)|$ and $|Z_{Source}|$ vs. α for the modified 14-bus system

Since the end goal is to use nonlinear HE-reduced networks to estimate the voltage stability margin, it is important to derive the condition at which maximum power transfer will occur. While one can use the roots (poles/zeros) of the voltage series, it is not clear as to which method would work the best when building the networks using actual noisy measurements. Hence it is important to have alternatives such as the maximum power transfer theorem for nonlinear networks. Using the same approach as that used for linear networks, i.e., equating to zero the derivative of the real-power transferred to the load w.r.t. to the load resistance, the appropriate condition can be derived as described below.

The power delivered to the load in the Thévenin-like network shown in Figure 3.23, is given by (3.26) which is similar to (3.9), with the only difference being that E_{Th} is replaced by $V_S(\alpha)$ which is the nonlinear voltage source in the Thévenin-like network and R_{Th} ,X_{Th} are replaced by R_S, X_S which are the resistive and reactive components of the net series impedance.

$$P_L = \frac{|V_S(\alpha)|^2 R_L(\alpha)}{\left(R_S + R_L(\alpha)\right)^2 + \left(X_S + X_L(\alpha)\right)^2} \tag{3.26}$$

Assuming that the power factor angle of the load, Φ, is kept fixed, the load impedance can be written as:

$$Z_L(\alpha) = R_L(\alpha) + jX_L(\alpha) = R_L(\alpha) + jR_L(\alpha)\tan(\phi) \tag{3.27}$$

Equation (3.26) can thus be written as:

$$P_L = \frac{|V_S(\alpha)|^2 R_L(\alpha)}{\left(R_S + R_L(\alpha)\right)^2 + \left(X_S + R_L(\alpha)\tan(\phi)\right)^2} \tag{3.28}$$

The derivative of P_L with respect to R_L is given by:

$$\begin{aligned}
&\frac{\partial P_L}{\partial R_L(\alpha)} = \\
&\frac{\left\{\dfrac{\partial |V_S(\alpha)|^2}{\partial R_L(\alpha)} R_L(\alpha) + |V_S(\alpha)|^2\right\}\left\{\left(R_S + R_L(\alpha)\right)^2 + \left(X_S + R_L(\alpha)\tan(\phi)\right)^2\right\}}{\left(\left(R_S + R_L(\alpha)\right)^2 + \left(X_S + R_L(\alpha)\tan(\phi)\right)^2\right)^2} \\
&-\frac{|V_S(\alpha)|^2 R_L(\alpha)\left\{2\left(R_S + R_L(\alpha)\right) + 2\left(X_S + R_L(\alpha)\tan(\phi)\right)\tan(\phi)\right\}}{\left(\left(R_S + R_L(\alpha)\right)^2 + \left(X_S + R_L(\alpha)\tan(\phi)\right)^2\right)^2}
\end{aligned} \tag{3.29}$$

When the power delivered to the load is maximum, the derivative of P_L with respect to R_L is zero. Equating (3.29) to zero, we get:

$$\begin{aligned}
&\left\{\frac{\partial |V_S(\alpha)|^2}{\partial R_L(\alpha)} R_L(\alpha) + |V_S(\alpha)|^2\right\}\left\{\left(R_S + R_L(\alpha)\right)^2 + \left(X_S + R_L(\alpha)\tan(\phi)\right)^2\right\} = \\
&|V_S(\alpha)|^2 R_L(\alpha)\left\{2\left(R_S + R_L(\alpha)\right) + 2\left(X_S + R_L(\alpha)\tan(\phi)\right)\tan(\phi)\right\}
\end{aligned} \tag{3.30}$$

Equation (3.30) can be rearranged as follows:

$$\begin{aligned}
&\left\{\frac{\partial |V_S(\alpha)|^2}{\partial R_L(\alpha)} R_L(\alpha)\right\}\left\{\left|Z_S + Z_L(\alpha)\right|^2\right\} = \\
&|V_S(\alpha)|^2 R_L(\alpha)\left\{2\left(R_S + R_L(\alpha)\right) + 2\left(X_S + R_L(\alpha)\tan(\phi)\right)\tan(\phi)\right\} \\
&-|V_S(\alpha)|^2\left\{\left(R_S + R_L(\alpha)\right)^2 + \left(X_S + R_L(\alpha)\tan(\phi)\right)^2\right\}
\end{aligned} \tag{3.31}$$

The terms of the right-hand side expression can be expanded to obtain:

$$\begin{aligned}
&\left\{\frac{\partial |V_S(\alpha)|^2}{\partial R_L(\alpha)} R_L(\alpha)\right\}\left\{\left|Z_S + Z_L(\alpha)\right|^2\right\} = \\
&|V_S(\alpha)|^2\left\{\begin{array}{l} 2R_S R_L(\alpha) + 2R_L^2(\alpha) + 2X_S R_L(\alpha)\tan(\phi) + 2R_L^2(\alpha)\tan^2(\phi) \\ -\left\{\begin{array}{l} R_S^2 + R_L^2(\alpha) + 2R_S R_L(\alpha) + X_S^2 \\ + R_L^2(\alpha)\tan^2(\phi) + 2X_S R_L(\alpha)\tan(\phi) \end{array}\right\} \end{array}\right\}
\end{aligned} \tag{3.32}$$

Equation (3.32) is reduced to:

$$\left\{\frac{\partial\left|V_S(\alpha)\right|^2}{\partial R_L(\alpha)}R_L(\alpha)\right\}\left\{\left|Z_S+Z_L(\alpha)\right|^2\right\}$$
$$=\left|V_S(\alpha)\right|^2\left\{R_L^2(\alpha)+R_L^2(\alpha)\tan^2(\phi)-R_S^2-X_S^2\right\} \tag{3.33}$$

Equation (3.33) can then be reduced to obtain the final maximum power transfer condition given by (3.34) or, the theoretical equivalent in (3.35), when the source voltage is not constant.

$$\left\{\frac{\partial\left|V_S(\alpha)\right|^2}{\partial R_L(\alpha)}R_L(\alpha)\right\}\left\{\left|Z_S+Z_L(\alpha)\right|^2\right\}$$
$$=\left|V_S(\alpha)\right|^2\left\{\left|Z_L(\alpha)\right|^2-\left|Z_S\right|^2\right\} \tag{3.34}$$

$$\frac{\partial\left|V_S(\alpha)\right|^2}{\partial R_L(\alpha)}\frac{R_L(\alpha)}{\left|V_S(\alpha)\right|^2}=\frac{\left|Z_L(\alpha)\right|^2-\left|Z_S\right|^2}{\left|Z_S+Z_L(\alpha)\right|^2} \tag{3.35}$$

The Maclaurin series for the expression $\partial|V_S(\alpha)|^2/\partial R_L(\alpha)$ used in (3.34) is obtained as:

$$\frac{\partial\left|V_S(\alpha)\right|^2}{\partial R_L(\alpha)}=\frac{\dfrac{\partial\left|V_S(\alpha)\right|^2}{\partial\alpha}}{\dfrac{\partial R_L(\alpha)}{\partial\alpha}} \tag{3.36}$$

The Maclaurin series for $|V_S(\alpha)|^2$ can be obtained as:

$$\left|V_S(\alpha)\right|^2=V_S(\alpha)\cdot V_S^*(\alpha^*) \tag{3.37}$$

and then the derivative of $|V_S(\alpha)|^2$ with respect to α can be calculated. For load buses with PQ loads, the load impedance $Z_L(\alpha)$ is given by:

$$Z_L(\alpha)=\frac{V(\alpha)V^*(\alpha^*)}{\alpha S^*} \tag{3.38}$$

Note that if the expression for $Z_L(\alpha)$ on the RHS of (3.38) is expanded as a power series, one will get a term with a negative exponent of α. Hence the expression for $R_L(\alpha)$ will also have a term with a negative exponent of α. In order to avoid the negative exponent, the values of the load resistance at different values of α can be obtained using the value of $\alpha R_L(\alpha)$, for which the Maclaurin series is given by (3.39),

$$\alpha R_L(\alpha) = \mathrm{Re}\left(\frac{V(\alpha)V^*(\alpha^*)}{S^*}\right) \tag{3.39}$$

where the function Re(.) indicates the real part of the operand. The value of $\partial R_L(\alpha)/\partial\alpha$ at different values of α can be obtained using the value of $\partial\alpha R_L(\alpha)/\partial\alpha$ as shown below:

$$\begin{aligned} \frac{\partial\alpha R_L(\alpha)}{\partial\alpha} &= \alpha\frac{\partial R_L(\alpha)}{\partial\alpha} + R_L(\alpha) \\ \therefore \frac{\partial R_L(\alpha)}{\partial\alpha} &= \frac{\left(\dfrac{\partial\alpha R_L(\alpha)}{\partial\alpha} - R_L(\alpha)\right)}{\alpha} \end{aligned} \tag{3.40}$$

It is seen that the left-hand-side (LHS) and right-hand-side expressions (RHS) of (3.34) are purely real. However, the $\partial|V_S(\alpha)|^2/\partial R_L(\alpha)$ term on the LHS is obtained by first performing convolutions of complex-valued power series and then taking derivatives with respect to α. While theoretically the series should be purely real, performing a convolution of two complex-valued power series, leads to small imaginary parts in the resultant series with magnitudes less than 10^{-19}. At loading levels that are not very close to the SNBP, the imaginary part of the LHS of (3.34) is observed to be of the order of 10^{-15}. However when the system load is modeled to be within 1% of the SNBP, the numerically small imaginary parts in the different series involved in the LHS of (3.34) become significant since they are multiplied by high-order exponents of α, which causes the imaginary part of the Padé approximants of the series on the LHS to be of the order of 10^{-3}. This is shown in Figure 3.36 and Figure 3.37 in which the imaginary parts of the LHS and RHS of (3.34) are plotted against α for the four-bus system and the modified 14-bus system (when bus 9 is retained), respectively. Since the imaginary parts of the LHS and RHS should theoretically be zero and are numerically of the order of 10^{-15} unless the system load is modeled to be within 1-2% of the SNBP, the imaginary parts will be ignored in the rest of the discussion.

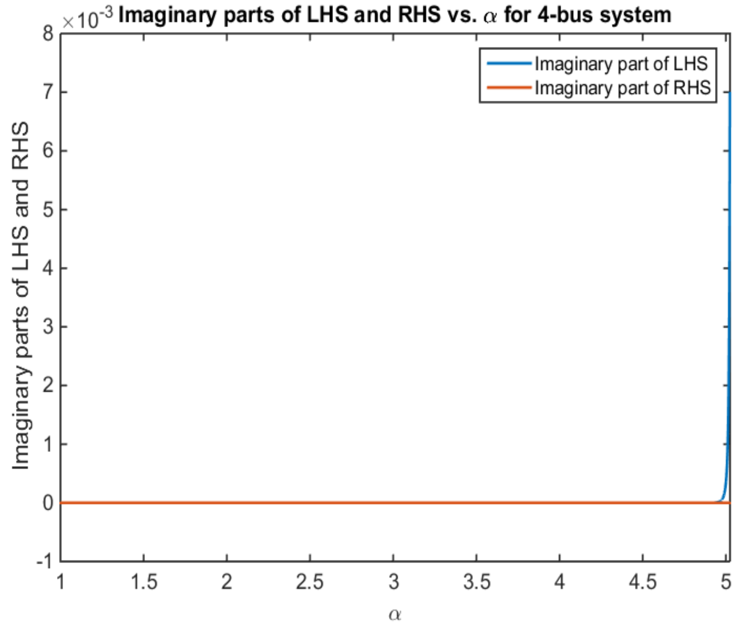

Figure 3.36 Imaginary parts of the LHS and RHS of (3.34) vs. α for the four-bus system

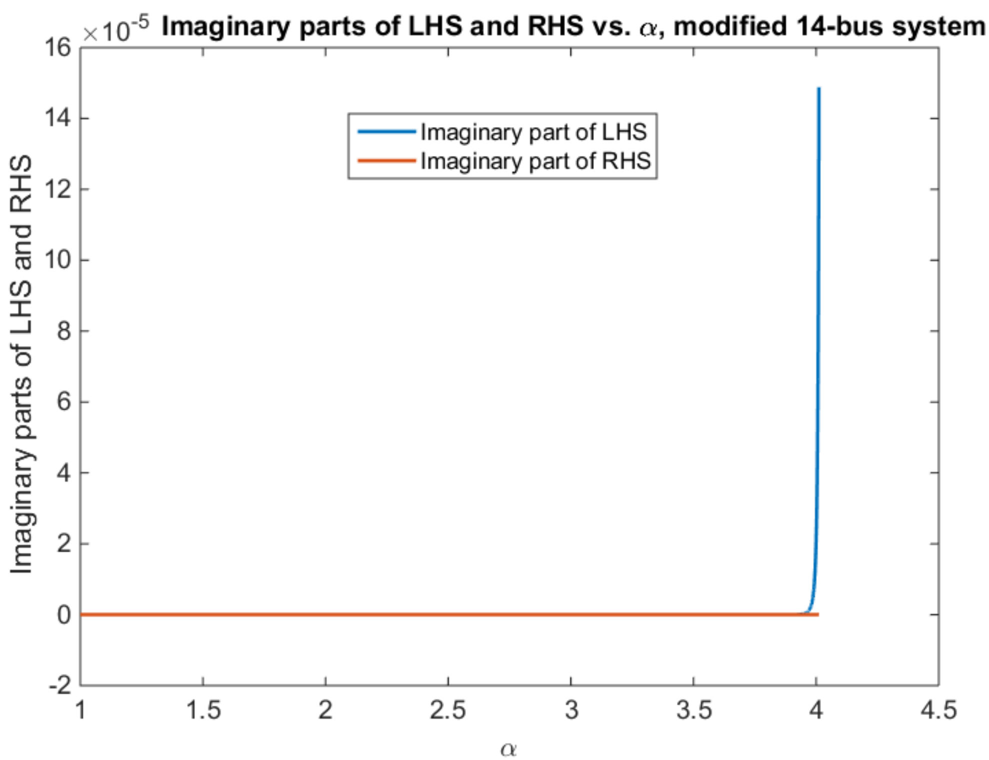

Figure 3.37 Imaginary parts of the LHS and RHS of (3.34) vs. α for the modified 14-bus system

The validity of the condition given by (3.34) is verified using the four-bus system shown in Figure 3.18 and the modified 14-bus system. In Figure 3.38 the LHS and RHS for the four-bus system are plotted against the load-scaling factor varying up to the SNBP and it is seen that at the SNBP, the LHS and RHS are very close to each other. Similarly, the LHS and RHS are plotted in Figure 3.39 against α for the modified 14-bus system (with the bus-of-interest chosen to be bus number 4) and the two approach each other at the SNBP as expected. It is observed that when the system load is modeled to be within 0.1% of the SNBP, a cross-over occurs between the values of the LHS and RHS expressions, which can be attributed to precision issues and is left as future work. It is well-known that precision limitations become an issue for the HEPF-based methods when the system is modeled to be very close to the SNBP.

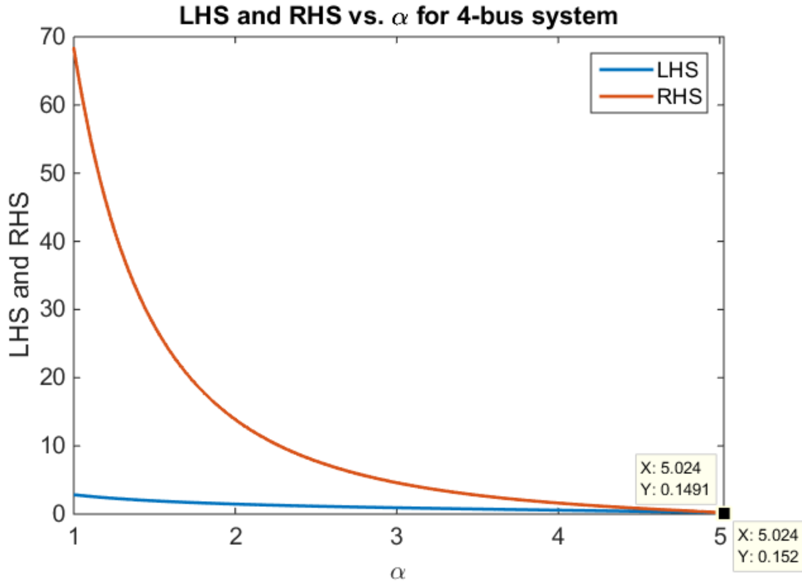

Figure 3.38 LHS vs. RHS of (3.34) for the four-bus system

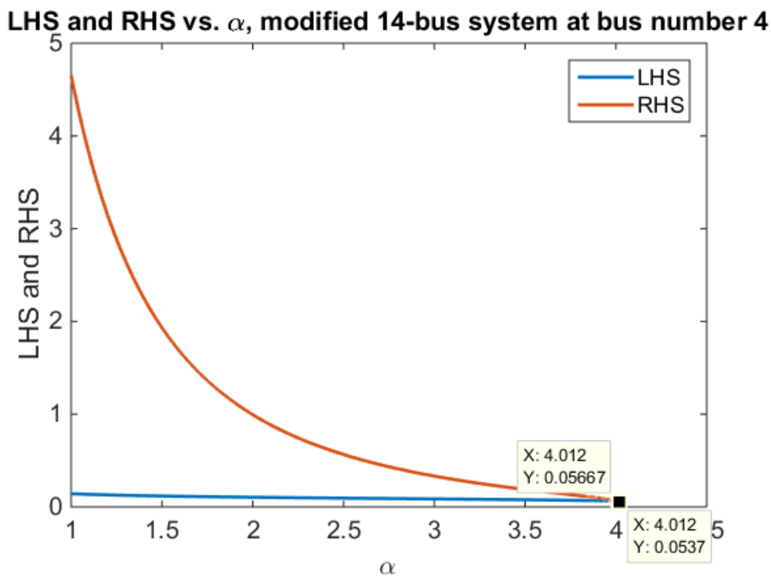

Figure 3.39 LHS vs. RHS of (3.34) for the modified 14-bus system

The condition also holds true for a Thévenin-like network with an arbitrarily chosen impedance as explained in section 3.4.3. This was verified numerically on the modified 14-bus system with the source impedance forced to be 0.15j (while the series impedance obtained using traditional HE reduction was approximately 0.03 + 0.1j). The necessary additional shunt impedance was calculated using (3.27) with compensatory current added at bus number 1. This is shown in Figure 3.40 where the LHS and RHS are plotted against α (varying up to the SNBP) for the above described arbitrarily chosen Thévenin-like network, with the bus-of-interest being bus number 4.

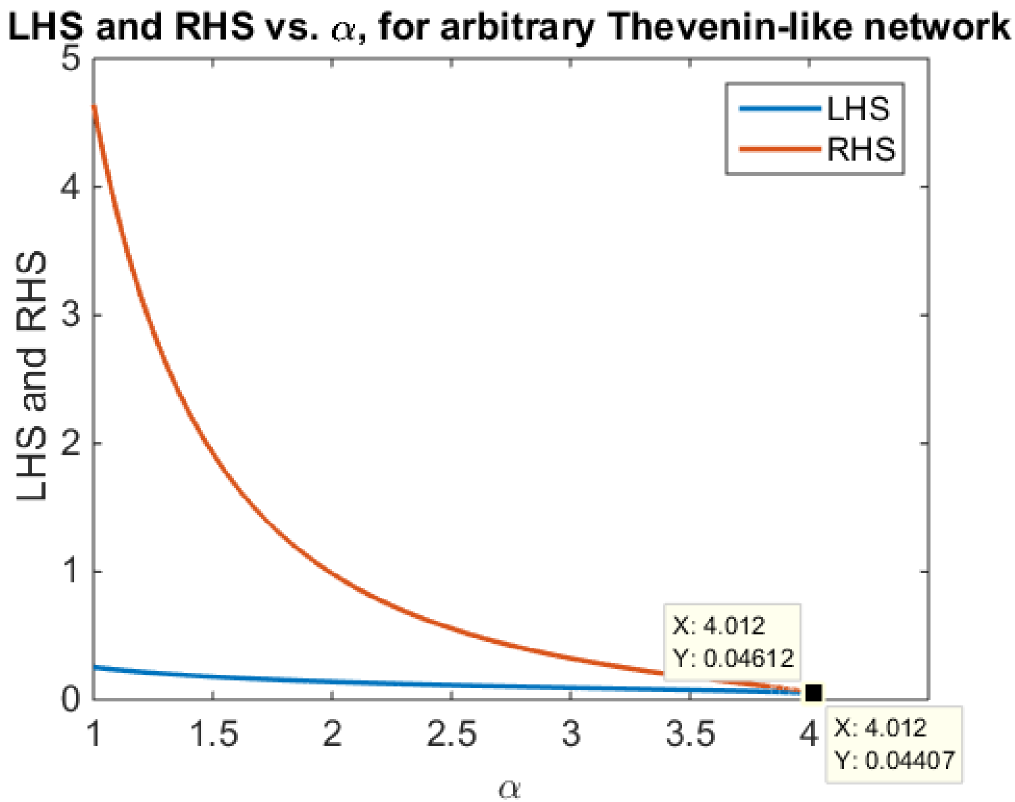

Figure 3.40 LHS vs. RHS of (3.34) for the modified 14-bus system with an arbitrary Thévenin-like network

3.4.5 Some implementation details

3.4.5.1 Handling ZIP-load models and arbitrary load models

While so far in this section only constant PQ loads were considered, the actual load may have ZIP-load characteristics or other more complex characteristics which need to be accounted for appropriately. The model for solving a power-flow problem in the presence of ZIP-loads requires representing all loads nonlinear current injections of α. The development is straight forward and will not be included here. Thus the reduction process to obtain the Thévenin-like networks would be the same as described in section 3.4.1. The maximum power transfer condition for nonlinear networks given by (3.34) holds true in the presence of ZIP-load models as well. While evaluating the two sides of the condition, one would need to calculate the effective load impedance $Z_L(\alpha)$ given by:

$$Z_L(\alpha) = \frac{V_i(\alpha)V_i^*(\alpha^*)}{\alpha P_{li}\left(p_1|V_i|^2(\alpha)+p_2|V_i|(\alpha)+p_3\right)-j\alpha Q_{li}\left(q_1|V_i|^2(\alpha)+q_2|V_i|(\alpha)+q_3\right)}, \quad i\in m \tag{3.41}$$

The LHS and RHS of (3.34) are plotted against α in Figure 3.41, for the 14-bus system with ZIP loads (equal proportions of the constant impedance, constant current and constant power assumed), with the bus-of-interest being bus number 2. The load-scaling factor is varied through to the SNBP in Figure 3.41 and it is seen that the LHS and RHS are numerically close to each other at the SNBP.

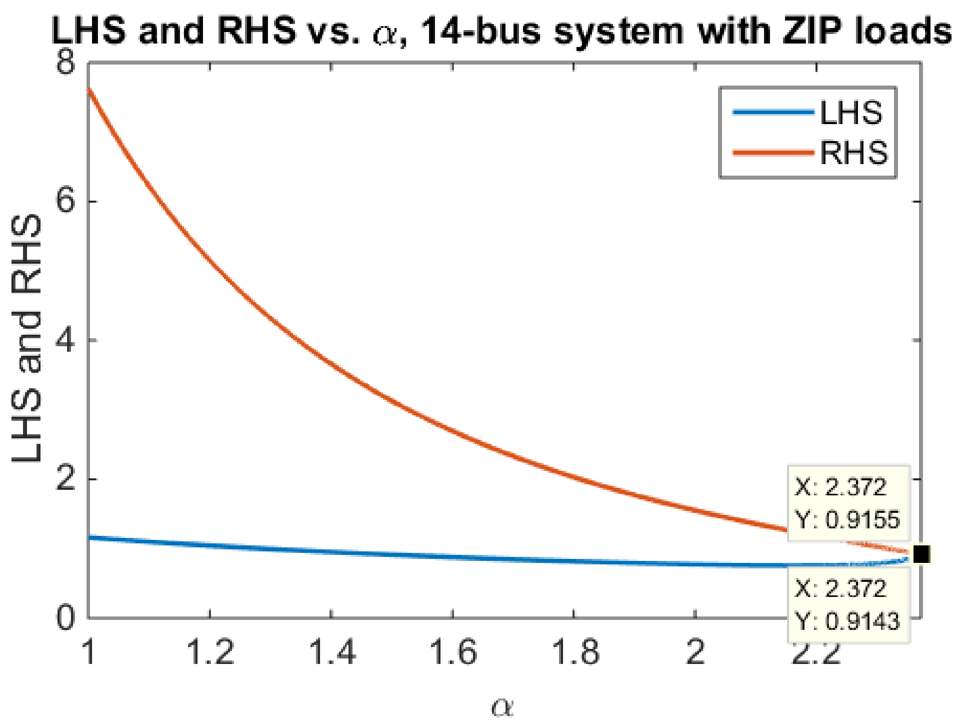

Figure 3.41 LHS and RHS of (3.34) for the modified 14-bus system with ZIP loads

In fact, any arbitrary load can effectively be represented as a nonlinear current injection in order to get the Thévenin-like networks. This can be demonstrated using an arbitrary load model that looks like:

$$\begin{aligned} S_L(\alpha) &= \alpha P_{li}\left(p_1|V_i|^2(\alpha)+p_2|V_i|(\alpha)+p_3\right)+j\alpha Q_{li}\left(q_1|V_i|^2(\alpha)+q_2|V_i|(\alpha)+q_3\right) \\ &+ K_i\left(\alpha+\frac{\alpha^3}{3!}+\frac{\alpha^5}{5!}+\frac{\alpha^7}{7!}+\frac{\alpha^9}{9!}+\frac{\alpha^{11}}{11!}\right) i\in m \end{aligned} \tag{3.42}$$

The above load model looks like a ZIP-load model along with a sine-of-α-series accurate to 11 Maclaurin series terms. Such a load model was added at each bus in the 14-bus system with the coefficient K_i being randomly chosen from uniformly distributed numbers between 0 and 10 MW (the base-case real-power loads at the different buses vary between 3.5 MW and 94.2 MW for this system). With this load modeled as a nonlinear current injection, the HEPF was used to solve the power-flow problem and then HE-reduction was performed. It was observed that as long as the reduction rules provided in this work are followed, the series terms of the voltage series (truncated at 61 terms) at the retained bus were preserved, when compared to the full network voltage series terms, with an accuracy of the order of 10^{-14} and the SNBP of the system was also preserved.

3.4.5.2 Handling transformers

3.4.5.2.1 Handling transformers with off-nominal tap ratios

Transformers with off-nominal tap ratios, are effectively modeled using pi models and hence shunt impedances are added at the terminal buses. As explained in section 3.4.3, fixed shunt impedances can either be represented in the admittance matrix, which would result in shunt impedances appearing in the HE-reduced network; or they may be modeled as nonlinear current injections given by $-Y_{shunt}V(\alpha)$ which would result in a reduced-order network that doesn't have any shunt impedances. Eventually, whether shunt impedances are retained in the HE-reduced network or converted to nonlinear current injections, the full model will be reduced to a Thévenin-like network shown in Figure 3.23 if the network reduction procedure given here is followed.

3.4.5.2.2 Handling transformers with non-zero phase-shifts

Transformers with non-zero phase-shifts lead to an asymmetric admittance matrix. If the phase-shifts are represented in the admittance matrix before performing HE-reduction, the reduced order network will have an effective phase-shifting transformer (i.e. the admittance matrix for the reduced network will also be asymmetric). It was shown in [31] that in order to obtain a power-flow solution using a non-scalable formulation in the presence of phase-shifting transformers, the asymmetric part of the admittance matrix needs to be moved to the right-hand side of the node-balance equation as an equivalent current injection. Phase-shifting transformers have not been accounted for in the previously published work on network reduction [27] as it is not straightforward to segregate the asymmetric components from the symmetric components using only the reduced-network admittance matrix for meshed reduced-order systems. Phase-shifting transformers can be handled in a similar manner as shunts in the system, i.e., the asymmetric components of the full-network admittance matrix that are present due to the phase-shifting transformers, can be modeled as nonlinear current injections before performing the HE-reduction and thus removed from the admittance matrix. This would result in a simpler reduced-order network without any phase-shifting transformer, that is structurally similar to Figure 3.23. This was numerically tested on the modified 14-bus system, by adding non-zero phase shifts to the three transformers in the system (with the phase-shifts chosen to be 7°, 9° and 25°). It was observed that the voltages were preserved as well as the condition given by (3.34) was obeyed at the SNBP as shown in Figure 3.42 where the LHS and RHS of (3.34) are plotted against α with the α being varied from 1.0 (i.e., the base-case loading condition) through to the SNBP, with the bus-of-interest being bus number 4.

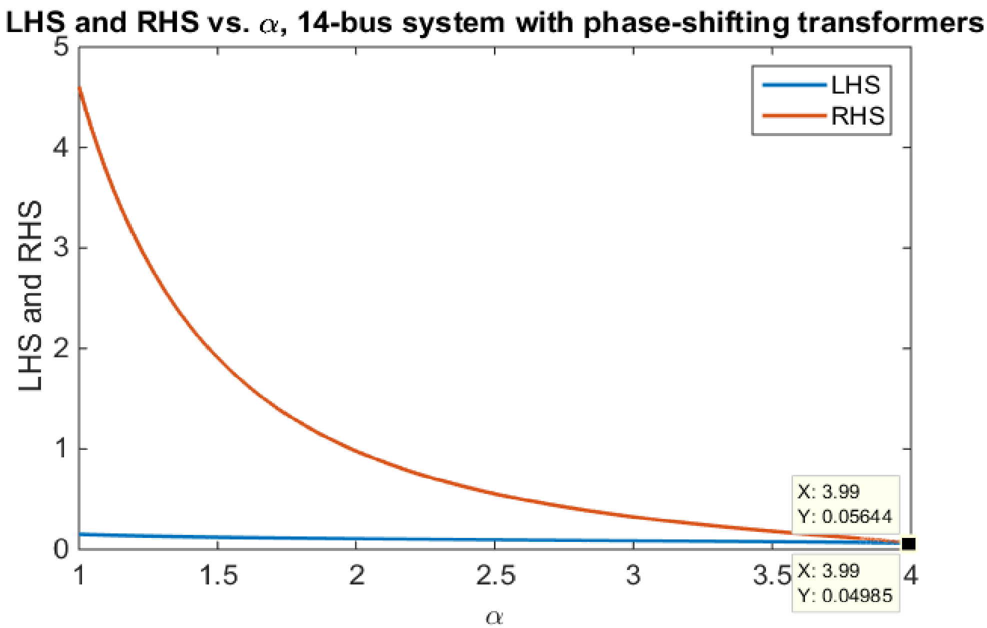

Figure 3.42 LHS and RHS of (3.34) for the modified 14-bus system with phase-shifting transformers

3.4.6 Multi-bus reduced-order equivalent networks

As mentioned in section 3.1, multi-bus equivalent networks have been used to estimate the voltage stability margin using the measurements in a load area in order to better account for the different limits of individual tie-lines connecting the load area to the rest of the network [24], [38], [43] - [45]. Hence it may be desirable to develop multi-bus nonlinear equivalent networks as well. It has already been shown that HE-reduction can be used to obtain multi-bus reduced-order equivalent networks which preserve the nonlinear behavior of the original system when there are no phase-shifting transformers in the system [27]. Using the strategy described in section 3.4.5.2 for modeling phase-shifters, multi-bus reduced networks can also developed for systems with phase-shifting transformers such that the voltages at the retained buses are preserved. This is shown in Figure 3.43, in which the magnitude of worst error (taken over all retained buses) between the bus voltages of the full network and those of the reduced network is plotted on a log scale against α for the 14-bus system with three phase-shifting transformers, when buses 0, 1, and 9 through 11 are preserved in the reduced network.

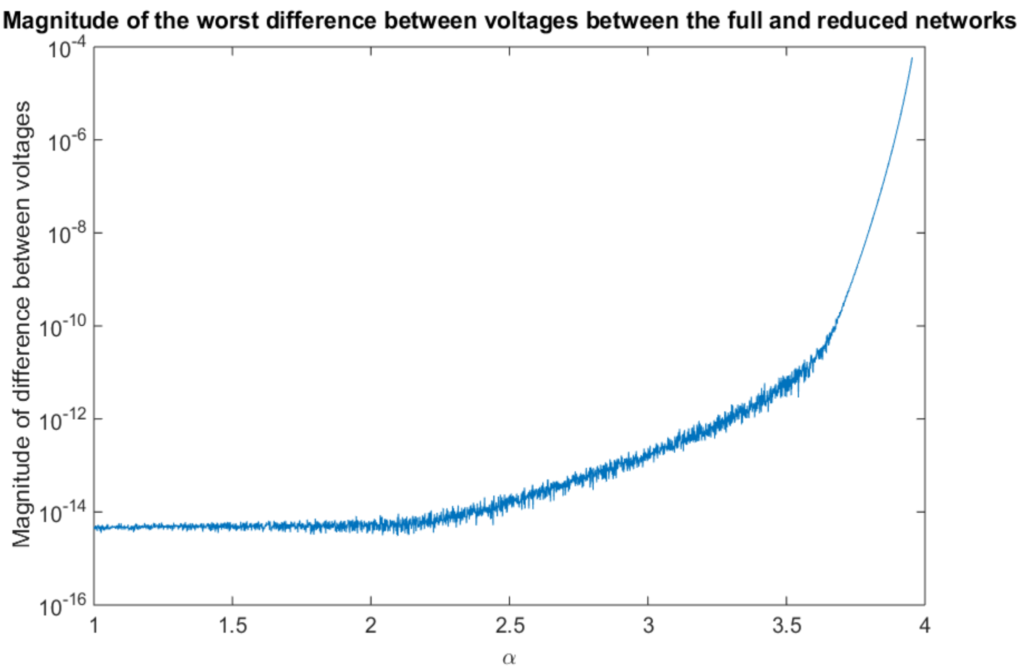

Figure 3.43 Error between the voltages of the full system and a multi-bus reduced-order system for the 14-bus system with phase-shifting transformers

As pointed out in section 3.4.3, there are an infinite number of ways of developing such reduced-order networks. Consider a reduced-order network obtained using HE-reduction with the admittance matrix $Y_{Reduced}$ given by (3.43), where the subscripts b and i denote the boundary (i.e. buses that are connected to the buses that have been eliminated), and internal buses respectively.

$$Y_{\mathrm{Re}\,duced} = \begin{bmatrix} Y_{bb} \; Y_{bi} \\ Y_{ib} \; Y_{ii} \end{bmatrix} \tag{3.43}$$

The node-balance equations in the reduced network are given by (3.44) where the subscripts e denotes external buses (i.e., buses in the full model that are not a part of the reduced network). As seen from (3.44) the boundary buses have additional current injections given by $I'_e(\alpha)$ that account for the injections and losses in the external network (i.e., in addition to the native loads at these buses).

$$\begin{bmatrix} Y_{bb} \; Y_{bi} \\ Y_{ib} \; Y_{ii} \end{bmatrix} \begin{bmatrix} V_b(\alpha) \\ V_i(\alpha) \end{bmatrix} = \begin{bmatrix} I_e^{'}(\alpha) + \alpha S_b^* W_b^*(\alpha^*) \\ \alpha S_i^* W_i^*(\alpha^*) \end{bmatrix} \tag{3.44}$$

Note just as there is much flexibility in selecting the value of the series impedance branch for a two-bus equivalent, there is similar flexibility for a multi-bus equivalent. One can modify the admittance matrix (and hence the series impedances) of the reduced network by adding compensatory nonlinear current injections on the RHS of (3.44) as shown below:

$$\begin{bmatrix} Y_{bb} & Y_{bi} \\ Y_{ib} & Y_{ii} \end{bmatrix}\begin{bmatrix} V_b(\alpha) \\ V_i(\alpha) \end{bmatrix} + \begin{bmatrix} Y_{bb}^{'} - Y_{bb} & Y_{bi}^{'} - Y_{bi} \\ Y_{ib}^{'} - Y_{ib} & Y_{ii}^{'} - Y_{ii} \end{bmatrix}\begin{bmatrix} V_b(\alpha) \\ V_i(\alpha) \end{bmatrix}$$
$$= \begin{bmatrix} I_e^{'}(\alpha) + \alpha S_b^* W_b^*(\alpha^*) \\ \alpha S_i^* W_i^*(\alpha^*) \end{bmatrix} + \begin{bmatrix} Y_{bb}^{'} - Y_{bb} & Y_{bi}^{'} - Y_{bi} \\ Y_{ib}^{'} - Y_{ib} & Y_{ii}^{'} - Y_{ii} \end{bmatrix}\begin{bmatrix} V_b(\alpha) \\ V_i(\alpha) \end{bmatrix} \tag{3.45}$$

Thus the modified admittance matrix of the reduced network is given by (3.46) and the modified current injections are given by (3.47).

$$\hat{Y}_{\mathrm{Re}duced} = \begin{bmatrix} Y_{bb}^{'} & Y_{bi}^{'} \\ Y_{ib}^{'} & Y_{ii}^{'} \end{bmatrix} \tag{3.46}$$

$$\hat{I}_{\mathrm{Re}duced} = \begin{bmatrix} I_e^{'}(\alpha) + \alpha S_b^* W_b^*(\alpha^*) \\ \alpha S_i^* W_i^*(\alpha^*) \end{bmatrix} + \begin{bmatrix} Y_{bb}^{'} - Y_{bb} & Y_{bi}^{'} - Y_{bi} \\ Y_{ib}^{'} - Y_{ib} & Y_{ii}^{'} - Y_{ii} \end{bmatrix}\begin{bmatrix} V_b(\alpha) \\ V_i(\alpha) \end{bmatrix} \tag{3.47}$$

In fact, not only can the impedance values in the HE-reduced network be modified using (3.45), but the topology can also be changed, though we believe in most cases it is unwise to do so. One could add additional branches that did not exist in the HE-reduced network. For example, for the 14-bus system with three phase-shifting transformers, when buses 0, 1, 9 through 11 are preserved in the reduced network, there is no connection between bus number 1 and bus number 10. However, a branch with impedance 0.01+0.1j was added between these two buses and compensatory currents added at buses 1 and 10 using (3.45). When the power-flow problem for such a reduced network was solved, it was observed that each term of the truncated Maclaurin voltage series (up to 61 terms) at all the retained buses in the new reduced network, matched those from the full network, with an accuracy of the order of 10^{-14}. Similarly, one could remove an existing branch by setting $Y^{'}_{ik}$ to be zero. For the 14-bus system reduction example described above, two branches were removed to effectively obtain a radial reduced-order network, while still preserving each term of the truncated voltage series (up to 61 terms) at the retained buses with an accuracy of the order of 10^{-14} when compared to the voltage series for the full model.

The implication that this has on using measurements to build multi-bus equivalent networks is that, one does not need to know the appropriate topology and network parameters prior to building the network, though it is believed results would be best if the topology chosen matches that in the real world. One can assume a certain topology and network parameters for the reduced network and fit the Maclaurin series for the nonlinear current injections using measurements at the retained buses. Note that the multi-bus reduced order networks, require more polynomials to be fitted than the Thévenin-like equivalent networks since each bus has a nonlinear current injection.

3.5 Revisiting the sigma method

It was shown in [51] that the original sigma method as shown in [33], has some fundamental flaws. It was shown that while it is true that to ensure a valid operating point for any system, the sigma condition must be obeyed for all of the system buses, the proximity of the σ condition to violating its limit at any of the buses is not an indicator of the proximity of the system to voltage collapse. This occurs because the σ indices of some of the buses can come very close to the boundary condition at loading levels far below the SNBP, and then start moving away from the boundary with further load increase. The fundamental issue is that, while the distance of the σ condition from its limit is an indicator of the proximity of the system to voltage collapse for a *two-bus system*, it is not an indicator for a two-bus *equivalent* of a larger system. The voltage source in the two-bus equivalent from which the original σ indices are obtained is constant (slack-bus voltage) whereas it has been shown in section 3.4 that a proper equivalent obtained using network-reduction procedures where the loads are modeled as nonlinear current injections would have a voltage source that depends on the loading condition. It will be shown numerically that if the σ indices are calculated corresponding to the Thévenin-like network obtained in section 3.4, these revised σ indices do not face the same issues as the original σ indices. The $U(\alpha)$ for the Thévenin-like network as shown in [51] is given by:

$$U(\alpha)=\frac{V(\alpha)}{V_{source}(\alpha)} \tag{3.48}$$

Substituting the above expression for $U(\alpha)$ into the performance equation for the two bus equivalent as shown in [51], one gets the revised σ indices, with the only difference being that $U(\alpha)$ is no longer $V(\alpha)/V_{Slack}$ but is given by (3.48). For the four-bus system from Figure 3.18, the σ condition at buses 3 and 4, evaluated using the original and revised σ indices are plotted against the load-scaling factor α in Figure 3.44. It is seen that the use of the original σ indices causes the σ condition at bus 4 be very close to zero at $\alpha = 4.85$ and then bounce back, whereas the σ condition at both buses evaluated using the revised σ indices have a consistent decreasing behavior as α increases. The other claim made in [33] was that the buses that are closer to violating the σ condition can be deemed to be the "weak buses" in the system. As discussed in [51], theoretically there is no clear connection between the sigma method of determining weak buses and the modal analysis method of determining weak buses. Using modal analysis [35], the weak bus for this small system is consistently obtained to be bus number 4 at different loading conditions (nearly 20%, 40%, 60%, 80% and 100% of the SNBP loading). However, it is seen that the "weak" bus obtained using the revised σ condition is not consistent at all loading conditions, shown by the cross-over in Figure 3.44. It is seen from Figure 3.44 that even when using the *revised* σ indices, at most operating conditions the "weak" bus obtained using the σ condition does not match that obtained using modal analysis, despite the small size and radial nature of the system being tested.

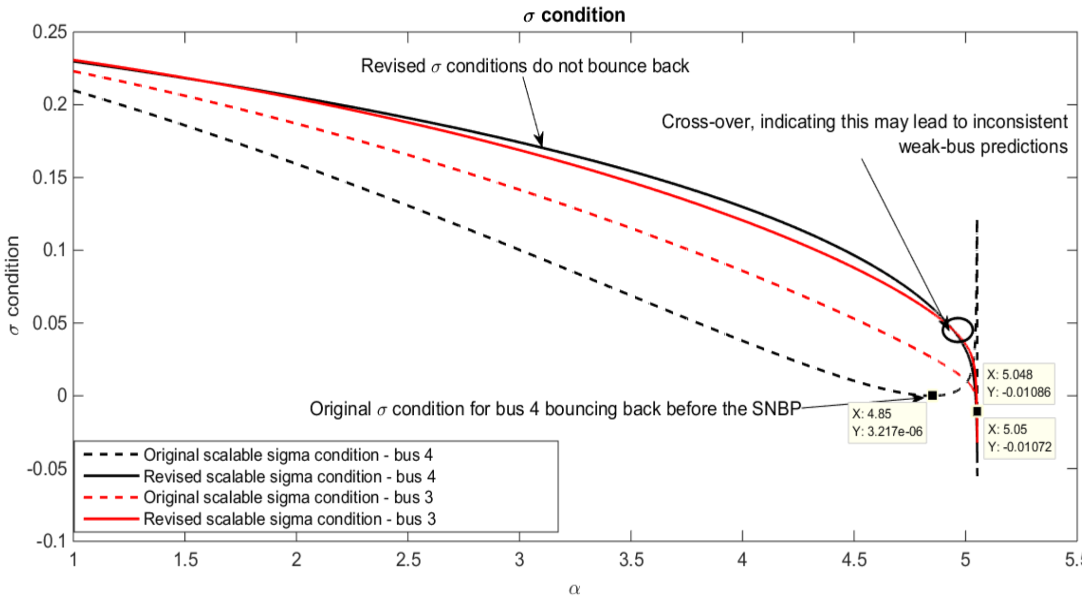

Figure 3.44 Original and revised σ conditions vs. α for the four-bus system

The σ scatter plot for bus number 4 as the system load increases is shown in Figure 3.45. The “turn-around” of the original σ index in Figure 3.45 occurs at $\alpha = 4.85$, which is consistent with its “turn-around” point observed on the σ condition plot in Figure 3.44.

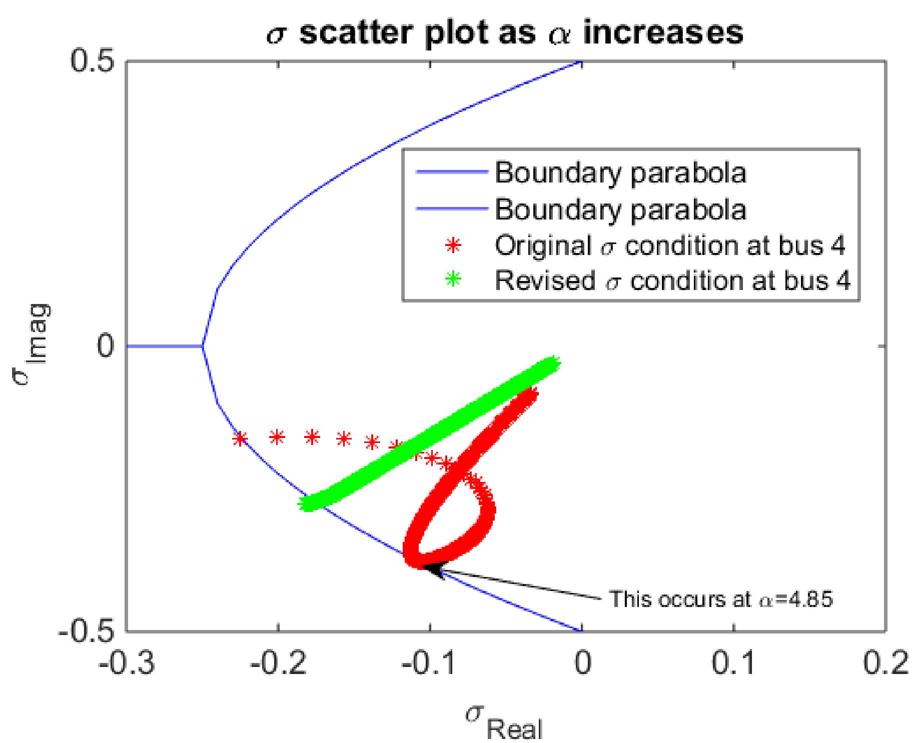

Figure 3.45 σ scatter plot with original and revised σ indices, bus 4

The σ condition with the revised σ indices was observed to have consistent behavior with load increase for the modified 14-bus system as well, as opposed to the σ condition with the original σ indices. This is shown in Figure 3.46 and Figure 3.47 where the value of the σ condition for the PQ buses is plotted against α for the revised and original σ indices respectively. Note that bus 7 has no load on it and hence the $V_{source}(\alpha)$ is the same as $V(\alpha)$ which causes the $U(\alpha)$ to be a constant (1.0) and hence the σ condition for bus 7 using the revised σ index remains constant as seen from Figure 3.46.

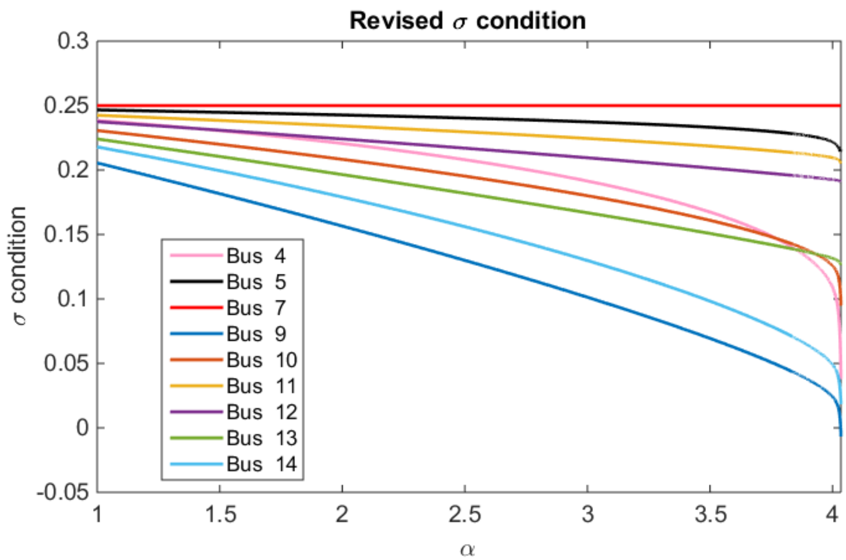

Figure 3.46 σ condition vs. α with revised σ indices, modified 14-bus system

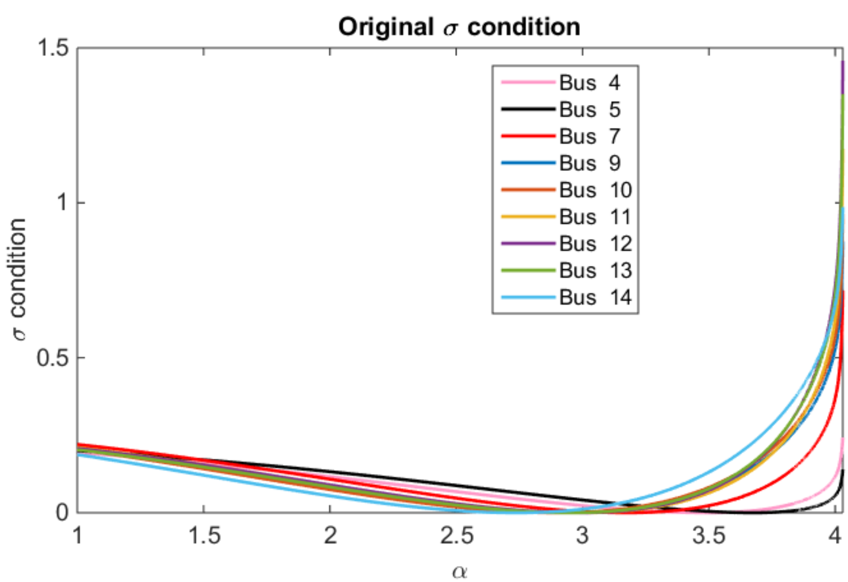

Figure 3.47 σ condition vs. α with original σ indices, modified 14-bus system

While the revised σ indices resolve the issue of approaching the boundary condition well ahead of the SNBP and then increasing again, it is seen from Figure 3.46 that for some of the buses, the σ

condition has a somewhat flat profile as the system load increased and then a sharp decrease as the modeled load gets very close to the SNBP. This highly nonlinear behavior of the σ condition, makes it unfavorable to use the σ condition as a measure of the proximity to the SNBP, even with the revised σ indices. Additionally, even for the revised σ indices, no correlation was found between the "weak buses" obtained using the σ condition and the "weak buses" from modal analysis, for the modified 14-bus system.

3.6 Conclusions

In this chapter, the measurement-based method of building a Thévenin equivalent at the bus-of-interest is discussed along with the impact that discrete changes can have on such purely local-measurement-based methods of estimating the SNBP. HE-reduction was used to build nonlinear Thévenin-like networks which preserved the nonlinearity of the original system. Using measurements, the polynomials in such a nonlinear Thévenin-like network can be fitted and it was shown that one can assume any value for the source impedance and the source voltage Maclaurin series can then be appropriately calculated. The maximum power transfer theorem for such nonlinear networks was derived and validated, while accounting for ZIP-load models and phase-shifting transformers. While multi-bus nonlinear reduced-order networks can also be built, these would require a greater number of polynomials to be fitted and hence are more complicated, particularly in the presence of noisy measurements. While the original sigma indices were modified such that their behavior became monotonic as the system load increased, it was observed that the revised sigma indices could still not easily be used to determine the weak buses in the system. In this work, it was assumed that the load changes along a pre-defined direction, and hence when measurements are used to build a nonlinear Thévenin-like network, the network will be fitted for a particular pattern of load/generation change. Once the nonlinear Thévenin-like network is built using measurements, if the loading vector changes drastically, the estimated SNBP may not be accurate. This will have to be carefully investigated going forward.

4. Fitting Methods in Detail and the Roots Methods

4.1 Different numerical methods for estimating the SNBP from measurements

In section 3.4.4, the maximum power transfer theorem (MPTT) was developed to estimate the SNBP for the nonlinear reduced network. Therefore, in this section, numerical experiments using noiseless pseudo-measurements to estimate the SNBP from the MPTT given by (3.35) will be conducted. The effects of noise in the measurements will be discussed in later sections.

4.1.1 Fit a function of α from noiseless measurements

Since the main process in these experiments is to build the functions of α for each component in (3.34) using noiseless data, different possible approaches to fit a general function of α from measurements will be first discussed in this section.

For a given function of α, $f(\alpha)$, as shown in Figure 4.1, a number of pseudo-measurements in the sample range (for example, 60%-70% of the SNBP in this figure) were generated and a curve fit to the samples in this range with the goal of projecting the value of $f(\alpha)$ beyond the sample range, up to the SNBP. The measurements can be used to fit either a polynomial or a Padé approximant to $f(\alpha)$. Three different approaches for fitting $f(\alpha)$ were used: the Matlab built-in Padé fit, self-coded Padé fit and polynomial fit are discussed in the following sections

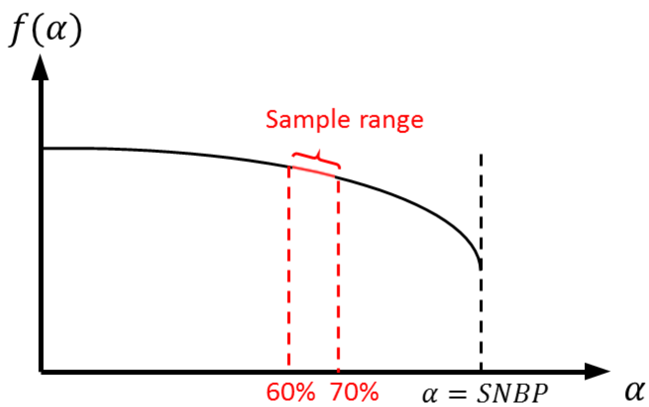

Figure 4.1 Function of α vs. loading-scale factor

4.1.1.1 Self-coded Padé fit

In this case, a rational function of the following form was assumed,

$$f(\alpha) = \sum_{i=0}^{N} c_i\,\alpha^i = \frac{\sum_{i=0}^{M} a_i\,\alpha^i}{\sum_{i=0}^{M+1} b_i\,\alpha^i} = [M/M+1]_{f_\alpha} \tag{4.1}$$

$$2M + 2 = N$$

$$b_0 = 1$$

where N is the degree of the Maclaurin series of $f(\alpha)$, M and M+1 are the degrees of the numerator and denominator polynomial of the Padé approximant, respectively. For a total of $N_{measure}$ measurements sampled over the range of loading values selected for training, ($\alpha_{k,}\, k = 1,2, \dots, N_{measure}$), the corresponding overdetermined set of equations shown in (4.2) was solved to calculate the unknown Padé approximant coefficients α_i, and b_i. Note that the Padé approximant coefficients, α_i and b_i, are written in ascending order of exponents of α.

$$\sum_{i=0}^{M} a_i\, \alpha_k^i - f(\alpha_k)\left(\sum_{i=1}^{M+1} b_i\, \alpha_k^i\right) = f(\alpha_k) \tag{4.2}$$

4.1.1.2 Matlab built-in Padé fit

Similar to the above approach, a set of linear overdetermined equations was solved to directly obtain the coefficients of the Padé approximant. The only difference is that the coefficients, α_i and b_i are written in descending order of exponents of α as given by (4.3).

$$\sum_{i=M}^{0} a_i\, \alpha_k^i - f(\alpha_k)\left(\sum_{i=M+1}^{1} b_i\, \alpha_k^i\right) = f(\alpha_k) \tag{4.3}$$

Though the self-coded Padé fit and Matlab built-in Padé fit are theoretically identical, the subtle difference in the order of coefficients could lead to very different numerical performance. Thus, both will be tested in a subsequent section.

4.1.1.3 Polynomial fit

In this approach, the measurements are used to fit a polynomial to $f(\alpha)$, i.e., to obtain the c_i coefficients in (4.1). The set of equations used to calculate the coefficients is indicated in (4.4):

$$\sum_{i=0}^{N} c_i\, \alpha_k^i = f(\alpha_k) \tag{4.4}$$

4.1.2 Four numerical methods for estimating the SNBP from measurements

As demonstrated in section 4.1.1, there are three approaches to fit the measurements for $f(\alpha)$, while fitting the measuerments for each component in (3.35) is more complicated. For example, for $|V_s(\alpha)|^2$ in (3.35), one can choose to directly fit the polynomial or Padé approximant to the Macluarin series for $|V_s(\alpha)|^2$ by squaring the magnitude of the source voltage measurements or by fitting the polynomial or Padé approximant to $V_s(\alpha)$ from source voltage measurements and then obtain $|V_s(\alpha)|^2$ calculated from the polynomial or Padé approximant of $V_s(\alpha)$ evaluated at different loading-scale factors. Therefore, there are a number of combinations of the ways pseudo-measurements can be used to fit each constituent term in (3.35) and which fitting technique discribed in section 4.1.1 is applied.

Because the Padé approximant is sensitive to roundoff error in the calculations and because the differences in numerical performance of different methods might become significant when building the networks using noisy measurements, it is important to find the best method for estimating the SNBP based on MPTT from measured data. Therefore, four possible numerical methods are discussed in the following section. Their numerical performance was tested on the IEEE 118 bus system. Noiseless pseudo-measauements were generated for loadings in the range of 60%-70% of the maximum system load (SNBP) using MATPOWER and a power-mismatch convergence tolerance of 10^{-8} (For the Best Component method demonstrated in section 4.1.2.2, the tested system is the modified 118 bus system and the sample range is 70%-80% of the SNBP). In each case, 200 measurements were used to fit 61 terms of a polynomial or [30/30] Padé approximant to each component in (3.35). The SNBP is estimated based on the following two approaches: The SNBP point is taken as the eareliest point where either 1) the LHS and RHS values of (3.35) cross each other, or 2) LHS and RHS values were initially converging and then began to diverge.

4.1.2.1 Built-In/Self-Coded method

The MPTT equation given by (3.35) consists of six different components: Z_s, $R_L(\alpha)$, $Z_L(\alpha)$, $|V_s(\alpha)|^2$, $\partial|V_s(\alpha)|^2/\partial\alpha$ and $\partial R_L(\alpha)/\partial\alpha$ from here on abbreviated $\partial|V_s(\alpha)|^2$ and $\partial R_L(\alpha)$, respectively. The variable Z_s is the source impedance of the Thévenin-like network obtained from HEM/Ward network reduction and it is a constant value. Thus there is no need to calculate Z_s from measurements. $R_L(\alpha)$ is the resistive component of the load impedance $Z_L(\alpha)$. Once $Z_L(\alpha)$ is obtained, $R_L(\alpha)$ can be calculated by taking the real part of $Z_L(\alpha)$. Therefore, there are only four components that need attention: $Z_L(\alpha)$, $|V_s(\alpha)|^2$, $\partial|V_s(\alpha)|^2$ and $\partial R_L(\alpha)$.

One simple approach is to directly get $Z_L(\alpha)$, $|V_s(\alpha)|^2$, $\partial|V_s(\alpha)|^2$ and $\partial R_L(\alpha)$ as Padé approximants from their respective measurements, though sometimes this has been handled differently. For example, the function$|V_s(\alpha)|^2$, was built by fitting a Padé approximant to samples of V_s to yield $V_s(\alpha)$and then $|V_s(\alpha)|^2$ was calculated by evaluating the square of the magnitude of $V_s(\alpha)$. The implemention details are summarized in Table 4.1. Note that the measurement $\partial|V_s(\alpha)|^2$ is obtained by calculating the increment in $|V_s|^2$ divided by the increment in loading-scale factor, i.e., $\Delta|V_s|^2/\Delta\alpha$. The $\Delta\alpha$ should be small enough so that the $\partial|V_s|^2$ measurement can accurately represent the derivative of $|V_s|^2$ with respect to α in the original system but at the same time making sure there is sufficient distance between two successive points to identify the voltage change. In this experiment, the $\Delta\alpha$ is chosen to be 10^{-6}. A similar approach is used to get ∂R_L measurements.

Table 4.1 Built-In/Self-Coded method

Components	Pseudo-measurements	Algorithm for fitting measurements
Z_s	Source impedance from HEM/Ward network reduction	
$R_L(\alpha)$	Real part of $Z_L(\alpha)$	
$Z_L(\alpha)$	Z_L	Built-In/Self-Coded Padé-fit Z_L
$\|V_s(\alpha)\|^2$	V_s	1. Built-In/Self-Coded Padé-fit V_s 2. Get $\|V_s\|^2$
$\partial\|V_s(\alpha)\|^2$	$\partial\|V_s\|^2$ ($\frac{\|V_{s1}\|^2-\|V_{s2}\|^2}{\Delta\alpha}$)	Built-In/Self-Coded Padé-fit $\partial\|V_s\|^2$
$\partial R_L(\alpha)$	∂R_L ($\frac{\|R_{L1}\|^2-\|R_{L2}\|^2}{\Delta\alpha}$)	Built-In/Self-Coded Padé-fit ∂R_L

The LHS and RHS of MPTT equation for the IEEE 118 bus system are plotted against α in Figure 4.2 and Figure 4.3 for buses 44 and bus 67, respectively. The SNBP of the 118 bus system is 3.187, obtained using the CPF. Bus 44 and bus 67 are selected intentionally to represent one weak bus and one strong bus, respectively, in the 118 bus system (indentified by the magnitude of voltage change for a given load change near the SNBP). It is seen that for the weak bus, bus 44, both the Built-In and Self-Coded methods can give an accurate estimation of the SNBP, which are 3.179 and 3.181, respectively, with only 0.25% and 0.19% errors, respectively. However, in Figure 4.3, neither Built-In nor the Self-Coded methods give a prediction of the SNBP for the strong bus, bus 67, regardless of whether we use the crossover or the divergence criterion. In other words, the Built-In and Self-Coded methods work well for weak buses but do not work well for strong buses in the system.

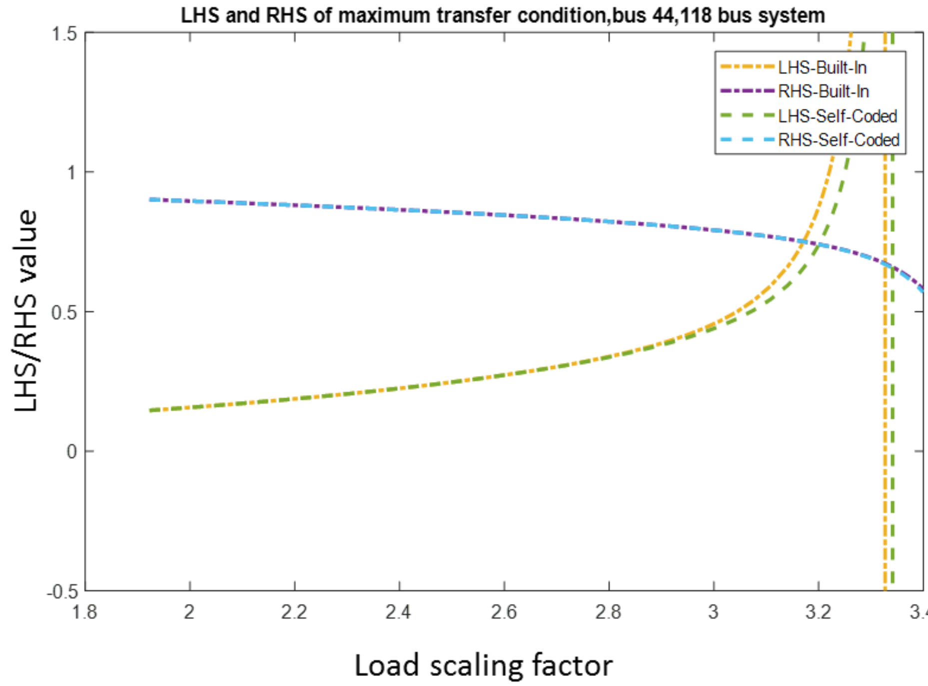

Figure 4.2 LHS and RHS of (3.35) at weak bus number 44 vs. the loading scaling factor for the IEEE 118 bus system

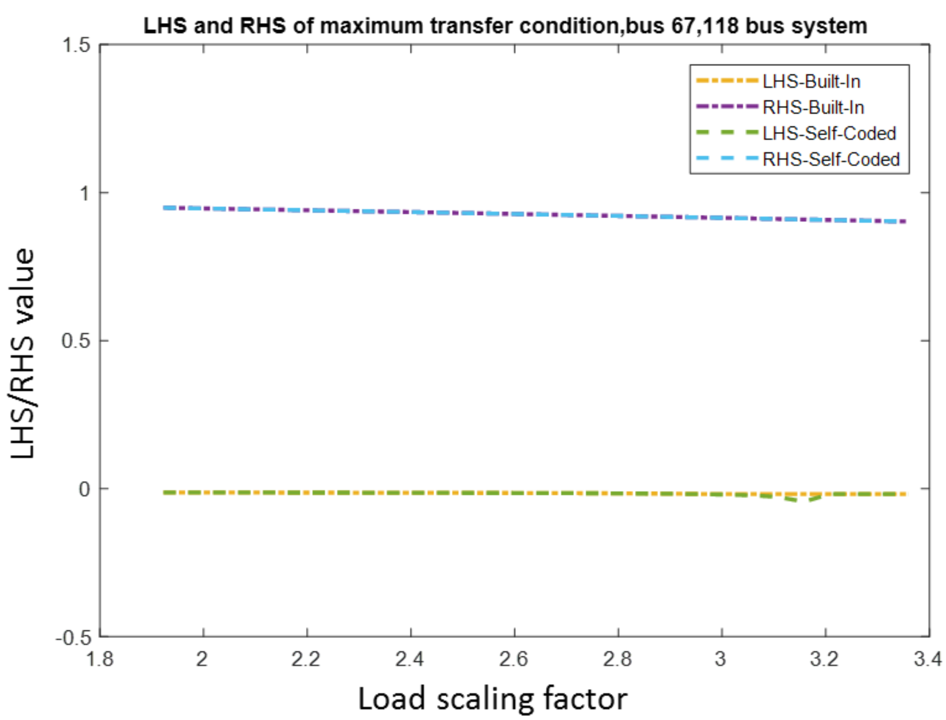

Figure 4.3 LHS and RHS of (3.35) at strong bus number 67 vs. the loading scaling factor for the IEEE 118 bus system

4.1.2.2 Best Component method

In this method, for each constituent of (3.35), ($Z_L(\alpha)$, $|V_s(\alpha)|^2$, $\partial|V_s(\alpha)|^2$ and $\partial R_L(\alpha)$), all of the different ways of fitting the measurements previously mentioned are considered. Note that the 118 bus system here is modified by adding S=1+1j MVA to bus 30, bus 37 and bus 38. The loading value at the SNBP for this modified 118 bus system is 3.172. The loading range for training data obtained as pseudo-measurements is 70%-80% of the SNBP.

First of all, we calculate the "true" value of those variables in the 80%-100% loading range using a 220-digit HEM implementation to obtain the accurate reference values for this range. Then the predictions of these four components are compared with their "true" values in the 90%-100% range. For each component, the representation that most accurately fit the true value was selected as the best way. The best algorithm for building each component is listed in Table 4.2.

Table 4.2 Best Component method

Components	Pseudo-measurements	Best algorithm for fitting measurements
Z_s	Source impedance from HEM/Ward network reduction	
$R_L(\alpha)$	Real part of $Z_L(\alpha)$	
$Z_L(\alpha)$	Z_L	Built-In Padé-fit Z_L
$\lvert V_s(\alpha)\rvert^2$	$\lvert V_s\rvert^2$	Self-Coded Padé-fit V_s
$\partial\lvert V_s(\alpha)\rvert^2$	$\partial\lvert V_s\rvert^2$ ($\frac{\lvert V_{s1}\rvert^2-\lvert V_{s2}\rvert^2}{\Delta\alpha}$)	Self-Coded Padé-fit $\partial\lvert V_s\rvert^2$
$\partial R_L(\alpha)$	∂R_L ($\frac{\lvert R_{L1}\rvert^2-\lvert R_{L2}\rvert^2}{\Delta\alpha}$)	Self-Coded Padé-fit ∂R_L

The LHS and RHS of the MPTT equation using the Best Component method for the modified 118 bus system with the buses-of-interest being buses 22 and 67 are plotted against α in Figure 4.4 and Figure 4.5, respectively. The curves labeled 1) "LHS-mp220", 2) "LHS-Built-In", 3) "LHS-Self-Coded" and 4) "LHS-Best-Component" represent the LHS of MPTT value of Padé approximant 1) from network reduction using 220 digit precision, 2) from measurements using the Built-In method, 3) from measurements using the Self-Coded method and 4) from measurements using the Best Component method. The legend beginning with "RHS-" stands for the RHS of the MPTT value of the Padé approximant. For bus 22, which is a weak bus in the system, the Best Component method is shown to be better than the Buit-In and the Self-Coded methods, but not significantly better. This slightly superior performance has also been seen for some other weak buses when the measurement range remains to be 70%-80%. However, this method does not work well for a strong bus since there is no point where the LHS and RHS cross each other or diverge and thus no prediction can be made as shown in Figure 4.5 (the yellow and purple line).

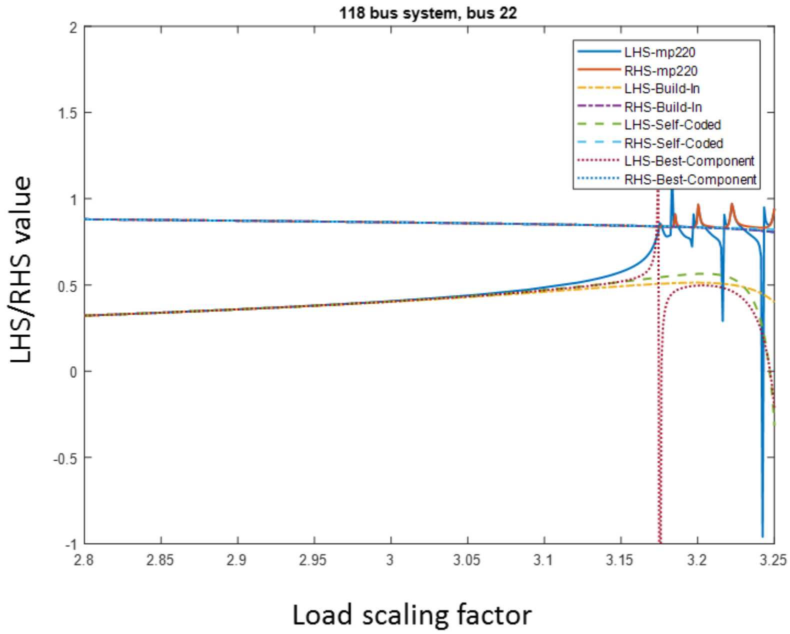

Figure 4.4 LHS and RHS of (3.35) at weak bus number 22 vs. the loading scaling factor for the modified 118 bus system

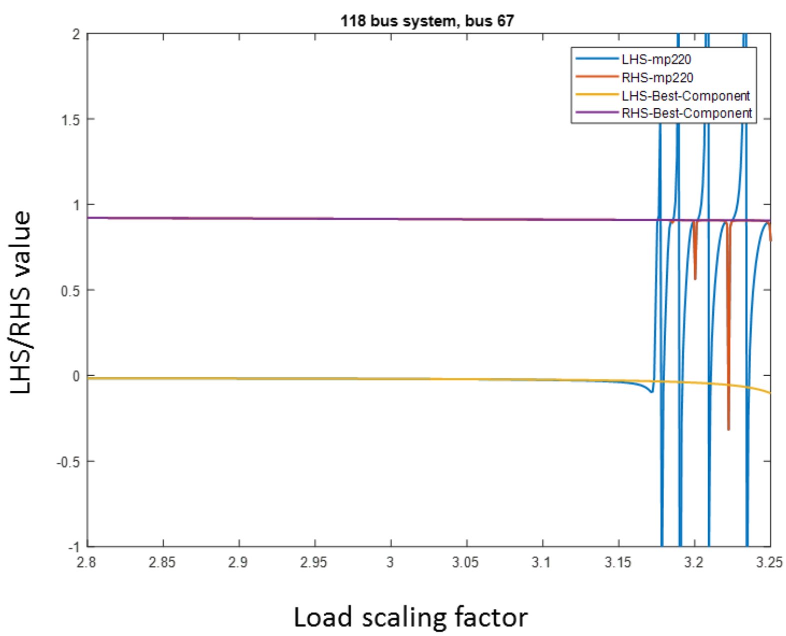

Figure 4.5 LHS and RHS of (3.35) at strong bus number 67 vs. the loading scaling factor for the modified 118 bus system

4.1.2.3 Polynomial Method

The Polynomial Method generates polynomials (rather than Padé approximants) of all functions of α in (3.35). To do that, each component in (3.35) needs to be reformulated to adapt to polynomial form. The process is described below:

The load voltage $V_L(\alpha)$ can be obtained as a Maclaurin series as given by (4.5) from HEM network reduction.

$$V_L(\alpha) = V_L[0] + V_L[1]\alpha + \cdots + V_L[n]\alpha^n + \cdots \tag{4.5}$$

The Maclaurin series for $Z_L(\alpha)$ is given by

$$Z_L(\alpha) = \frac{V_L(\alpha) \cdot V_L^*(\alpha)}{\alpha S^*} \tag{4.6}$$

Note that if the expression for $Z_L(\alpha)$ on the RHS of (4.6) is expanded as a power series using (4.5), one will get a term with a negative exponent of α. The expression for $R_L(\alpha)$ will also have a term with a negative exponent of α. To avoid the negative exponent, the values of the load impedance and load resistance at different values of α can be obtained using the value of $\alpha Z_L(\alpha)$ and $\alpha R_L(\alpha)$ respectively. The corresponding Maclaurin series are given below:

$$\alpha Z_L(\alpha) = \frac{V_L(\alpha) \cdot V_L^*(\alpha^*)}{S^*} \tag{4.7}$$

$$\alpha R_L(\alpha) = Re\big(\alpha Z_L(\alpha)\big) \tag{4.8}$$

The value of $\partial R_L(\alpha)$ at different values of α can be obtained using the value of $\partial[\alpha R_L(\alpha)]/\partial\alpha$ as shown below:

$$\begin{aligned}
&\frac{\partial \alpha R_L(\alpha)}{\partial \alpha} = \alpha \frac{\partial R_L(\alpha)}{\partial \alpha} + R_L(\alpha) \\
&\therefore \frac{\partial R_L(\alpha)}{\partial \alpha} = \frac{\left(\dfrac{\partial \alpha R_L(\alpha)}{\partial \alpha} - R_L(\alpha)\right)}{\alpha}
\end{aligned} \tag{4.9}$$

By multiplying the top and bottom of (3.35) on both sides by α^2, one can obtain:

$$\frac{\partial |V_S(\alpha)|^2}{|V_S(\alpha)|^2} \frac{\alpha \cdot [\alpha R_L(\alpha)]}{\alpha \cdot [\alpha \partial R_L(\alpha)]} = \frac{|\alpha Z_L(\alpha)|^2 - \alpha^2 |Z_S|^2}{|\alpha Z_S + \alpha Z_L(\alpha)|^2} \tag{4.10}$$

Substitute (4.9) into the above equation, the modified MPTT equation for Polynomial Method is obtained, as given by (4.11).

$$\frac{\partial|V_s(\alpha)|^2}{|V_s(\alpha)|^2}\frac{\alpha\cdot[\alpha R_L(\alpha)]}{\alpha\cdot\partial[\alpha R_L(\alpha)]-\alpha R_L(\alpha)}=\frac{|\alpha Z_L(\alpha)|^2-\alpha^2|Z_s|^2}{|\alpha Z_s+\alpha Z_L(\alpha)|^2} \tag{4.11}$$

It can be observed that the reformulated equation given by (4.11) consists of six parts: ① $|\alpha Z_L(\alpha)|^2-\alpha^2|Z_s|^2$, ② $|\alpha Z_s+\alpha Z_L(\alpha)|^2$, ③ $\alpha\cdot[\alpha R_L(\alpha)]$,④ $\alpha\cdot\partial[\alpha R_L(\alpha)]-\alpha R_L(\alpha)$, ⑤ $|V_s(\alpha)|^2$, ⑥ $\partial|V_s(\alpha)|^2$. The next step is to figure out how to get polynomials for ①-⑥ in (4.11) from pseudo-measurements, which are shown below:

①$|\alpha Z_L(\alpha)|^2-\alpha^2|Z_s|^2$:

The *n^th* degree polynomial for $\alpha Z_L(\alpha)$ can be caluclated from αZ_L measurements over a range of loading values ($\alpha_k, k=1,2,\dots N_{measure}$) using the polynomial fit techinique. The polynomial expression for $\alpha Z_L(\alpha)$, also named as $Z_1(\alpha)$, is shown in (4.12).

$$\alpha Z_L(\alpha)=Z_1(\alpha)=Z_1[0]+Z_1[1]\alpha+Z_1[2]\alpha^2+\cdots+Z_1[n]\alpha^n \tag{4.12}$$

Once $\alpha Z_L(\alpha)$ is obtained, the $|\alpha Z_L(\alpha)|^2$, also labeled $Z_2(\alpha)$, can be calculated using (4.13):

$$\begin{aligned}|\alpha Z_L(\alpha)|^2&=Z_2(\alpha)=Z_1(\alpha)\cdot Z_1^*(\alpha^*)\\&=Z_2[0]+Z_2[1]\alpha+Z_2[2]\alpha^2+\cdots+Z_2[2n]\alpha^{2n}\end{aligned} \tag{4.13}$$

Note that the $|\alpha Z_L(\alpha)|^2$ is represented as a 2n-degree polynomial instead of being truncated to an nth degree polynomial to avoid losing information from $Z_1(\alpha)$. The varible Z_s represents the source impedance obtained by network reduction and is a constant. Therefore, ① is obtained by adding (4.13) where the 2nd order term $\alpha^2|Z_s|^2$, is given by (4.14).

$$\begin{aligned}&|\alpha Z_L(\alpha)|^2-\alpha^2|Z_s|^2\\&\quad=Z_2[0]+Z_2[1]\alpha+(Z_2[2]-|Z_s|^2)\alpha^2+\cdots+Z_2[2n]\alpha^{2n}\end{aligned} \tag{4.14}$$

② $|\alpha Z_s+\alpha Z_L(\alpha)|^2$:

Similarly, the expression $\alpha Z_s+\alpha Z_L(\alpha)$ is obtained by adding (4.12) with a 1st order term αZ_s as given by (4.15).

$$\begin{aligned}&|\alpha Z_L(\alpha)|^2-\alpha^2|Z_s|^2\\&\quad=Z_2[0]+Z_2[1]\alpha+(Z_2[2]-|Z_s|^2)\alpha^2+\cdots+Z_2[2n]\alpha^{2n}\end{aligned} \tag{4.15}$$

Then ② can be calculated using the following equation:

$$\begin{aligned}|\alpha Z_s+\alpha Z_L(\alpha)|^2&=Z_3(\alpha)=[\alpha Z_s+\alpha Z_L(\alpha)]\cdot[\alpha Z_s+\alpha Z_L(\alpha)]^*\\&=Z_3[0]+Z_3[1]\alpha+\cdots Z_3[2n]\alpha^{2n}\end{aligned} \tag{4.16}$$

③ $\alpha\cdot[\alpha R_L(\alpha)]$:

The polynomial for $\alpha R_L(\alpha)$ is calculated by taking the real part of $\alpha Z_L(\alpha)$, and then multiply it with α. The process is shown below:

$$\alpha R_L(\alpha) = R_1(\alpha) = Re\big(\alpha Z_L(\alpha)\big) \\ = R_1[0] + R_1[1]\alpha + \cdots R_1[n]\alpha^n \tag{4.17}$$

$$\alpha \cdot [\alpha R_L(\alpha)] = \alpha R_1(\alpha) = R_1[0]\alpha + R_1[1]\alpha^2 + \cdots + R_1[n]\alpha^{n+1} \tag{4.18}$$

④ $\alpha \cdot \partial[\alpha R_L(\alpha)] - \alpha R_L(\alpha)$

The polynomial for $\partial[\alpha R_L(\alpha)]$ is obtained by taking the derivative of $\alpha R_L(\alpha)$ with respect to α as shown below:

$$\partial[\alpha R_L(\alpha)] = R_2(\alpha) = \frac{\partial R_1(\alpha)}{\partial \alpha} \tag{4.19}$$

$$= R_2[0] + R_2[1]\alpha + \cdots R_2[n-1]\alpha^{n-1}$$

Then ④ is given by:

$$\begin{aligned} &\alpha \cdot \partial[\alpha R_L(\alpha)] - \alpha R_L(\alpha) = \\ &= \alpha \cdot (\, R_2[0] + R_2[1]\alpha + \cdots R_2[n-1]\alpha^{n-1}) \\ &\quad - (R_1[0] + R_1[1]\alpha + \cdots R_1[n]\alpha^n) \\ &= -R_1[0] + (\, R_2[0] - R_1[1])\alpha + \cdots + (\, R_2[n-1] - R_1[n])\alpha^n \end{aligned} \tag{4.20}$$

⑤ $|V_s(\alpha)|^2$:

The n^{th} order polynomial for $V_s(\alpha)$ is obtained from the source voltage measurements using the polynomial fit technique and then ⑤ is obtained by using (4.21).

$$|V_s(\alpha)|^2 = V_s(\alpha) \cdot V_s^*(\alpha^*) \tag{4.21}$$

⑥ $\partial|V_s(\alpha)|^2$:

The term ⑥ is obtained by taking the derivative of the polynomial for ⑤ with respect to α.

The MPTT results using the Polynomial Method for weak bus 44 and strong bus 67 are plotted in Figure 4.6 and Figure 4.7, respectively. The labels “LHS-MODEL-Polynomial” and “RHS-MODEL-Polynomial” represent the LHS and RHS values, respectively, of (4.11) obtained using network reduction techniques [27]. The labels “LHS-Polynomial” and “RHS-Polynomial” represent the LHS and RHS values of (4.11), respectively, obtained by fitting measurements to a polynomial. Observe that the Polynomial Method can give a reasonable estimate (by using the divergence criterion in this case) when obtaining the power series from network reduction. However, when using the polynomials obtained from measurements, this method does not extrapolate the LHS well far away from the training data range. Therefore, use of the Polynomial Method is not feasible for predicting the SNBP.

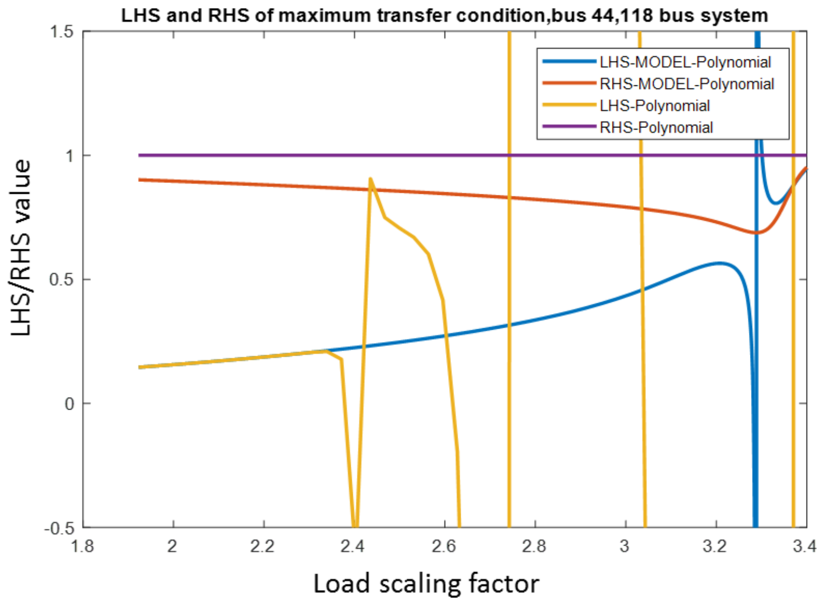

Figure 4.6 LHS and RHS of (4.11) at weak bus number 44 vs. the loading scaling factor for the IEEE 118 bus system

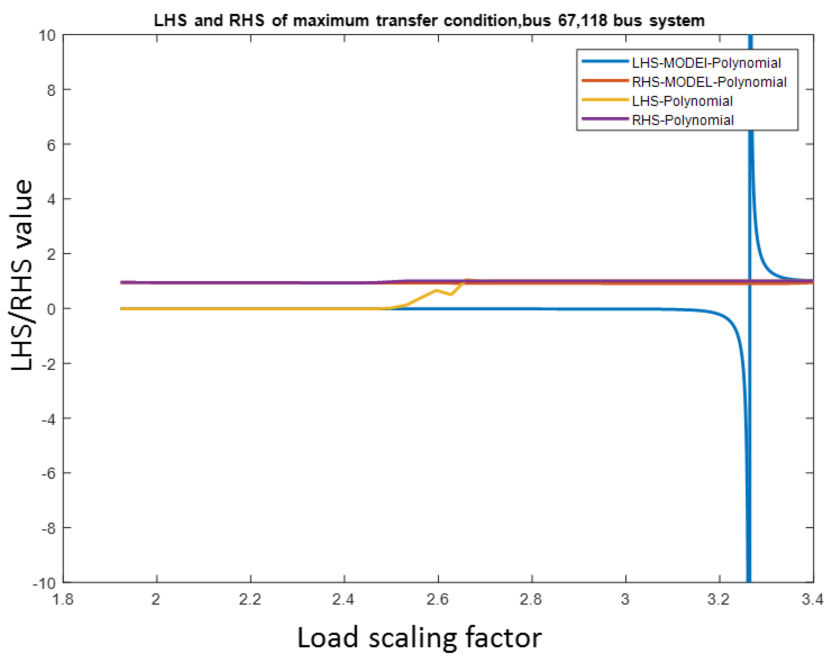

Figure 4.7 LHS and RHS of (4.11) at strong bus number 67 vs. the loading scaling factor for the IEEE 118 bus system

4.1.2.4 $\mathbf{Z_{th}(\alpha)}$ method

The idea of the $Z_{th}(\alpha)$ method is similar to conventional TE-based method. The rest of the system is modeled as a voltage source connected through a Thévenin impedance as shown in Figure 4.8. Note that unlike the Thévenin-like network, in which the impedance Z_s from HE-reduction is constant, the Thévenin impedance in Figure 4.8 is a function of α. It can be calculated based on its definition:

$$Z_{th}(\alpha) = -\frac{\frac{\partial V_L(\alpha)}{\partial \alpha}}{\frac{\partial I_L(\alpha)}{\partial \alpha}} = -\frac{\partial V_L(\alpha)}{\partial\left(\frac{\alpha S^*}{V_L^*(\alpha^*)}\right)} = -\frac{\partial V_L(\alpha) \cdot V_L^*(\alpha^*) \cdot V_L^*(\alpha^*)}{S^*\left(V_L^*(\alpha^*) - \alpha \cdot \partial V_L^*(\alpha^*)\right)} \tag{4.22}$$

The load impedance $Z_L(\alpha)$ is given by:

$$Z_L(\alpha) = \frac{V_L(\alpha) \cdot V_L^*(\alpha^*)}{\alpha S^*} \tag{4.23}$$

The potential advantage of this approach is that at the SNBP, the magnitude of the Thévenin impedance is equal to the magnitude of the load impedance, i.e., $|Z_{th}(\alpha)| = |Z_L(\alpha)|$ and the test for the SNBP is much simpler.

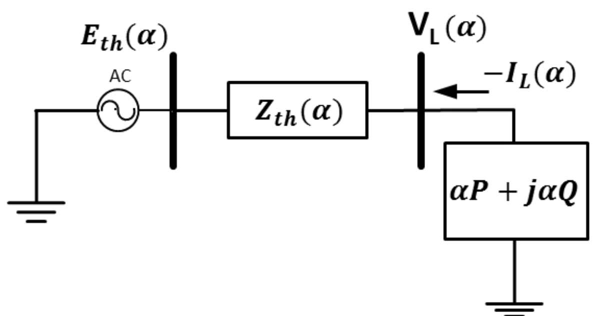

Figure 4.8 Two-bus equivalent diagram for $Z_{th}(\alpha)$ method

Plotted in Figure 4.9 is the magnitude of $Z_{th}(\alpha)$ and $Z_L(\alpha)$ vs. load-scaling factor for the IEEE 118 bus system with bus-of-interest being bus 48, a strong bus in the system. It is thought that for strong buses, $Z_{th}(\alpha)$ method may reliably have a crossover while the Built-In/Self-Coded methods or Best Component method do not. Thus the $Z_{th}(\alpha)$ method can give a prediction of SNBP for strong buses while the Built-In/Self-Coded methods or Best Component method do not, because the LHS and RHS do not cross each other or diverge. However, this method gives a non-conservative estimate of SNBP. (In Figure 4.9, the estimate is around 3.3 while the SNBP loading value for the system is 3.187.) In addtion, uses the same assumption as TE-based method, namely that the voltage source remains constant during the sampling period. Therefore, this method will not be considered in later research work in this report. But it might show benefits when using noisy measurements.

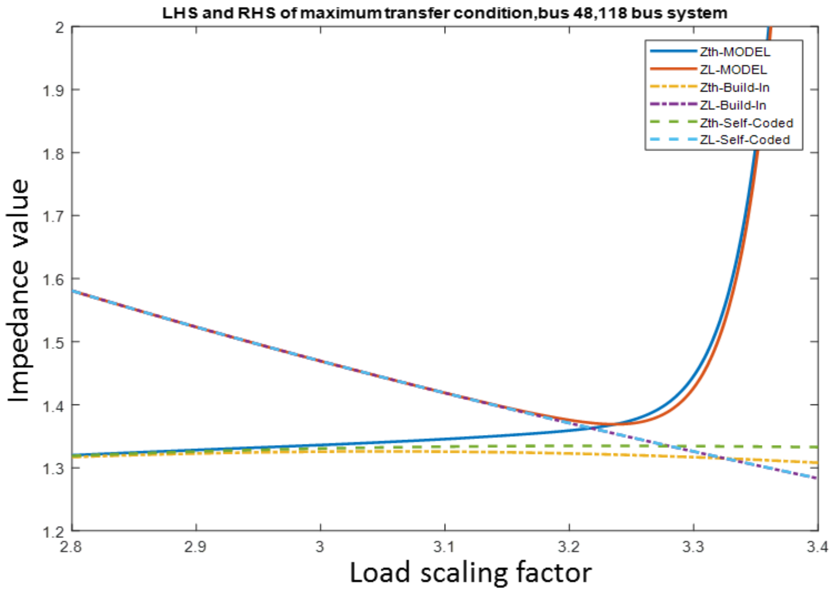

Figure 4.9 Magnitude of Z_L and Z_{th} at strong bus number 48 vs. the loading scaling factor for the IEEE 118 bus system

4.2 Validating the Maximum Power Transfer Theorem

As shown in section 4.1, when different numerical methods (including network reduction techniques which should be accurate to within roundoff error) are applied to MPTT, the SNBP could be predicted with acceptable accuracy for so-called weak buses, but not for so-called strong buses. To prove that the problem was not with the equation, but the precision with which the equation was evaluated, extended precision (250 digit) was used in generating the constituents of (3.35) for strong buses using network reduction techniques. As shown in Figure 4.10 (b), when extended precision is used for strong buses, the LHS and RHS of (3.35) indeed are equal at the SNBP. (The calculated SNBP for the (non-modified) 118 bus system using extended precision is 3.189). Note that there is a "blip" in the LHS curve when using double precision and it might affect the accuracy of SNBP estimation in some cases. This behavior will be further discussed in later sections.

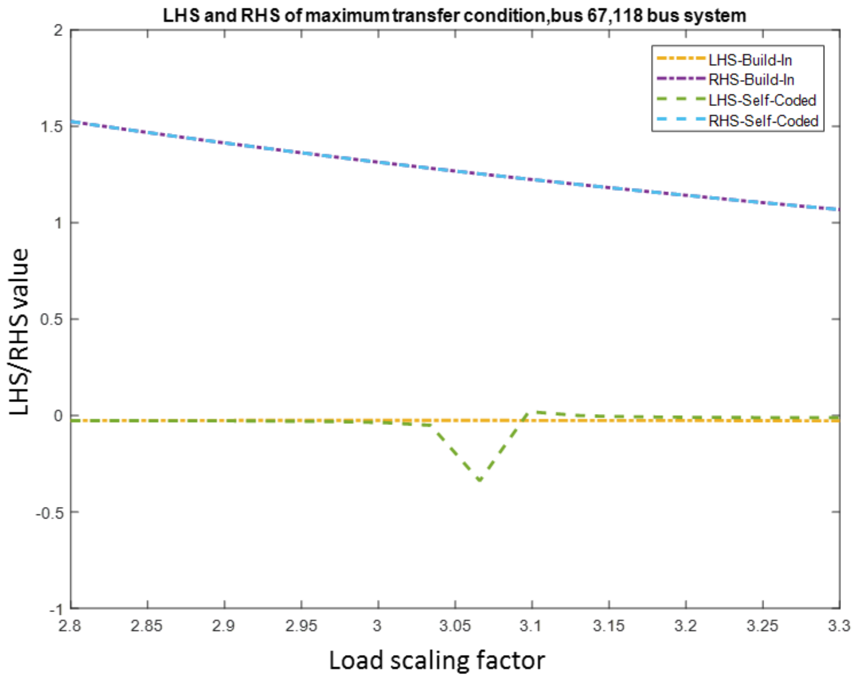

(a) Double precision

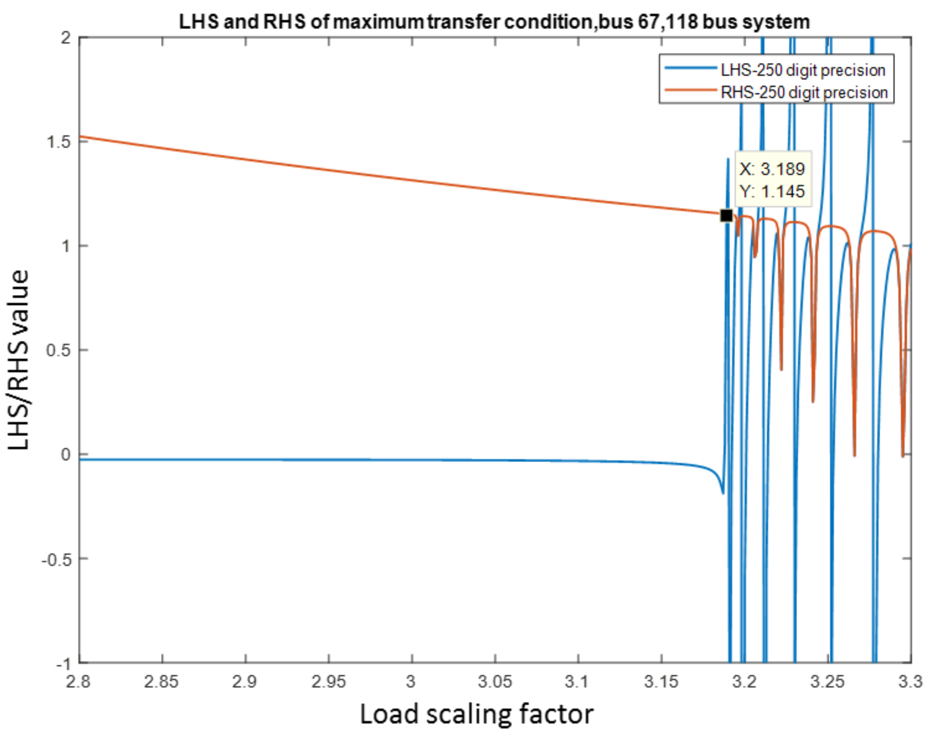

(b) 250 digits of precision

Figure 4.10 LHS and RHS of (3.35) at strong bus number 67 vs. the loading scaling factor for the IEEE 118 bus system

4.3 Numerical comparison of different methods using noiseless measurements

In the above section, the MPTT was validated by implementing it using high precision and, in section 4.1, different numerical methods were investigated to estimate the SNBP based on the MPTT from measurements. However, it was shown that, regardless of the method used, when only double precision is used the method cannot predict the SNBP using data from strong buses. Hence, to be effective, SNBP prediction algorithm should be applied to PMU buses that are close to the weakest buses in the system. Also it was observed from the above numerical experiments that the Built-In, Self-Coded and Best Component methods are promising if applied to weak buses, but a larger performance sample will aid in drawing a conclusion with high confidence. Therefore, more extensive tests were conducted using these three methods with 11 weak buses on the 118 bus system in the following sections.

4.3.1 Modified 118 bus system

The tested 118 bus system is modified by adding a small load, S=1+1jMVA, to bus 30, bus 37 and bus 38 in order to increase the number of testable weak buses in the system. (Because there is no real or reactive power load at those PQ buses in the original system, the MPTT could not be applied to those buses.) The loading value at the SNBP for this modified 118 bus system is 3.172 (versus 3.189 for the original system), obtained using the CPF.

4.3.2 Finding the ten weakest buses from modal analysis

Arguably, the most well-known method of determining the weak buses of a system is modal analysis [29], which will be used here to determine the ten weakest buses of the modified 118 bus system.

The modal analysis method calculates the eigenvalue and eigenvector of the reduced Jacobian matrix based on the relation between the incremental bus voltage magnitudes and their respective incremental reactive power injections. The smallest eigenvalue can be used to estimate the stability margin and the participation factor calculated from the left and right eigenvectors corresponding to the critical mode, which provides insight about which bus loads have significant impact on the system voltage stability. The buses with relatively large participation factors in the smallest eigenvalue are determined to be the weak buses in the system. Since modal analysis is based on a linear approximation of the system model, the order of the buses from the weakest to the strongest might change as the operating condition changes.

The top ten weakest buses (in decreasing order of weakness) obtained from modal analysis using VSAT [35] and our own MATLAB modal-analysis program for the modified 118 bus system are listed in Table 4.3, both calculated when the loading of the system is close to its SNBP. Note that when using VSAT to identify the weakest buses, we can only scale the system load up to 2.35 because VSAT can not give a converged solution beyond that. It can be observed that there is a one-to-one correspondence between VSAT and MATLAB program except for the 10th weakest bus, i.e., the strongest one among the 10 weakest buses. Thus, this shows that, in this case, the order of the top ten weakest buses changes only slightly as the loading changes. The first nine weakest buses (identical for VSAT and MATLAB) and the 10th weakest buses both for VSAT and MATLAB, totaling eleven buses, are selected to be tested in the following section.

Table 4.3 Ten weakest buses for the modified 118 bus system using modal analysis

	VSAT (loading=2.35)		MATLAB (loading=3)	
Smallest eigenvalue	2.947722		3.035	
No.	Bus	Part.Fac.	Bus	Part.Fac
1	21	1	21	1
2	22	0.80834	22	0.83712
3	20	0.47027	20	0.46517
4	44	0.05503	44	0.04171
5	43	0.02785	43	0.0195
6	45	0.01984	45	0.01658
7	23	0.01407	23	0.01603
8	38	0.00313	38	0.00218
9	30	0.0006	30	0.00085
10	37	0.00016	17	0.00012

4.3.3 Numerical results

Numerical tests were conducted on the Built-In, Self-Coded and Best Component methods for the eleven weakest buses in the modified 118 bus system with different ranges of noiseless pseudo-measurements. In each experiment, 200 measurements were used to fit a [30/30] Padé approximant for each variable. The SNBP was predicted either by the crossover or divergence behavior of the LHS and RHS values of the MPTT equation.The numerical results are shown as follows, where "Average error" is the average of the absolute value of the errors:

4.3.3.1 Measurements in the range of 50%-60% of the SNBP

In this experiment, the measurements in the 50%-60% training range were used to fit the Padé approximant. The percent error in SNBP for the 11 weakest buses using the three numerical methods are listed in Table 4.4 and the absolute value of the errors is shown in Figure 4.11.

Table 4.4 Percent error in SNBP estimation for measurements in the 50%-60% training range for the modified 118 bus system

Bus no.	Numerical methods			Average error over all methods (%)
	Built-In (%)	Self-Coded (%)	Best Component (%)	
21	4.17087	6.882093	8.237705	6.430223
22	12.16898	2.301387	2.04918	5.506515
20	2.175284	9.174023	6.052963	5.800757
44	-1.25158	0.29319	-0.05359	0.532787
43	-0.02207	0.576923	0.608449	0.40248
45	-1.8285	5.422446	5.453972	4.234973
23	-5.64313	12.54729	13.11475	10.43506
38	-2.60404	-0.81021	-1.50378	1.639344
30	0.063052	5.611602	-3.97226	3.215637
37	-0.90479	6.472257	7.796343	5.057797
17	-2.71122	13.52459	18.63178	11.62253
Average error over all buses	3.04941	5.783274	6.134071	4.988918

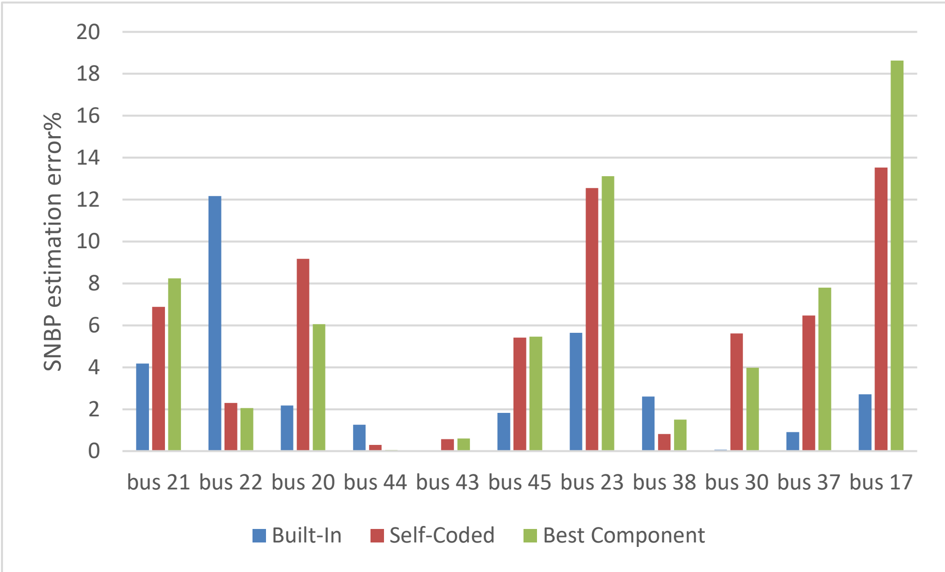

Figure 4.11 Percent error in SNBP estimation for measurements in the 50%-60% training range

4.3.3.2 Measurements in the range of 60%-70% of the SNBP

The numerical results of SNBP estimation using measurements in the 60%-70% training range are shown in Table 4.5 and Figure 4.12.

Table 4.5 Percent error in SNBP estimation for measurements in the 60%-70% training range for the modified 118 bus system

Bus no.	Numerical methods			Average error over all methods (%)
	Built-In (%)	Self-Coded (%)	Best Component (%)	
21	6.431274	4.854981	7.124842	6.137032
22	0.189155	-0.09458	-0.15763	0.147121
20	10.40353	8.228247	8.732661	9.12148
44	-8.62863	0.955233	1.144388	3.576082
43	0.797604	2.689155	2.058638	1.848466
45	-2.60404	0.513871	0.513871	1.210593
23	-14.029	4.287516	7.093317	8.469945
38	0.545397	-2.60404	-2.60404	1.917823
30	-5.42245	4.602774	3.87768	4.6343
37	2.657629	3.225095	3.571879	3.151534
17	2.900378	9.962169	8.417402	7.093317
Average error over all buses	4.964462	3.819787	4.117849	4.300699

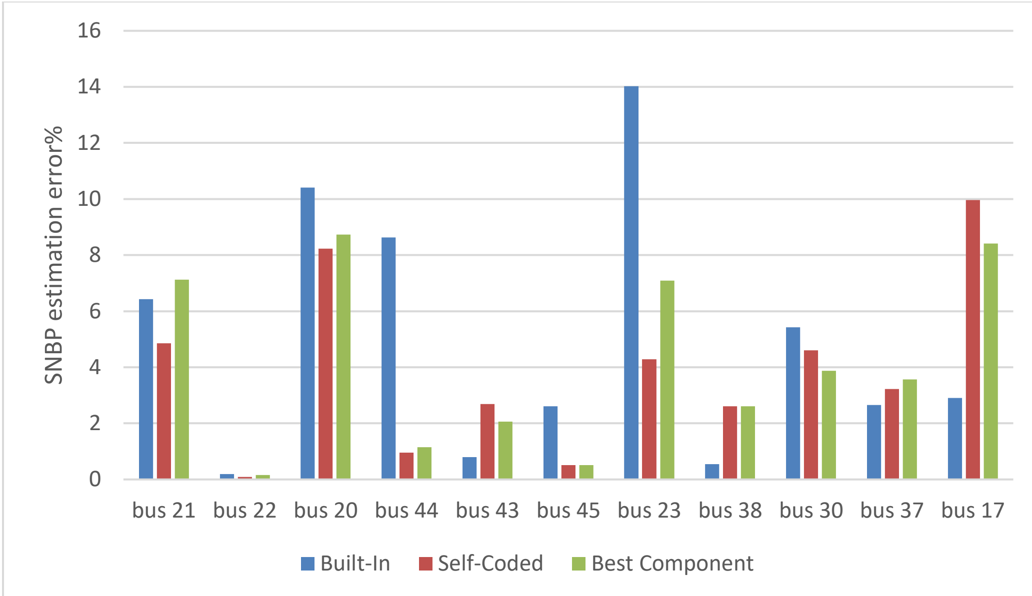

Figure 4.12 Percent error in SNBP estimation for measurements in the 60%-70% training range

4.3.3.3 Measurements in the range of 70%-80% of the SNBP

The numerical results of the SNBP estimation using measurements in the 70%-80% training range are shown in Table 4.6 and Figure 4.13.

Table 4.6 Percent error in SNBP estimation for measurements in the 70%-80% training range for the modified 118 bus system

Bus no.	Numerical methods			Average error over all methods (%)
	Built-In (%)	Self-Coded (%)	Best Component (%)	
21	0.094578	-0.44136	-0.50441	0.346784
22	1.481715	1.261034	0.031526	0.924758
20	1.680328	1.806431	0.040984	1.175914
44	-0.49496	-1.44073	-1.59836	1.178016
43	1.081337	-0.02207	-0.24275	0.448718
45	0.513871	0.040984	0.040984	0.198613
23	2.909836	1.869483	1.995586	2.258302
38	-0.36885	-0.46343	-0.58953	0.473939
30	0.135561	-0.84174	-0.84174	0.606347
37	0.671501	1.20744	1.302018	1.060319
17	2.373897	1.428121	1.428121	1.74338
Average error over all buses	1.073312	0.983893	0.783274	0.946826

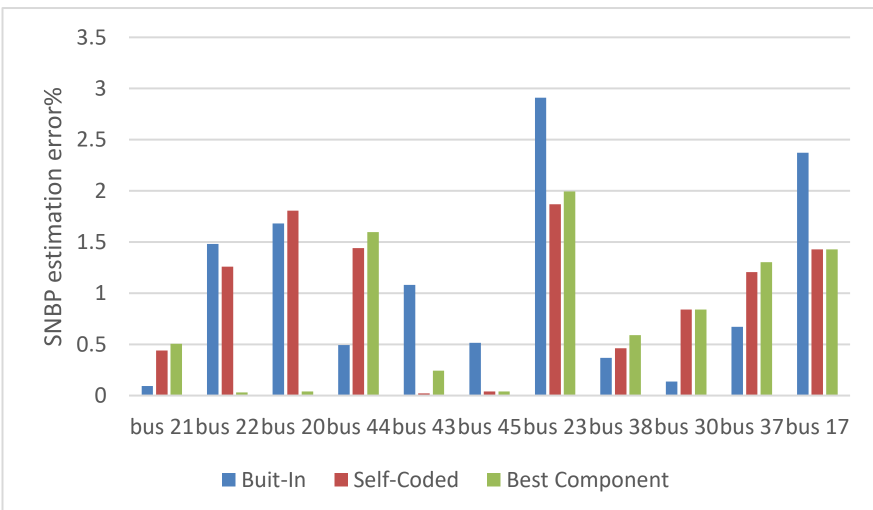

Figure 4.13 Percent error in SNBP estimation for measurements in the 70%-80% training range

4.3.4 Conclusion

From the above numerical results, it can be observed that the average errors in SNBP estimation using the three different methods are: 3%-6% for measurements in the 50%-60% range; 3%-5% for measurements in the 60%-70% range; about 1% for measurements in the 70%-80%. If simply taking the average of the average of the absolute values of the errors for the three methods, the approximate errors for each training data range are shown in Figure 4.14. It can be seen that the closer the measured data is to the SNBP, the smaller is the error in the SNBP estimate.

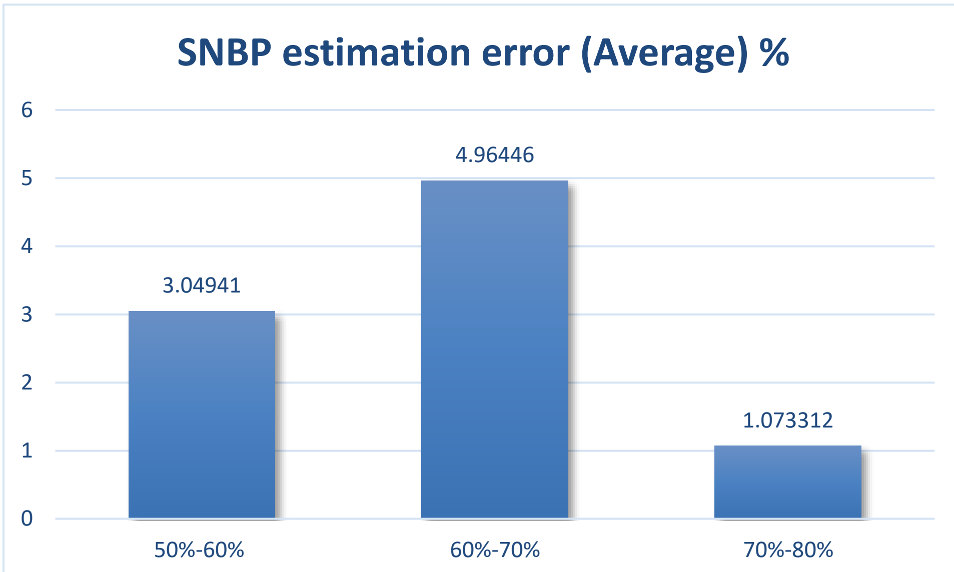

Figure 4.14 Percent error in SNBP estimation for different training data range (average of the absolute value of errors)

If we average over the 11 weakest buses (no absolute value), the Built-In method gives the best results as shown in Figure 4.15. Other methods may be competitive if more sophisticated algorithms of outlier detection are used.

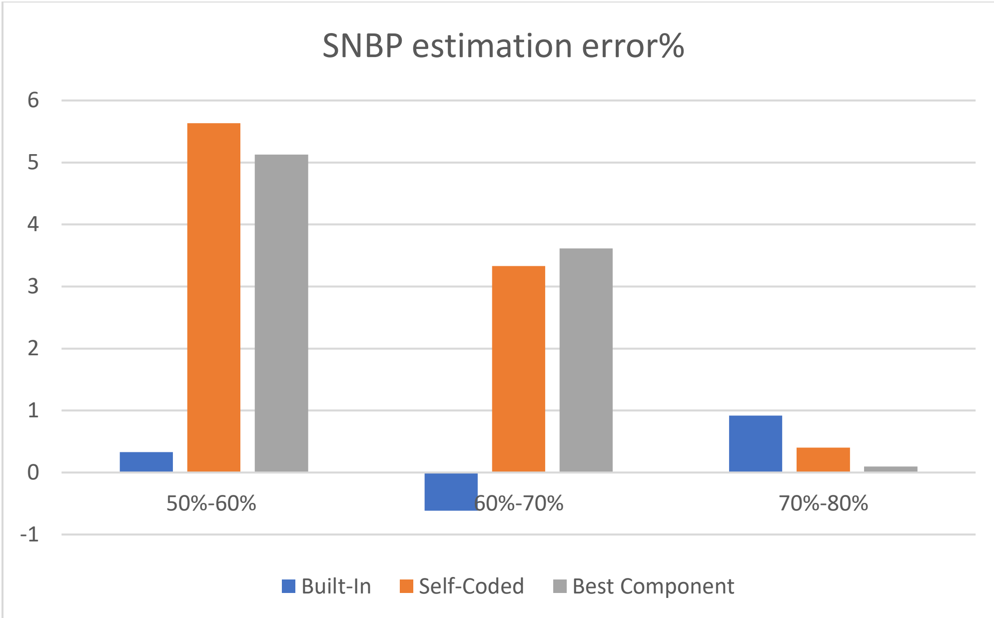

Figure 4.15 Percent error in SNBP estimation for different training data range (average errors)

4.3.5 More analysis on the numerical results

When the range of the measurements is 60%-70% of the SNBP, the numerical results as shown in Figure 4.12 show that the errors in SNBP estimation using the Built-In method for most buses are less than 7%, which is acceptable. However, the estimation error at bus 23 is 14.029%. (The estimated SNBP is 2.727 while the true SNBP of the system is 3.172), which obviously is an outlier. Hence, in order to improve the accuracy of our method for estimating the SNBP, we focus now on finding the cause of this outlier. Bus 43, for which the estimation error is only 0.797%, is also included in the following tests for comparison.

If we generate the MPTT plot for bus 23 as shown in Figure 6.23 (a), it can be observed that the yellow line which represents the LHS of (3.35) has a spike at around 2.727 and this point will be detected as the SNBP by the divergence criteria, which is incorrect. Then by analyzing each component in the LHS of (3.35) ($\partial|V_s|^2, \partial R_L(\alpha), R_L(\alpha)$ and $|V_s|^2$), we find that the cause comes from $\partial|V_s|^2$ as shown in Figure 6.24 (a).

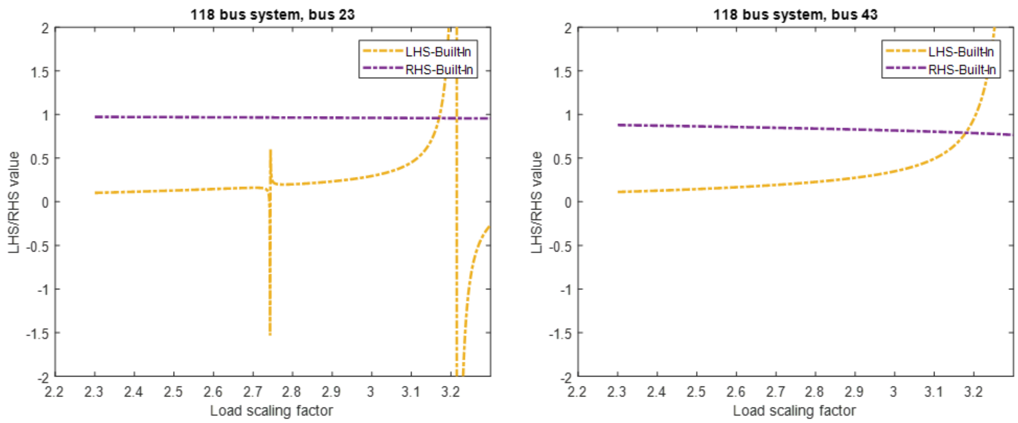

(a) Bus 23 (b) Bus 43

Figure 4.16 LHS and RHS of (3.35) at bus 23 or bus 43 vs. loading scaling factor

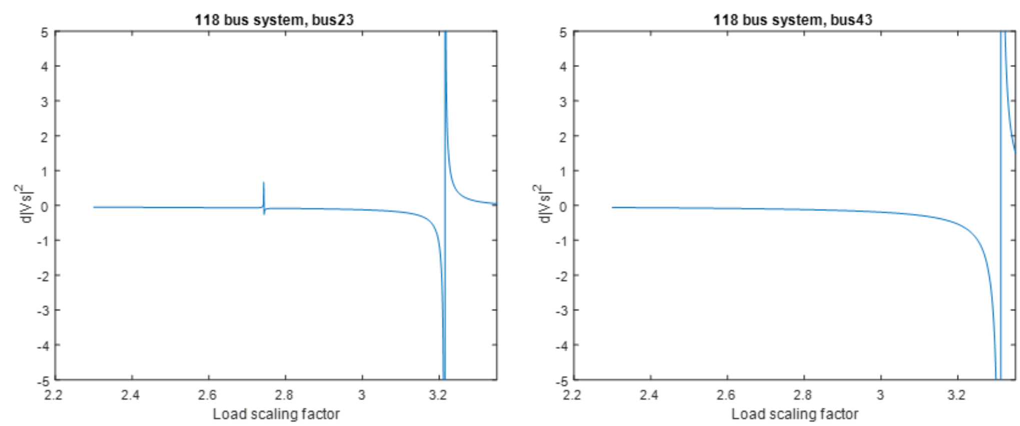

(a) Bus 23 (b) Bus 43

Figure 4.17 $\partial|V_s(\alpha)|^2$ at bus number 23 or bus 43 vs. loading-scaling factor

To dive further into determining the root cause of blip in Figure 6.24 (a), the poles and zeros of the Padé approximants of $\partial|V_s|^2$for bus 23 and bus 43 are plotted in Figure 4.18. It can be seen that there are a number of poles/zeros accumulating on the real axis in the range [1.9, 2.22], which is the measured data range. Since we only focus on the range beyond the measured data range for estimating the SNBP, these poles/zeros will not affect the estimation. And the pole/zero that is located at around 3.4 should be the actual root of the Padé approximant obtained from measurements and will be taken as the estimated SNBP if using the roots method. (Using the roots method, an estimated SNBP of 3.4 is significantly inaccurate, which is why the MPTT is used.) Observe that for bus 23, there is a pole-zero pair in the range between the boundary of the measured data range and the root of the Padé approximant, located at around 2.73 (also inaccurate if the roots method were to be used) and this pole-zero pair will affect the behavior of the LHS and RHS of (3.35). Therefore, when we search for the estimated SNBP detected by crossover or divergence behavior starting from the boundary of the measured data range, the estimation of the SNBP is

2.727, which is incorrect. More discussion on the poles and zeros of the Padé approximant obtained from measurements is contained in section 4.4, as well as suggested remedies for this problem. As will be seen in section 4.4, this pole-zero pair for bus 23 is caused by round-off error.

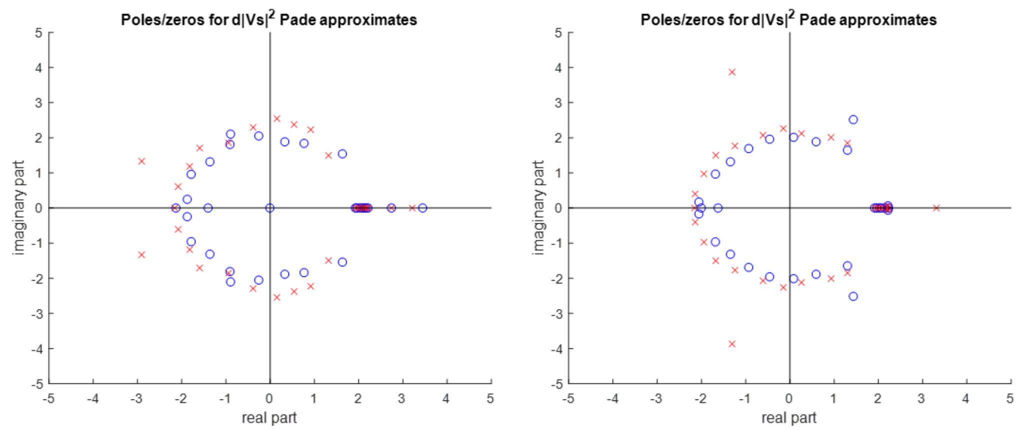

(a) Bus 23 (b) Bus 43

Figure 4.18 Pole-zero plot for $\partial|V_s(\alpha)|^2$ at bus number 23 and bus 43

4.4 Using the roots method to estimate the SNBP

In addition to using the MPTT, one can use the roots (poles/zeros) of the voltage Padé approximant to estimate the SNBP using the so-called roots method. As seen in section 4.3.5, the location of the poles/zeros of the Padé approximant is an effective way to analyze numerical issues. Hence the numerical performance of the roots method will be discussed in the following section.

4.4.1 The effect of order of Padé approximant

The pole-zero plots for different orders of [*M*/*M*+1] Padé approximants of V_L at bus 23 are plotted in Figure 4.19 using various numbers of series terms, *n*. The range of the measurements used to fit the Padé approximant is 60%-70% of the SNBP, which is 1.9032 to 2.2204 in α values. The total number of measurements is 200. It is seen from Figure 6.26 (a) that when the number of terms, n, used to calculate the Padé approximants is insufficient, like *n*=4 in this case, there is no pole/zero on the real axis and thus no SNBP prediction can be made using the roots method. Looking at Figure 6.26 (b) (c) and (d),we observe that the pole/zero that is located at around 3.4 is viewed to be the actual root of Padé approximants of V_L fitted from measurements and will be referred to "the meaningful" pole/zero in the rest of the work. It was observed that the location of the meaningful pole/zero changes slightly as *n* changes. However, as *n* increases, beyond a certain threshold, as seen in Figure 6.26 (c), poles/zeros occur on the real axis inside and just beyond the training data range, i.e., [1.9032, 2.2204]. This type of poles/zeros will be referred to "training range" poles/zeros. When *n*=20, those training range poles/zeros are all within the training data range and thus will not affect the accuracy of the SNBP estimation. When *n* increases to 50, as shown in Figure 6.26 (d), many poles/zeros accumulating on a circle centered at the origin, which will be referred to as "the circle" poles/zeros in the following sections. Also, observe in Figure 6.26 (d) that there is an (approximately real-valued) near-training-range pole/zero located at 2.312, which is beyond the training data range and would be taken as the estimated SNBP from roots method, leading to inaccuracy in SNBP prediction.

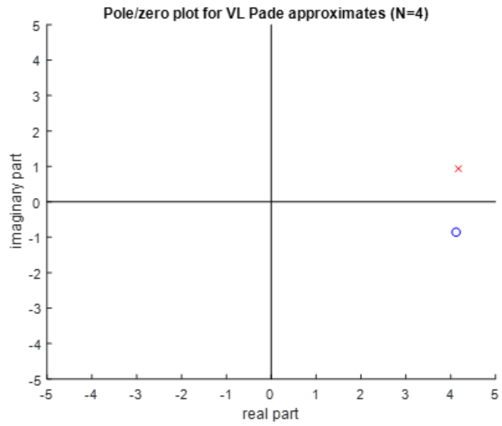

(a) *n*=4

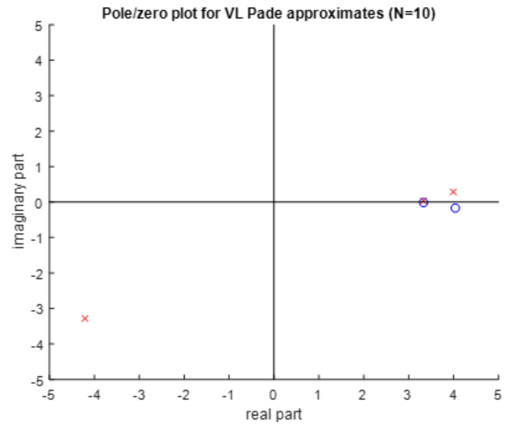

(b) *n*=10

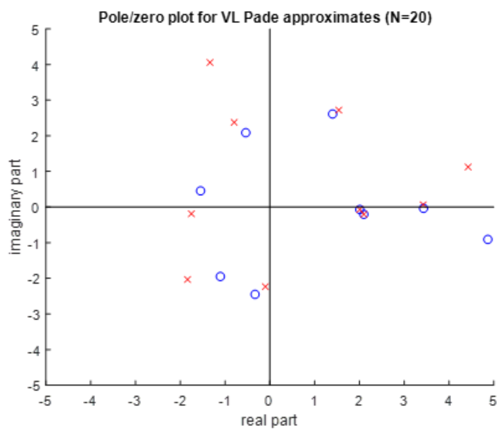

(c) *n*=20

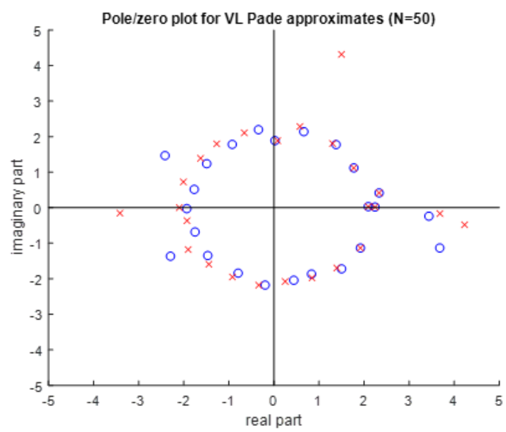

(d) *n*=50

Figure 4.19 Pole-zero plot for different order of V_L Padé approximant

Let us define the following variables.

- N_{start} is the number of terms at which the Padé approximant starts to have a pole/zero on or near the real axis, which consequently would allow the prediction of the SNBP by the roots method (as seen in Figure 6.26 (b)) to be reasonably accurate,
- N_{range} is the number of terms at which the Padé approximant starts to have training range poles/zeros all in the training range but these roots remain within the training range so they do not affect the accuracy of the SNBP estimation (as seen in Figure 6.26 (c))
- N_{bad} corresponds to the number of terms of the Padé approximant when there exist training range poles/zeros located beyond the training data range as more and more spurious poles/zeros appear, thus causing estimation errors (as seen in Figure 6.26 (d)).

The general conclusion from a series of tests on the modified 118 bus system is that in general: $N_{start} = 7$, $N_{range} = 12$ and $N_{bad} = 21$. The specific SNBP estimation results for bus 23 are shown in Figure 4.20.

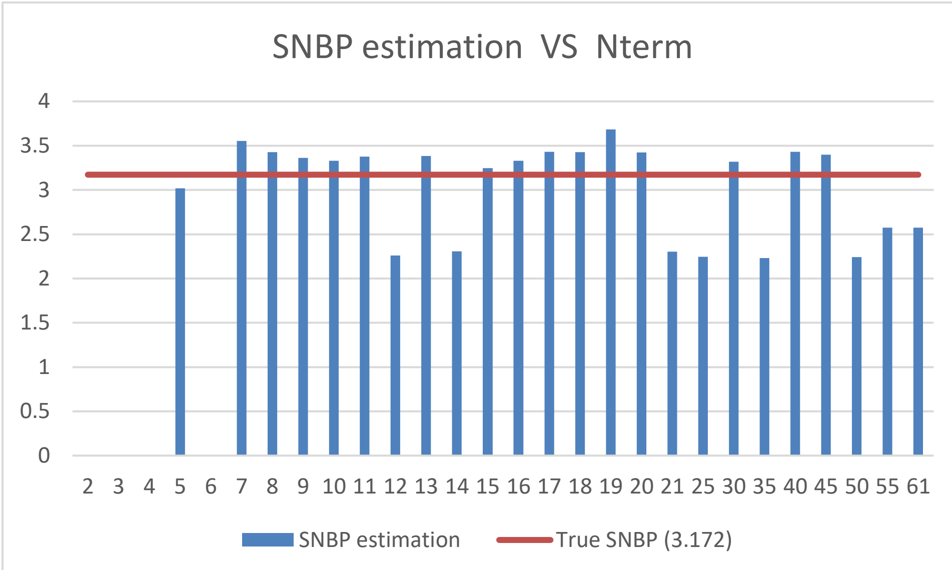

Figure 4.20 The estimation of SNBP vs. number of series terms used in building the Padé approximant of V_L using 200 measurements

As seen from Figure 4.20, one does not need many terms to obtain a reasonably accurate estimate of the SNBP and using too many terms will reduce the accuracy of the estimation eventually. Typically, n=12 to 20 will give a reasonably good SNBP estimation.

4.4.2 The effect of number of measurements

As demonstrated in section 4.1.1, the Padé approximant is calculated by solving a set of overdetermined equations. Increasing the number of measurements is expected to reduce round-off error. If we repeat the simulation in section 4.4.1 with 2000 measurements, the result we obtain is: $N_{start} = 5$, $N_{range} = 18$ and $N_{bad} = 24$, which means we can use a wider range of n selections and still obtain a good estimate. The specific SNBP estimation results are shown in Figure 4.21. Notice that the SNBP estimate is more reliable when 2000 samples are used versus 200 samples, as shown in Figure 4.20.

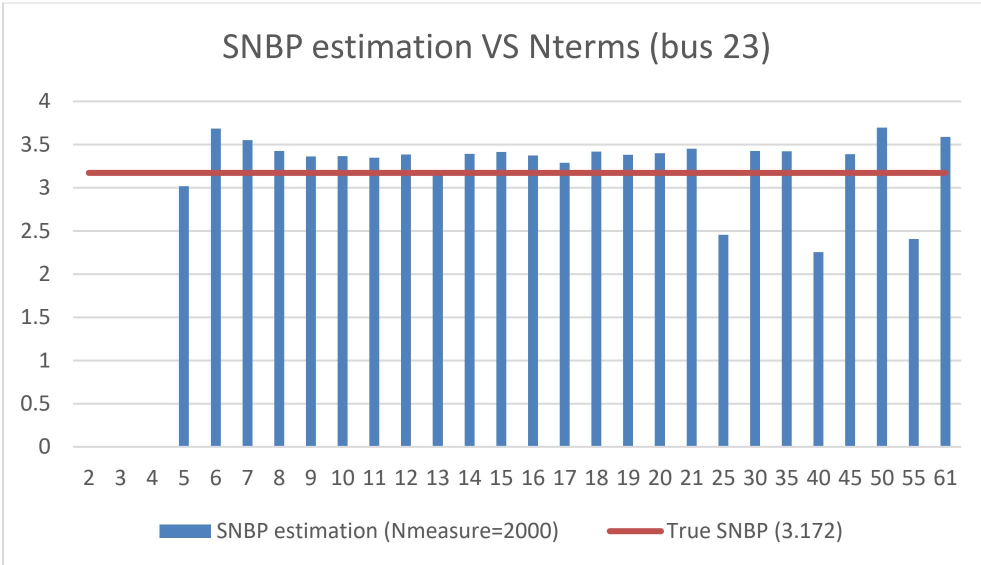

Figure 4.21 The estimation of SNBP vs. number of series terms used in building the Padé approximant of V_L using 2000 measurements

4.4.3 The effect of precision

As shown in Figure 4.20, we classify three types of poles/zeros of the Padé approximant by their locations: meaningful pole/zero, training range pole/zero, and circle pole/zero. To have a better understanding of which factors affect the locations of those roots, we implemented a high precision code that we used to perform the following tests. We recognized that spurious roots could be caused by errors in either the measurements or the calculation of the Padé approximant. Therefore, we implemented our training algorithm with different numbers of digits of precision in both obtaining the pseudo-measurements and fitting the Padé approximants. The simulation results are shown in Figure 4.22, Figure 4.23, and Figure 4.24. The number of terms used here is 50.

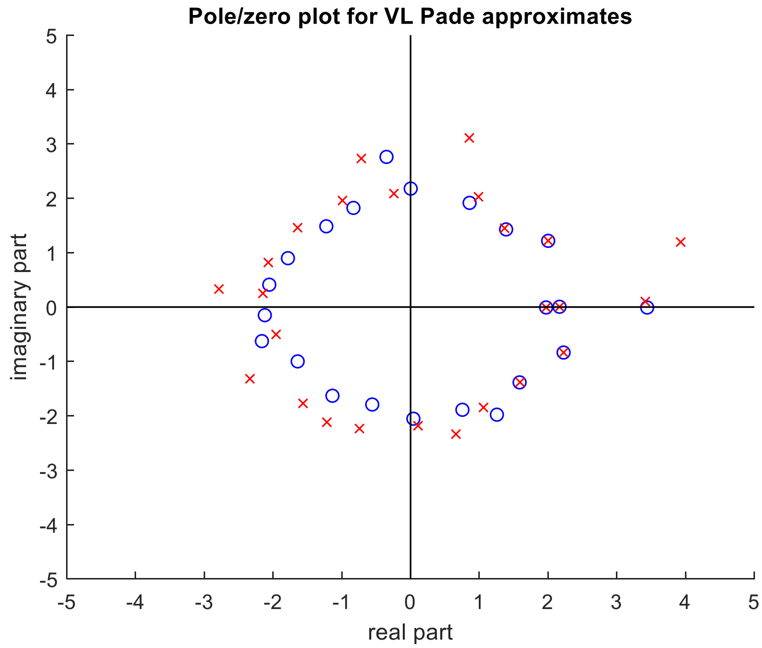

Figure 4.22 Pole-zero plot for V_L Padé approximant for the modified 118 bus system (double precision measurements, double precision Padé approximant)

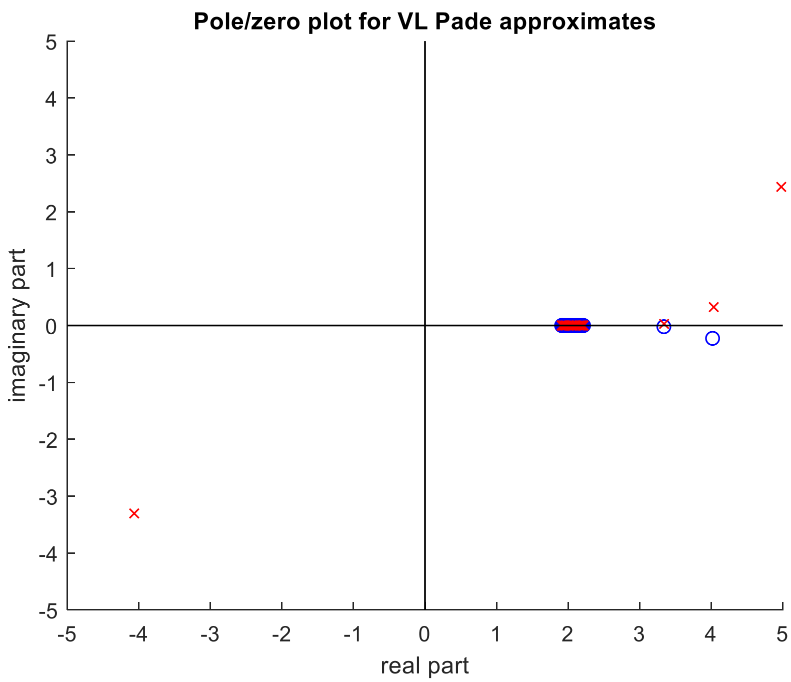

Figure 4.23 Pole-zero plot for V_L Padé approximant for the modified 118 bus system (double precision measurements, 220 digits of precision Padé approximant)

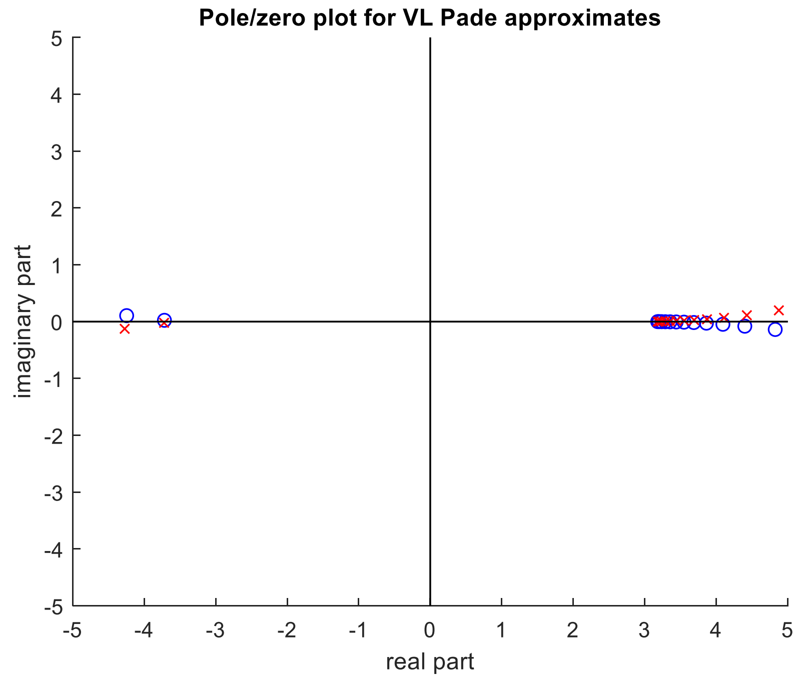

Figure 4.24 Pole-zero plot for V_L Padé approximant for the modified 118 bus system (220 digits of precision measurements, 220 digits of precision Padé approximant)

By comparing Figure 4.22 and Figure 4.23, we can see that the circle poles/zeros disappear when using high precision to fit the Padé approximants. Therefore, the circle poles/zeros are in fact spurious roots due to round-off errors during the calculation of the Padé approximant coefficients. Note that the circle poles/zeros in Figure 4.22 seem to move to the training data range as shown in Figure 4.23 and the location of the meaningful poles/zeros does not change much when using high precision to fit the Padé approximants.

By comparing Figure 4.23 and Figure 4.24, we can see that the training range poles/zeros disappear if both measurements and Padé approximants are calculated with high precision. In addition, the meaningful poles/zeros are closer to the true SNBP of the system (the meaningful pole/zero is located at 3.34 and 3.172 in Figure 4.23 and Figure 4.24 respectively). Therefore, we can conclude that the occurrence of those training range poles/zeros comes from measurement errors. Also, obtaining a more accurate estimation of the meaningful pole requires using high precision for both measurements as well as Padé approximants. Given that precision is limited from PMU measurements (maybe 3-4 accurate digits, if noise is minimal), accurately predicting the SNBP from measured data will require more elaborate means than the simple roots method.

In summary, in order to improve the accuracy of roots method for estimating the SNBP, one should focus on reducing measurement noise or eliminating spurious poles/zeros caused by the computation of Padé approximants.

4.4.4 Comparison of the MPTT and the roots method

The comparison of SNBP estimation error produced by the MPTT using the Built-In method and the roots method was performed using the eleven weakest buses for the modified 118 bus system. The measurements in the 60%-70% range were used to fit the Padé approximant, obtained using MATPOWER with a power-mismatch convergence tolerance of 10^{-8}. The numerical results are shown in Figure 4.25 where mp120 represents using 120 digits of precision to fit the Padé approximants. The error in the SNBP estimation is the average of the absolute errors for all buses shown in Figure 4.25.

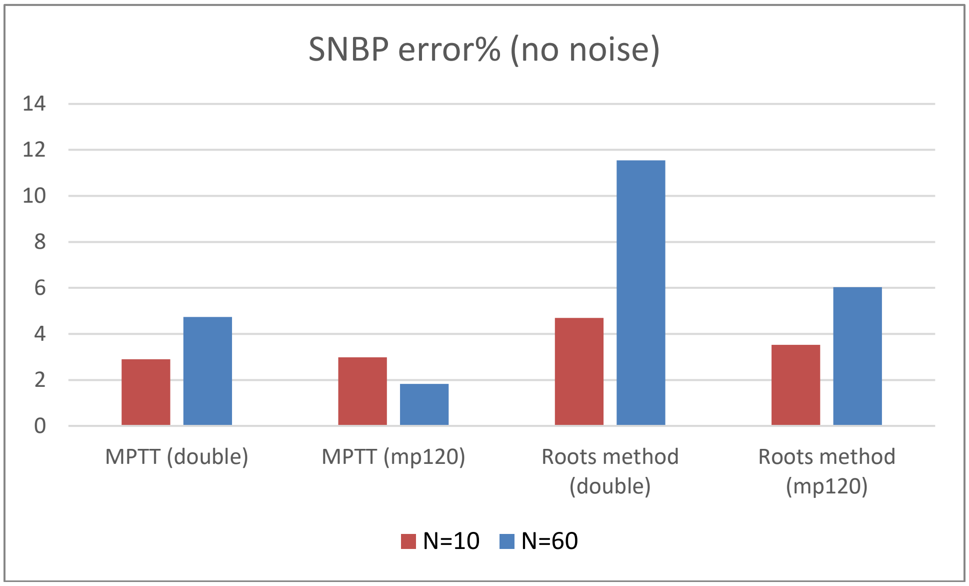

Figure 4.25 Comparison of MPTT and roots method for estimating the SNBP

From Figure 4.25 we can conclude that:

(1) The MPTT method can give more accurate results than the roots method for the system test. The roots method is more sensitive to the number of terms and digits of precision used for the Padé approximant.

(2) Reducing the order of Padé approximant (for example, using n=10 instead of n=60 in this case) helps to eliminate estimation errors with the roots method and with the MPTT method when using double precision.

(3) Increasing precision can improve accuracy, which is expected. But when we use a small-order Padé approximant (n=10 for example), the effect of precision is not as significant.

Therefore, generally, estimating the SNBP using the MPTT method with double precision and n=10 for the Padé approximant seems to be a prudent choice. More numerical experiments on a wide variety of systems is needed to confirm this hypothesis.

4.5 Numerical comparison of different methods using noisy measurements

4.5.1 Numerical results

We inserted random noise (zero mean, standard deviation of 0.01) in a range of PMU voltage pseudo-measurements from the modified 118 bus system and repeated the same numerical tests as presented in section 4.3. The numerical results we obtained are shown in Table 4.7 and Figure 4.26. The average error in SNBP estimation for a 70%-80% training range is around 15%, which is unacceptable. The poles/zeros of the Padé approximant for bus 23 are plotted in Figure 4.27. It is observed that there are no meaningful poles/zeros in this plot because of the corruption of the measurements by noise; therefore, neither the MPTT method nor the roots method works and more research is needed in the future to develop different methods for ameliorating measurement error.

Table 4.7 Percent error in SNBP estimation for noisy measurements in the 70%-80% training range for the modified 118 bus system

Bus no.	Numerical methods			Average error over all methods (%)
	Built-In (%)	Self-Coded (%)	Best Component (%)	
21	-19.4515	-19.1362	-16.6141	18.40059
22	-19.4515	-17.8752	-19.4515	18.92602
20	-19.1362	17.74905	-4.6343	13.83985
44	11.44388	-15.0378	-15.3531	13.94493
43	-13.4615	-7.47163	-11.2547	10.7293
45	-19.4515	-19.4515	-19.1362	19.34636
23	-16.2989	-7.78689	-19.4515	14.5124
38	-17.2446	-19.4515	-19.4515	18.71585
30	-11.57	-19.4515	6.399748	12.47373
37	-15.6683	-18.8209	-19.4515	17.98024
17	-10.6242	-0.8512	-15.9836	9.153005
Average error over all buses	15.80018	14.82575	15.19833	15.27475

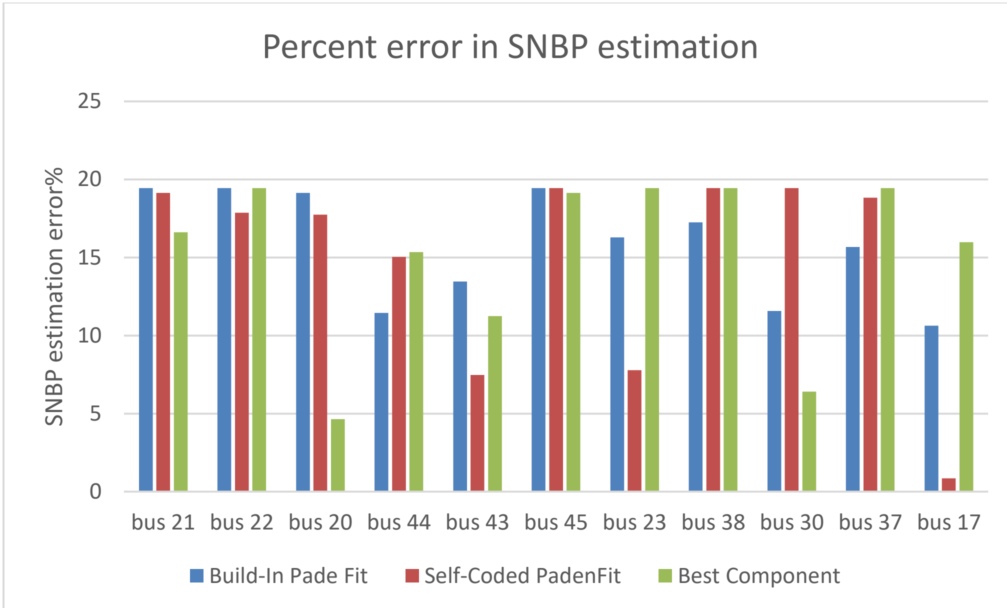

Figure 4.26 Percent error in SNBP estimation for noisy measurements in the 70%-80% training range

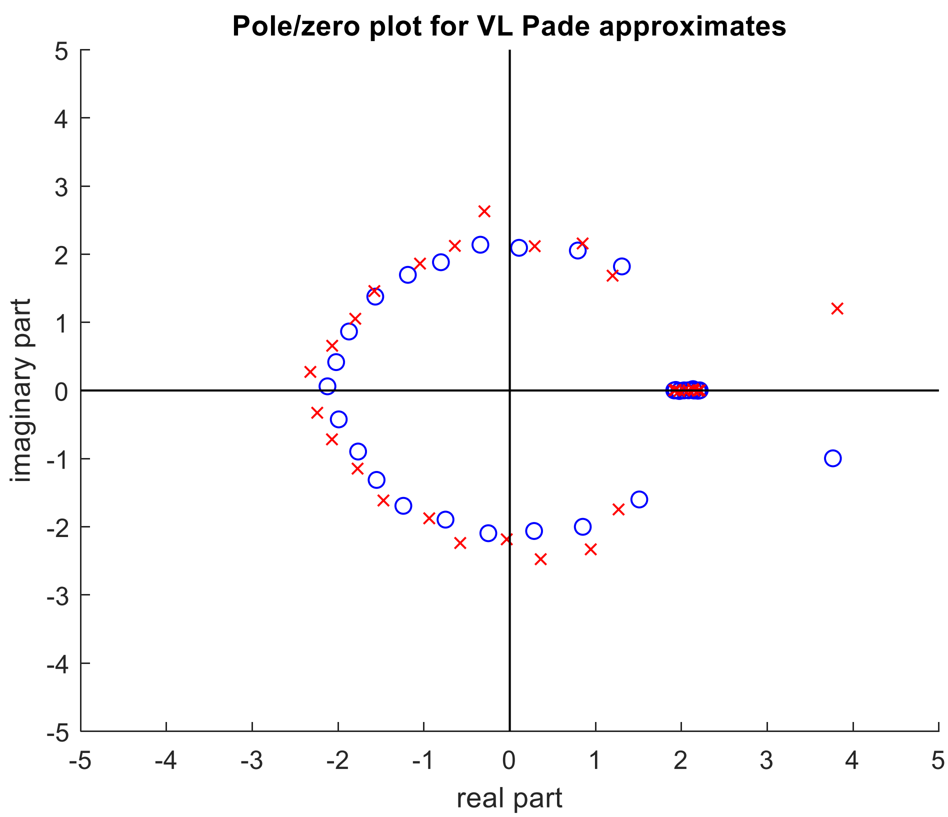

Figure 4.27 Pole-zero plot for V_L Padé approximant with noisy measurements

4.5.2 Analytic Derivative method

In the above tests, the components $\partial|V_s(\alpha)|^2$and ∂R_L in the MPTT were obtained by directly fitting the corresponding Padé approximant from the corresponding numerically calculated incremental values, i.e., the numerically calculate voltage and load resistance increments (i.e., subtraction of adjacent measurements), respectively. Even relatively small deviations in these measurements from the true values (due to measurement noise) will have a large effect on the value of the increment, and therefore on the derivative. To eliminate the use of the numerically calculated incremental values, another fitting technique was developed, specifically the "Analytic Derivative" method, introduced next.

In the Analytic Derivative method, rather than taking the derivative numerically by subtracting adjacent measurements, the Padé approximant of the needed function is first constructed and then the derivative of this function is performed analytically. For example, the Padé approximant for $\partial|V_s(\alpha)|^2$ is obtained by first fitting the Padé approximant to $|V_s(\alpha)|^2$ from the square of the magnitude of the source voltage measurements and then taking the derivative of this rational function. The approach to getting the Padé approximant for ∂R_L is similar. The MPTT results using the Analytic Derivative method for weak bus 22 in the modified 118 bus system from noiseless measurements is plotted in Figure 4.28 and compared with the results from the Built-In method. The measurement range is 60%-70% of the SNBP load, i.e., α in the range 1.9032<α<2.2204. It is shown that the Analytic Derivative method does not perform as well as the Built-In method because the LHS of the MPTT for the Analytic Derivative method deviates more from the true curve earlier than the Built-In method. It is believed that performance is inferior in cases with noiseless measurements because the process of taking the derivative for $\partial|V_s(\alpha)|^2$ and ∂R_L produces roundoff error.

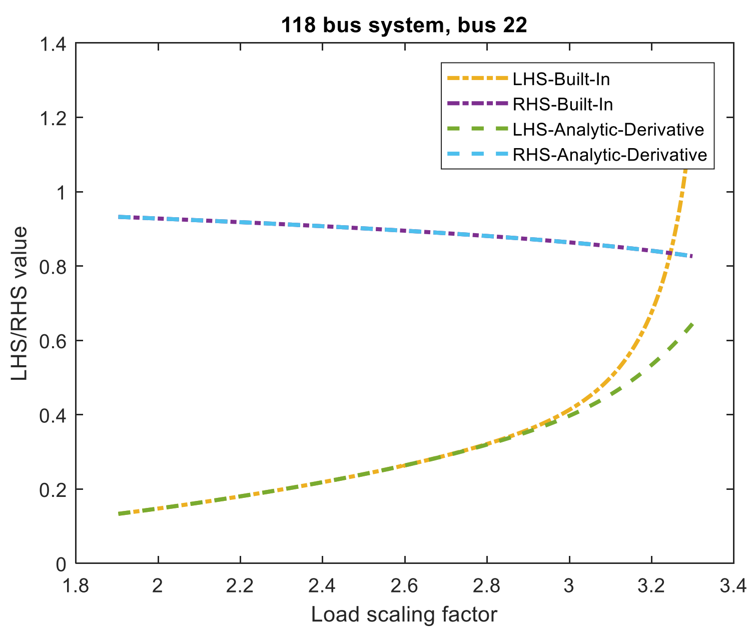

Figure 4.28 LHS and RHS of (3.35) at weak bus number 22 vs. the loading scaling factor for the modified 118 bus system using noiseless measurements

Next, we inserted random noise (zero mean, standard deviation of 10^{-9} and 10^{-6}) into the voltage measurements and repeated the above numerical tests. The MPTT results using noisy measurements with a standard deviation of 10^{-9} and 10^{-6} are shown in Figure 4.29 and Figure 4.30, respectively. We can see that when using measurements with noise, the Analytic Derivative method performs better than the Built-In method because it avoids the use of numerically calculated incremental values. However, this method is still not able to estimate the SNBP with acceptable accuracy. More effort is needed to improve the numerical performance.

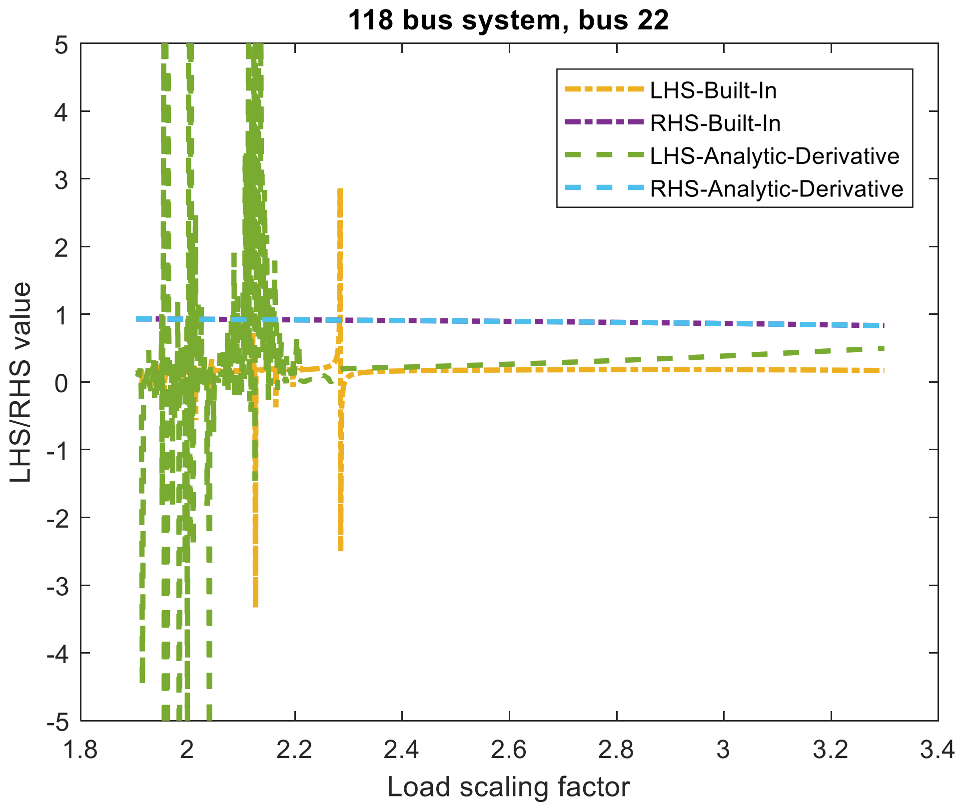

Figure 4.29 LHS and RHS of (3.35) at weak bus number 22 vs. the loading scaling factor for the modified 118 bus system using noisy measurements with standard deviation of 10^{-9}

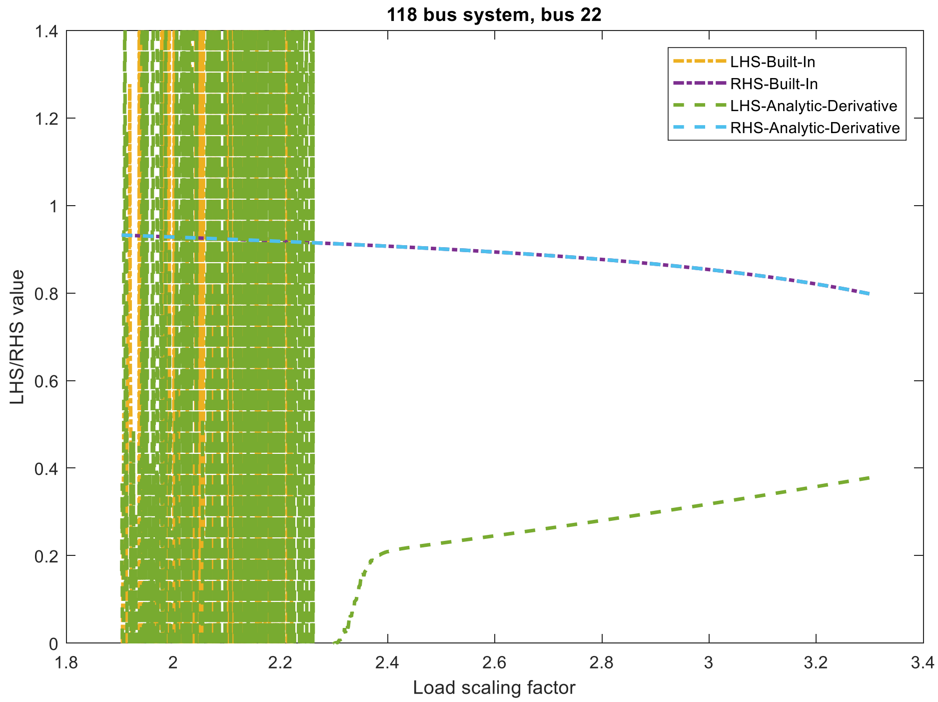

Figure 4.30 LHS and RHS of (3.35) at weak bus number 22 vs. the loading scaling factor for the modified 118 bus system using noisy measurements with standard deviation of 10^{-6}

4.5.3 Summary

From above tests, we see that the noise in the measurements (whether injected, or inherent as roundoff error in the calculation of the pseudo-measurements) has a similar effect on poles/zeros as roundoff error (generated in the calculation of the Padé approximant). They lead to spurious roots in the Padé approximant and affect the accuracy of the non-spurious poles/zeros and the accuracy of the SNBP prediction. It is important to develop methods to eliminate the effect of noise, which is left as future work.

4.6 Summary

This chapter concentrates on the application of HEM to the estimation of the SNBP using local measurements. We developed a nonlinear Thévenin-like network from HE reduction and establish the Maximum Power Transfer Theorem for estimating the SNBP, which has been validated using high precision. Different numerical methods are investigated and the comparison of their numerical performance is conducted on a modified version of the IEEE 118 bus system using measurements with/without noise. We also looked at the poles/zeros of the Padé approximant to analyze the source of estimation error. We found that spurious pole/zero pairs caused by measurement error and roundoff error impacted accuracy. Developing different ways to minimize the effect of noise is necessary and is left for future work.

5. Conclusions

The local-measurement-based methods of estimating the SNBP using linear Thévenin networks were explored along with the possible impacts of discrete changes on such methods. HE-reduction was used to develop nonlinear Thévenin-like networks for which the maximum power transfer condition was derived and verified. It was shown that, for such Thévenin-like networks as well as nonlinear multi-bus reduced-order networks, the topology and impedances of the reduced network can be arbitrarily assumed and measurements be used to fit the polynomials for the nonlinear voltage source/current injections. A revised sigma index was obtained using the nonlinear Thévenin-like network, however it was seen that it cannot be used in raw form to estimate the weak buses in the system. Whether the sigma index can be used in some form to identify weak buses remains an open problem.

The theory for building nonlinear networks from PMU measurement of the bus-voltage and then using the MPTT and the roots method to predict the SNBP was developed. The performance of some of the proposed numerical methods worked acceptably on noiseless pseudo-measurements. When these methods were used with pseudo-measurements that were corrupted with noise the performance was less accurate than hoped. Methods for improving the performance are suggested in the report.

References

[1] A. Trias, "The holomorphic embedding load flow method," IEEE Power and Energy Society General Meeting, July 2012, pp. 1-8.

[2] S. D. Rao, D. J. Tylavsky, and Y. Feng, "Estimating the saddle-node bifurcation point of static power systems using the holomorphic embedding method," International Journal of Electrical Power & Energy Systems, vol. 84, pp. 1-12, 2017.

[3] R. J. Avalos, C. A. Cañizares, F. Milano, and A. J. Conejo, "Equivalency of continuation and optimization methods to determine saddle-node and limit-induced bifurcations in power systems," IEEE Transactions on Circuits and Systems I: Regular Papers, vol. 56, no. 1, pp. 210-223, 2009.

[4] D. R. Gurusinghe, "Saddle Node Bifurcation and Voltage Stability Analysis of Sri Lanka," Engineer: Journal of the Institution of Engineers, Sri Lanka, vol. 45, no. 4, 2012.

[5] V. Ajjarapu and C. Christy, "The continuation power flow: a tool for steady state voltage stability analysis," IEEE transactions on Power Systems, vol. 7, no. 1, pp. 416-423, 1992.

[6] E. Garbelini, D. A. Alves, A. B. Neto, E. Righeto, L. C. da Silva, and C. A. Castro, "An efficient geometric parameterization technique for the continuation power flow," Electric Power Systems Research, vol. 77, no. 1, pp. 71-82, 2007.

[7] E. d. M. Magalhães, A. Bonini Neto, and D. A. Alves, "A parameterization technique for the continuation power flow developed from the analysis of power flow curves," Mathematical Problems in Engineering, vol. 2012, 2012.

[8] A. B. Neto and D. Alves, "Improved geometric parameterisation techniques for continuation power flow," IET generation, transmission & distribution, vol. 4, no. 12, pp. 1349-1359, 2010.

[9] A. Jalali, M. Aldeen, "Novel continuation power flow algorithm", IEEE PES International Conference on Power Systems Technology (POWERCON), 2016.

[10] P. Xu, X. Wang, and V. Ajjarapu, "Continuation power flow with adaptive stepsize control via convergence monitor," IET generation, transmission & distribution, vol. 6, no. 7, pp. 673-679, 2012.

[11] D. A. Alves, L. C. da Silva, C. A. Castro, and V. F. da Costa, "Continuation fast decoupled power flow with secant predictor," IEEE transactions on Power Systems, vol. 18, no. 3, pp. 1078-1085, 2003.

[12] S. H. Li and H. D. Chiang, "Continuation power flow with multiple load variation and generation re-dispatch patterns," in Power Engineering Society General Meeting, 2006.

[13] K. Vu, M. M. Begovic, D. Novosel, and M. M. Saha, "Use of local measurements to estimate voltage-stability margin," IEEE Transactions on Power Systems, vol. 14, no. 3, pp. 1029-1035, 1999.

[14] D. Julian, R. P. Schulz, K. Vu, W. H. Quaintance, N. B. Bhatt, and D. Novosel, "Quantifying proximity to voltage collapse using the voltage instability predictor (VIP)," in Power Engineering Society Summer Meeting, 2000. IEEE, 2000, vol. 2, pp. 931-936: IEEE.

[15] I. Smon, G. Verbic, and F. Gubina, "Local voltage-stability index using Tellegen's theorem," IEEE Transactions on Power Systems, vol. 21, no. 3, pp. 1267-1275, 2006.

[16] S. Corsi and G. N. Taranto, "A real-time voltage instability identification algorithm based on local phasor measurements," IEEE transactions on power systems, vol. 23, no. 3, pp. 1271-1279, 2008.

[17] H. Yuan and F. Li, “A comparative study of measurement-based Thevenin equivalents identification methods,” in North American Power Symposium (NAPS), 2014, 2014, pp. 1-6: IEEE.
[18] EPRI Technical Update: Voltage Instability Load Shedding. EPRI, Palo Alto, CA: 2006. 1012491.
[19] M. Zima, M. Larsson, P. Korba, C. Rehtanz, and G. Andersson, “Design aspects for wide-area monitoring and control systems,” Proceedings of the IEEE, vol. 93, no. 5, pp. 980-996, 2005.
[20] G. Huang, L. Zhao, “Measurement Based Voltage Stability Monitoring of Power System,” PSERC publication 2001, available online: www.pserc.wisc.edu, 2001
[21] M. Larsson, C. Rehtanz, J. Bertsch, “Real-Time Voltage Stability Assessment of Transmission Corridors,” Proc. IFAC Symposium on Power Plants and Power Systems, Seoul, S. Korea, 2003
[22] J.-H. Liu and C.-C. Chu, “Wide-area measurement-based voltage stability indicators by modified coupled single-port models,” IEEE Transactions on Power Systems, vol. 29, no. 2, pp. 756-764, 2014.
[23] S. G. Ghiocel et al., “Phasor-measurement-based voltage stability margin calculation for a power transfer interface with multiple injections and transfer paths,” in Power Systems Computation Conference (PSCC), 2014, 2014, pp. 1-6: IEEE.
[24] F. Hu, K. Sun, A. Del Rosso, E. Farantatos, and N. Bhatt, “Measurement-based real-time voltage stability monitoring for load areas,” IEEE Transactions on Power Systems, vol. 31, no. 4, pp. 2787-2798, 2016.
[25] B. Milosevic, M. Begovic, “Voltage-stability protection and control using a wide-area network of phasor measurements,” IEEE Trans. Power Systems, vol. 18, no. 1, pp. 121-127, 2003.
[26] M. Glavic and T. V. Cutsem, “A Short Survey of Methods for Voltage Instability Detection,” Proceedings of the IEEE PES General Meeting, Detroit, July 2011.
[27] Y. Zhu, D. Tylavsky, and S. Rao, “Nonlinear structure-preserving network reduction using holomorphic embedding,” IEEE Transactions on Power Systems, vol. 33, no. 2, pp. 1926-1935, 2018.
[28] S. Rao and D. Tylavsky, “Nonlinear network reduction for distribution networks using the holomorphic embedding method,” in North American Power Symposium (NAPS), 2016, 2016, pp. 1-6: IEEE.
[29] P. Kundur, N. J. Balu, and M. G. Lauby, Power system stability and control. McGraw-hill New York, 1994.
[30] P. Gonnet, S. Suttel, and L. N. Trefethen, “Robust Padé Approximation via SVD,” SIAM Review, vol. 55, no. 1, pp. 101-117, 2013.
[31] Shruti Rao, Yang Feng, Daniel Tylavsky and Muthu Kumar Subramaniam, “The Holomorphic Embedding Method Applied to the Power-Flow Problem,” IEEE Transactions on Power Systems , vol. 31, no. 5, pp. 3816-3828, Sept. 2016.
[32] C. A. Canizares and F. L. Alvarado, “Point of collapse and continuation methods for large AC/DC systems,” IEEE Transactions on Power Systems, vol. 8, no. 1, pp. 1-8, Feb 1993.
[33] A. Trias, “Sigma algebraic approximants as a diagnostic tool in power networks,” US Patent 2014/0156094 (2014).
[34] R. D. Zimmerman, C. E. Murillo-Sánchez and R. J. Thomas, “MATPOWER: Steady-State Operations, Planning and Analysis Tools for Power Systems Research and Education,” IEEE

Transactions on Power Systems, Feb. 2011, vol. 26, no. 1, pp. 12-19.
[35] "Voltage Security Assessment Tool," DSATools, accessed in April 2015, available at: http://www.dsatools.com/html/prod_vsat.php.
[36] J. S. Giraldo, J. A. Castrillon and C. A. Castro, "Network-free voltage stability assessment of power systems using phasor measurements," 2015 IEEE Eindhoven PowerTech, Eindhoven, 2015, pp. 1-5.
[37] S. A. Soliman, H. K. Temraz and S. M. El-Khodary, "Power system voltage stability margin identification using local measurements," Large Engineering Systems Conference on Power Engineering, 2003, 2003, pp. 100-104.
[38] M. Parniani, J. H. Chow, L. Vanfretti, B. Bhargava, A. Salazar, "Voltage Stability Analysis of a Multiple-Infeed Load Center Using Phasor Measurement Data," Proc. 2006 IEEE Power System Conference and Exposition, Atlanta, GA, Oct./Nov. 2006.
[39] P. Zhang, L. Min, N. Zhang, "Voltage Instability Load Shedding," EPRI Report 1012491, Sep. 2006.
[40] Illinois Center for a Smarter Electric Grid (ICSEG), "IEEE 14-Bus System," accessed, April 2017, available at: http://icseg.iti.illinois.edu/ieee-14-bus-system/
[41] S. S. Biswas, C. B. Vellaithurai and A. K. Srivastava, "Development and real time implementation of a synchrophasor based fast voltage stability monitoring algorithm with consideration of load models," 2013 IEEE Industry Applications Society Annual Meeting, Lake Buena Vista, FL, 2013, pp. 1-9.
[42] A. Perez, H. Jóhannsson, J. Østergaard, M. Glavic and T. Van Cutsem, "Improved Thévenin equivalent methods for real-time voltage stability assessment," 2016 IEEE International Energy Conference.
[43] K. Sun, F. Hu and N. Bhatt, "A new approach for real-time voltage stability monitoring using PMUs," 2014 IEEE Innovative Smart Grid Technologies - Asia (ISGT ASIA), Kuala Lumpur, 2014, pp. 232-237.
[44] D. Osipov, F. Hu and K. Sun, "Voltage stability margin estimation for a load area using a three-bus equivalent," 2016 IEEE Power and Energy Society General Meeting (PESGM), Boston, MA, 2016, pp. 1-5.
[45] F. Hu, K. Sun, A. Del Rosso, E. Farantatos and N. Bhatt, "An adaptive three-bus power system equivalent for estimating voltage stability margin from synchronized phasor measurements," 2014 IEEE PES General Meeting, Conference & Exposition, National Harbor, MD, 2014, pp. 1-5.
[46] M. Nakmali, D. Osipov and K. Sun, "A new hybrid approach to thevenin equivalent estimation for voltage stability monitoring, " 2015 IEEE Power & Energy Society General Meeting, Denver, CO, 2015, pp. 1-5.
[47] A. Wiszniewski, "New Criteria of Voltage Stability Margin for the Purpose of Load Shedding, " in IEEE Transactions on Power Delivery, vol. 22, no. 3, pp. 1367-1371, July 2007.
[48] I. Dobson and L. Lu, "Voltage collapse precipitated by the immediate change in stability when generator reactive power limits are encountered," IEEE Transactions on Circuits and Systems I: Fundamental Theory and Applications, vol. 39, no. 9, pp. 762-766, Sep 1992.
[49] S. S. Baghsorkhi, S. P. Suetin, "Embedding AC Power Flow in the Complex Plane Part II: A Reliable Framework for Voltage Collapse Analysis," arXiv:1609.01211v1 [cs.SY], 2016.
[50] Zima M., Larsson M., Korba P., Rehtanz C., Andersson G., "Design aspects for wide-area monitoring and control systems," Proceedings of the IEEE, vol. 93, no. 5, pp. 980-996, 2005.

[51] S. Rao, D. Tylavsky, V. Vittal, W. Yi, D. Shi and Z. Wang, “Fast Weak-Bus and Bifurcation Point Determination using Holomorphic Embedding Method,” 2018 IEEE Power & Energy Society General Meeting (PESGM), Portland, OR, 2018, pp. 1-5.